Analysis of the Component- and Control System Application of a Hydropower- and PV Based DC Microgrid Designed for Electrifying Land-Based Industries in Norway

Andreas Gerhardsen Vikestad

Andreas Frantzen

SUPERVISORS

Professor Mohan Lal Kolhe

Sandun Yasantha Konara Konara Mudiyanselage

University of Agder, 2022

Faculty of Engineering and Science

Department of Engineering and Sciences

Abstract

The Norwegian Water Resources and Energy Directorate reports that a significant share of Norway's greenhouse gas emissions originates from burning fossil fuels in the land-based industry. Although some electrification and energy cuts have been initiated, the current technology for further electrification, particularly chemical industries, is classified as "immature". The electrification development of such industries is recognized as a critical step in reducing Norway's land-based industry's carbon footprint. However, this requires considerable investments in the public grid. Intending to address this, the thesis attains the NWA concept by proposing a hydropower- and PV based DC microgrid structure using hybrid energy storage.

The software MATLAB Simulink™ is used to design, model, and simulate the microgrid. The model covers a 100 kW PV system, an 85 kVA rated salient pole synchronous generator and an energy storage system incorporating either exclusively a battery system or in conjunction with a supercapacitor system. This system undertakes three modes of operation, simulated for two different load cases with different demand responses. The goal is to determine a control system- and component applications that satisfy a predetermined stability requirement while sharing out the power contributions to saturate the load demand. For the first two modes of operation, the DC bus is controlled by the HES system, whereas the generator operates first with constant rotation and field voltage, and then with an excitation system. In the third mode of operation, the DC bus is controlled by the generator system, while the battery system is tasked with saturating the remaining load demand.

The thesis concludes that the proposed system shows promising characteristics for electrifying land-based industry, and the obtained robustness in the control system is satisfactory for selected component applications. Moreover, the system can somewhat attain the NWA concept, although the obstacle of safeguarding energy storage capacity must be overcome to practically implement it.

Preface

We, the authors of this thesis, would like to take this opportunity to extend our most sincere gratitude to our two supervisors- Professor Mohan Lal Kolhe and Engineer Sandun Yasantha Konara Konara Mudiyanselage, for providing a platform of knowledge for us to make our research on. Since the basis of the work conducted in this thesis was formed, in the spring of 2021, both Prof. Mohan and Eng. Konara have been highly supportive of the project and have provided invaluable help for us to arrive where we wanted with this work. For this we are grateful.

Additionally, we would like to extend a thanks to Dr. K. Raghavendra Naik for providing his expertise within microgrid control and voltage stabilization. His help with the Simulink modelling has been imperative for us to achieve what we wanted with our model. We are therefore immensely grateful for him spending his own time to help us.

This thesis is the results of an accumulation of knowledge within the field of smartgrid throughout this master programme. The initial groundwork of the subject was formed in the course ENE506-G “Smartgrid Systems”, where we got the opportunity to write a report on the control strategy of PV based nano- and microgrid systems. A further development on this was conducted in the following semester in the course ENE503-G “Energy Research Project” where our research paper on the analysis of the component- and control system application of a PV based DC microgrid was conceived. As a continuation of that research, this master’s thesis undertakes a more practical approach with regards to the application of several modes of operation in a DC microgrid designed to undertake the issues of electrifying Norwegian DC-based industries.

Individual/group Mandatory Declaration

The individual student or group of students is responsible for the use of legal tools, guidelines for using these and rules on source usage. The statement will make the students aware of their responsibilities and the consequences of cheating. Missing statement does not release students from their responsibility.

1.	I/We hereby declare that my/our report is my/our own work and that I/We have not used any other sources or have received any other help than mentioned in the thesis.	☒
2.	I/we further declare that this thesis: - has not been used for another exam at another department/university/university college in Norway or abroad; - does not refer to the work of others without it being stated; - does not refer to own previous work without it being stated; - have all the references given in the literature list; - is not a copy, duplicate or copy of another's work or manuscript.	☒
3.	I/we am/are aware that violation of the above is regarded as cheating and may result in cancellation of exams and exclusion from universities and colleges in Norway, see Universitets- og høgskoleloven §§4-7 og 4-8 og Forskrift om eksamen §§ 31.	☒
4.	I/we am/are aware that all submitted theses may be checked for plagiarism.	☒
5.	I/we am/are aware that the University of Agder will deal with all cases where there is suspicion of cheating according to the university's guidelines for dealing with cases of cheating.	☒
6.	I/we have incorporated the rules and guidelines in the use of sources and references on the library's web pages.	☒

Publishing Agreement

Authorization for electronic publishing of the thesis.

Author(s) have copyrights of the thesis. This means, among other things, the exclusive right to make the work available to the general public (Åndsverkloven. §2).

All theses that fulfill the criteria will be registered and published in Brage Aura and on UiA's web pages with author's approval.

Theses that are not public or are confidential will not be published.

I hereby give the University of Agder a free right to

make the task available for electronic publishing: ☒YES ☐NO

Is the thesis confidential? ☐YES ☒NO

(confidential agreement must be completed and signed by the Head of the Department)

- If yes:

Can the thesis be published when the confidentiality period is over? ☐YES ☐NO

Is the task except for public disclosure? ☐YES ☒NO

(contains confidential information. see Offl. §13/Fvl. §13)

Table of content

List of Figures

List of Tables

Nomenclature

Abbreviation	Meaning
NVE	Norges Vassdrags- og energidirektorat / The Norwegian Water Resources and Energy Directorate
NWA	Non-Wires Alternative
PV	Photovoltaic
ICT	Information and communication
IoT	Internet of things
DDoS	Distributed Denial-of-Service
AGC	Automatic generation control
AVR	Automatic voltage regulation
PID	Proportional-integral-derivative
IGBT	Insulated-gate bipolar transistor
HES	Hybrid energy storage
MPPT	Maximum power point tracking
MOSFET	metal-oxide-semiconductor field-effect transistor
PWM	Pulse width modulation
VSR	Voltage source rectifier
P&O	Perturb and observe
PLL	Phase locked loop
STC	Standard Test Conditions
SOC	State of charge

1 Introduction

This chapter defines the background of the thesis in the context of the current energy- and electrification situation in Norway. The electrification of land-based industry and its impending impact on the public grid is especially emphasized along with the need for attaining the NWA concept to avoid major grid investments. Furthermore, the research question of this thesis is stated followed by a section on the significance this work may pose in the context of the presented background. Finally, a segment on the motivation, and preliminary work on this topic is presented before the outline of the thesis is described.

1.1 Background

Norway is undeniably privileged when it comes to the possibilities of producing clean energy. The orography and geographical landscape of the country effectively enables a vast amount of energy production by means of hydropower in their many mountains, hills, and valleys. The Norwegian Water Resources and Energy Directorate (NVE) are reporting that 90 % of Norway's produced power in 2020 originated from hydropower, and 8 % originated from wind power, including imported power [1]. When considering their most recent quarterly report on new power production and power plants approved for building, though not commenced or put into operation, an increase of the portion of hydropower and wind power in the future is expected [2]. Despite the promising outlook on Norway's energy sector, it is also a reality that Norway ranks relatively high in the world for territory-based CO_2 emissions per capita. Data from 2020 shows that the country's territorial CO_2 emissions per capita outdo the world average by 67 % and the Europe average by 30 % [3-5].

In a combined effort, the Norwegian Ministry of Petroleum and Energy, NVE, and the Norwegian Environment Agency have launched an investigation to address Norway's carbon footprint. They found that a significant share of Norway's greenhouse gas emissions originates from the use of fossil fuel in three sectors- the transport sector, land-based industry, and offshore oil- and gas fields[6, 7]. Furthermore, when considering the wealth of green energy in the Norwegian power industry, it is also stated that the electrification of these three sectors is viewed as an imperative step towards reducing Norway's carbon footprint [7-9].

By the spring of 2022, a certain degree of electrification of the three sections has already commenced. As disclosed by the Norwegian Petroleum Directorate, several offshore oil- and gas fields have already applied, or decided to use, power from the mainland [9]. Additionally, the electrification of the transport sector, being an increasingly hot topic, is continuously gaining momentum both commercially and industrially [8]. As for the land-based industry sector, NVE reports that some electrification and energy cuts have been initiated in this sector as well [7], although the current technology for further electrification of certain industries, such as chemical industries, are reportedly classified as "immature" [10]. The development of the electrification strategy of such industries is recognized as a critical step in addressing the carbon footprint of Norway's land-based industry.

NVE estimates in their enquiry from 2020 a total increase in the annual Norwegian power consumption by roughly 23 [TWh], in addition to separate consumption growths, as a consequence of electrifying the three sectors mentioned above [8]. These electrification measures imply that considerable investments in the power grid are necessary if they are to be realised. Since the upgrades in the grid must take place

before the bulk of the electrification process is initiated, it is unlikely that these measures will be completed in the immediate future. This thesis aims to address the issues of electrifying the land-based industries, such as chemical industries, classified as immature by today's technology standard, by proposing a microgrid approach with roots in smartgrid technology and distributed generation. By undertaking a scenario focusing on minimizing the impact on the current grid, the proposed solution is also expected to decrease the potential investments in the grid infrastructure to realize the electrification measures. This would result in cutting the investment cost and reducing the time for the electrification to be realised.

In contrast to the traditional approach of centralized power systems, the microgrid based, distributed generation scheme benefits from short transmission lines between the power source and -consumer. Reducing the transmission line lengths in the power infrastructure enables the microgrid to naturally become less prone to outages while simultaneously streamlining the power transmission due to lower transmission losses. In the pursuit of reducing the impact on the grid infrastructure, the latter point is considered particularly imperative because a reduced overall efficiency between the power source and -consumer would be detrimental. Also, the microgrid topology naturally provides the flexibility to efficiently integrate local, intermittent, clean, and green energy sources to the power grid without any major reactive power compensation from the grid. The added on-site energy production will also lessen the impact on the existing grid infrastructure whilst the topology itself facilitates the option of island mode operation. Furthermore, microgrid operation also promotes the possibility of operating as a DC bus which also is inclined to economize DC appliances' consumption.

Due to the growing employment of DC sources and loads to the power grid, DC microgrids are becoming progressively popular compared to their conventional counterpart- the AC microgrid. There are several arguments as to why the DC microgrid is predicted to represent the future of the power grid, though IEEE Power & Energy Society's Industry Technical Support Leadership Committee Task Force highlights its promotion in the context of climate change as particularly significant [11]. In their technical report from 2022, on modernization of the power grid with respect to climate change, they state that power grids of the future require redevelopment, taking into consideration the effects of the current probable future. They especially highlight the increased frequency- and magnitude of extreme weather conditions, increased temperatures, and human interferences like physical- or cyber-attacks as issues to consider [11]. The report proposes the employment of DC microgrids as one of the more viable options for addressing many of the issues mentioned above while promoting global decarbonization. In addition to effectively integrating the ever more eminent DC loads, DC microgrids' ability to easily facilitate battery storage makes them particularly well suited to perform certain mechanics that are crucial in developing a smartgrid architecture.

In the context of [11], energy storage systems integrated into a microgrid structure makes the microgrid inherently more resilient to extreme weather conditions, improving power availability in situations that otherwise would cause a power outage. Additionally, the ability to store energy for later use enables more purposeful operations when combined with intermittent energy sources such as PV power, which would also facilitate increased penetration of renewable energy sources to the power infrastructure. The microgrid itself will also be able to undergo energy efficiency operations such as peak shaving during hours of high load demands, further reducing the stress on the public grid.

A near-complete utilisation of battery integrated microgrids that is particularly relevant to modernizing the power grid is the "Non-Wires Alternative" (NWA). In the report [11], NWA is described as a concept of increasing the degree of electrification in a microgrid without major investment in the existing power

grid. By utilising distributed generation with integrated battery energy storage, forming a microgrid structure, the report states that a high degree of electrification can be completed without major investments in the existing transmission and distribution grid, given a substantial amount of local renewable energy integration and a viable smartgrid system architecture operation.

Smartgrid system architecture incorporates mechanisms spanning from the primary control of the local power systems' physical layer to socioeconomic considerations of entire communities' infrastructures. In order to ensure the system's optimal operation to the circumstances in the actual community, every level of the infrastructure must be accessed and appraised. However, a special emphasis must be taken on the real-time regulation of the smartgrid since the system architecture takes on a hierarchical format. This implies that the lower or more fundamental level of the system sets the benchmark for how well the remaining system can operate. Ultimately, this makes the development of the component- and control system application of smartgrid systems a particularly complex affair. The smartgrid system's energy sources, load profile, and load type must therefore be carefully considered in the context of the remaining infrastructure in the grid when establishing a control strategy. This thesis will therefore attempt to undertake the specific component- and control system architecture of a DC microgrid system intended to address the general electrification of typical land-based chemical industries in Norway. In order to attain the NWA concept, the microgrid will include both dispatchable- and non-dispatchable energy sources in PV power and hydropower, respectively, as well as a hybrid energy storage system.

1.2 Research question

How can a hydro- and PV based DC microgrid be configured, in terms of component- and control system application, to attain the NWA concept and facilitate the electrification of Norwegian land-based chemical industry?

1.3 Scope

This thesis does not cover the socioeconomic considerations of higher-level control mechanisms such as the overall power market, weather forecasts, and predicted load demands and power productions, although the concepts are discussed in the context of the proposed microgrid model. Instead, the top-level mechanisms are induced through components available in the model itself, e.g., dynamic load control and predefined power production patterns. However, the authors recognize that socioeconomic considerations of communities' infrastructure in the context of smartgrid refer to more comprehensive mechanisms.

Furthermore, it stands to mention that in the hydropower generator system, used as a dispatchable energy source in the microgrid solution of this thesis does not incorporate any speed governing system. Instead, an ideal scenario is considered where the speed of the generator shaft is fixed at the nominal value of the generator at all times. The authors of this thesis are aware that this is not a true representation of a real-life hydropower application, both in terms of negating unwanted speed deviations but also in terms of controlling the active power production in the generator.

1.4 Significance

Reducing Norway's carbon footprint is intrinsically linked to the electrifying of the land-based industry sector, such as the chemical industry [7, 10]. However, directly electrifying such large sectors, energy-wise, with the grid approach already in place, requires a tremendous upgrade in the public grid and

would therefore generate large investment costs and further impede the electrification process [7]. By implementing the NWA concept, one can explore a way of bypassing this challenge and significantly reduce the amount of upgrades needed in the power grid, introducing a more efficient grid operation [11]. This is significantly beneficial in the short-term perspective, enabling a more economical and rapid electrification process. Also, in the long-term perspective, this will be advantageous in terms of streamlining the transmission and distribution infrastructure of the public grid, providing a more efficient adoption of the available power.

The NWA concept depends on a significant portion of locally produced and preferably renewable energy. DC microgrids utilizing distributed generation is, therefore, a desirable framework to implement NWA on. However, proper smartgrid operation of the microgrid is a complex subject that greatly depends on the context and constitution of the microgrid and is, therefore, a topic under constant development. Engaging in the component- and control system application of a microgrid design intended to address the electrification of the Norwegian land-based industry will work as a contribution towards developing a microgrid composition that is applicable to electrifying Norwegian land-based industry.

1.5 About This Thesis

This thesis is based on the previously conducted, unpublished energy research project from the 7.5 ECTS course ENE503-G "Analysis of the Component- and Control System Application of a PV Based DC Microgrid" [12]. The findings of the energy researched project resulted in establishing a particular component- and control system application for operating a PV based microgrids using a HES system. The motivation of this master thesis is to use the established groundwork in a more practical application with the goal of undertaking the electrification of the Norwegian land-based industry that runs on DC load, namely chemical industries. As a consequence, much of the theory segment of this thesis is based on the already established theoretical concepts introduced in the preliminary energy research project, although it is rewritten for the purpose of this thesis.

1.5.1 Thesis Outline

This master's thesis is divided into seven chapters. The chapter structure is adopting the following outline

- *Chapter 1: Introduction* – This part defines the background of the thesis, formulates a research question, and defines its significance in context the background.

- *Chapter 2: Theory and Literature Review* – In this part the theoretical framework of the thesis' subject is presented. Consecutively, as the theory is presented, the corresponding literature review is presented in context of the applied theory.

- *Chapter 3: Method* – This part conveys the methodology that is used to produce the results and conduct the analysis that this thesis' research is based on.

- *Chapter 4: Results* – The findings of the conducted simulations are presented in this part. Since the findings mainly belong to categories reflecting three modes of operation, so is this section divided as well.

- *Chapter 5: Discussion* – In this part the findings of the research, i.e., the simulations, are discussed. This part is divided on the basis of what type of result parameter is discussed.

- *Chapter 6: Conclusion* – This part draws the conclusions resulting from this thesis' work. The research question is answered.

- *Chapter 7: Future Work* – In this part a discussion on how the work of this thesis can be proceeded in the future. This includes eventual flaws in this thesis' models, or methodology that can be rectified, as well as pointing out the direction of this thesis' subject's further development.

2 Theory and Literature Review

This chapter conveys the relevant theory needed for modelling a microgrid system in Simulink, which is used to perform the analysis conducted in this thesis. The theory is presented in a manner that verifies the validity of this thesis' results. Furthermore, a review of the present standing of relevant scientific literature is conducted on both the model and its affiliated control- and application theory.

2.1 Physical Layer of a PV Based DC Microgrid Model

As an applicable portrayal of a DC microgrid solution, the physical layer of the system undertaken in this thesis is based on the conceptual block diagram in Figure 2-1. It depicts a DC microgrid consisting of a PV system, an energy storage system, and a DC load.

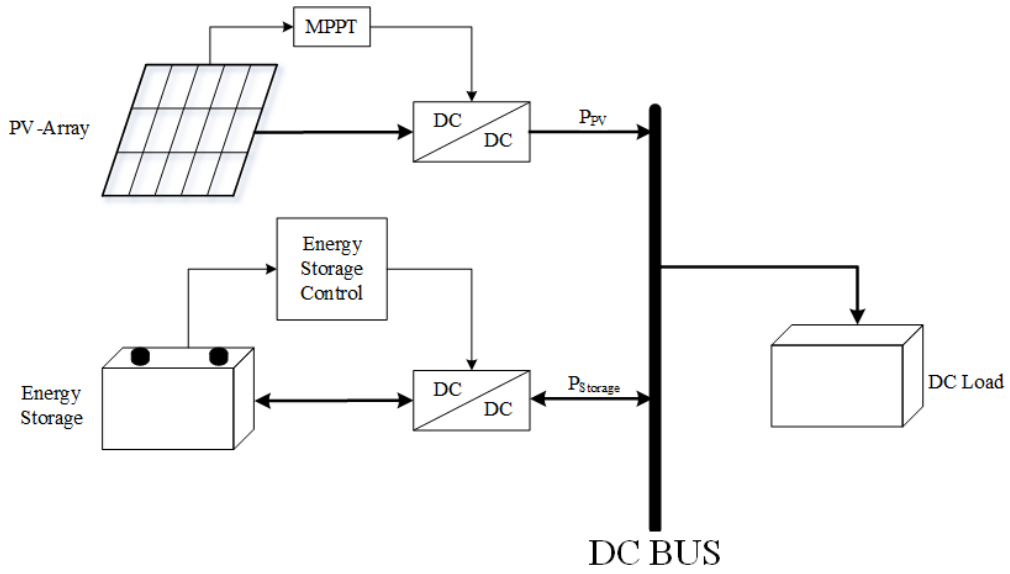

Figure 2-1 Conceptual block diagram of the representative PV based DC microgrid.

The HES system, shown in Figure 2-1, usually consist of a battery system and a supercapacitor system which are separately integrated into the DC bus. The DC microgrid structure can therefore be broken down into the following five separate sub-systems:

- PV system
- Battery system
- Supercapacitor system
- DC load system

As for imposing the sub-systems governing mechanisms, each component is equipped with a dynamic governing body. For each component, the governing bodies are in the form of boost DC-DC converters, unidirectional maximum power point tracker (MPPT) based for the PV system and bidirectional buck-boost converters for the battery- and supercapacitor systems.

2.1.1 DC-DC Boost PV Converter

The PV array's ability to directly generate renewable energy makes it a highly sought-after power source; however, the PV output voltage is generally lower than the desired operating DC bus voltage [13]. In order to conjoin the PV array with the microgrid physical layer, the output voltage of the PV system has to compliment the required DC bus voltage. This necessitates the need for a DC-DC boost converter to ensure efficient regulation of its varying output voltage. Aside from increasing the DC output voltage, the DC-DC converter provides the governing body to attain the maximum power point of the PV array. This is usually done by employing maximum power point tracking algorithms, which is discussed in greater detail in subchapter 2.1.3.

The operating principle and energy conversion relations for various DC-DC converters have been well established in a multitude of literature over the last years. Ned Mohan covers the operation of typical used DC-DC converter in all types of electronics equipment in his book, [14]. His literature offers an in-depth explanation of how the converters, such as buck and boost, are designed and built to alter the voltage to its desired level. Furthermore, Koca, Aslan, Yonetken, and Oğuz provide an enquiry about the boost converter design specifically for PV systems in their conference paper from 2019 [15]. In their conducted study, the performance of the boost converter design is tested to optimize the efficiency and energy produced by a photovoltaic system. The system is modelled and simulated using Simulink, where each model is explained in detail how the selected parameters for each component are calculated.

The equivalent circuit of a boost converter is shown in Figure 2-2. It is composed of a diode, inductor, input- and output capacitor and a switch [14, 15]. Semiconductor switches, like IGBT or MOSFET, are normally utilized because of their ability to handle rapid alternation between on- and off-state, usually governed by a "Pulse width modulation" (PWM) signal. When the switch enters its on-state, the input voltage, V_{in}, is applied across the inductor, L_{boost}, consequently ramping up the inductor current and increasing the energy stored in the inductor. Then, when in off-state, both the stored inductor energy and the voltage source are forced to flow through the diode and are transferred to the load side, effectively generating a larger output voltage than the initial input voltage [14, 15]. The ratio between the on- and off-sate of the boost converter is determined by the duty cycle and acts as the main control variable. It inherently impacts the voltage input- and output ratio as expressed in equation (2.1)

$$V_{out} = \frac{V_{in}}{(1-D)}[\text{V}], \tag{2.1}$$

where V_{out} is the boost converters output voltage, [V], V_{in} is the boost converters input voltage, [V], and D is the duty cycle.

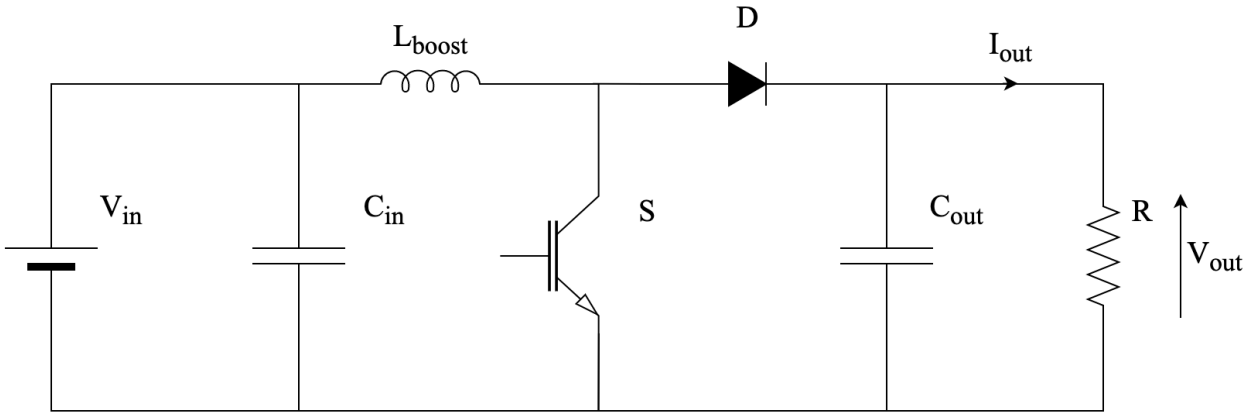

Figure 2-2 Equivalent circuit diagram of a boost converter.

The boost converter design process simply consist of fitting its equivalent circuit's components, i.e., the inductor and capacitors, in accordance with the system's specifications [16]. These components play a vital role in reducing ripple current or -voltages that occur due to the selected switching frequency. For calculating the inductor, L_{boost}, equation (2.2) can be used

$$L_{boost} = \frac{V_{in}\left(V_{out} - V_{in}\right)}{f_s \cdot \Delta I \cdot V_{out}} \text{ [H]}, \tag{2.2}$$

where f_s represents the switching frequency [Hz], and ΔI is the ripple current [A]. It is crucial to consider that the higher the inductor value, the higher is the maximum output current as a result of the reduced ripple current [16]. An appropriate estimation for the ripple current is between 20 to 40 % of the output current [16].

The input capacitor, C_{in}, positioned in parallel to the voltage source, acts as the boost converters voltage input filter [16]. This stabilization may be necessary due to the noise originating from the switching power supply. If there is a significant, unwanted ripple voltage on the input source, the value of the input capacitor should be increased in accordance with the recorded input voltage noise.

The boost converters output capacitance, C_{out}, is essential for ensuring the converter's output ripple voltage is reduced to an acceptable range and can be calculated by applying equation (2.3),

$$C_{out} = \frac{I_{out}\left(V_{out} - V_{in,min}\right)}{f_s \cdot \Delta V \cdot V_{out}} \text{ [F]}, \tag{2.3}$$

where I_{out} is the output current [A], and ΔV is the ripple voltage [V] [16].

2.1.2 Bidirectional DC-DC Converter

The buck-boost DC-DC converters are among the most common designs used for both step-down and step-up DC conversion. These converters are extensively used with applications such as batteries, fuel cells, or supercapacitors, where bidirectional power transfer between two DC sources is required in either direction [17]. In order to commence bidirectional conversion, a well-established practice is to use a combination of the buck- and boost converter in the same circuit. Replacing their diodes with controllable switches, such as MOSFET and IGBT, in combination with the corresponding switching

signal, allows for bidirectional operation [18]. The buck-boost converter's equivalent circuit can be viewed in Figure 2-3. The buck mode of operation is actualized by combining the switch S_1 and the diode in S_2, while the boost mode of operation is actualized by the diode in S_1 and the switch in S_2 [18].

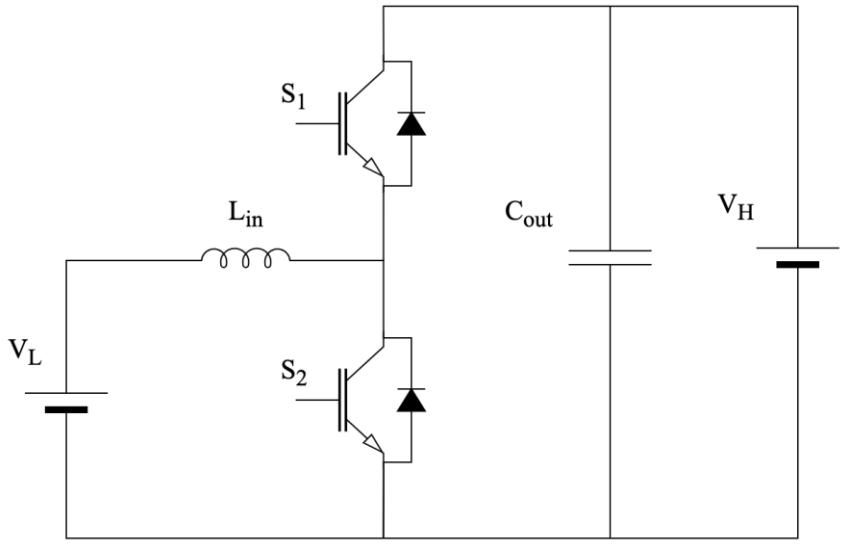

Figure 2-3 Equivalent circuit diagram of a bidirectional DC-DC converter.

Being a very versatile converter topology featuring in a broad selection of installations, including energy storage systems, the bidirectional DC-DC converted topologies is a well-researched topic. The conference paper, [19], written by Nisha Kondrath, provides an overview of the bidirectional DC-DC converters implemented with energy storage systems in microgrids. It undertakes the converter's objectives in the microgrid, such as maintaining system stability by controlling the energy storage direction and amount of power. The conference paper concludes that while the converter topology is crucial for efficient power transfer between the DC bus and the storge unit, choosing the right control strategy is of utmost importance for maintaining a stable and reliable microgrid. The utilized control strategies in this thesis are presented in subchapter 2.1.3. For the storage system to be able to provide the system with stable energy, the converters, inductor, and capacitors should be designed in accordance with the specifications of the system. The designing process of a buck-boost converter adopts the same principles as for the boost PV converter, described in subchapter 2.1.1. By utilizing the aforementioned design strategy, the inductor, L_{in}, and capacitor, C_{out}, can be well integrated, which is critical for reducing ripple voltage and -current acting in the system.

2.1.3 Control Systems

The presented PV based DC microgrid may be controlled in a multitude of ways. Both in terms of the mode of operation that the system may undertake, based on the available components connected to the microgrid, and how the overall control system may put the sub-control objectives into action. Nevertheless, it stands to mention that some control systems are viewed as near inevitable when it comes to the type of components that are integrated into the microgrid. For instance, it is common in any PV based system to inherit an MPPT controller.

MPPT Control

The optimal operation point of the PV system is identified, attained, and maintained by the MPPT controller. As the irradiation level predominantly drives the PV array's current output, the MPPT controller uses a DC-DC PV converter to establish the corresponding voltage level at the array output, which produces the largest possible power output of the system during the present conditions. The manner in which the MPPT controller is able to identify and impose the point of maximum power can be undertaken by using several different strategies or algorithms. According to a review article on the most prevalent MPPT methods, written by Motahhir, El Hammoumi, and El Ghzizal in 2020 [20], the P&O- and incremental conductance methods are the most commonly used in commercial contexts. It is argued that their ability to locate and appoint the true maximum power point at a reasonable effectivity, low price, and a low degree of implementation complexity makes up for what they lack in tracking speed compared to other, more complex strategies. The review article, [20], concludes by proposing the incremental conductance method for commercial applications whenever the tracking speed is not of the essence although the P&O method is a viable option.

As the name might suggest, the P&O method locates the true maximum power point by imposing an offset on the current operation point of the PV array, observing the effects on the power output, and imposing the following offset in the direction that suggests a higher power output. Figure 2-4 shows a simplified decision-making flowchart of the P&O algorithm. Since the algorithm operates at fixed perturbation steps and only considers one input, i.e., operation point, and one output, i.e., the power output, the implementation of this method does not require any information on the PV system at hand [21]. On the negative side, however, the P&O method's continuous perturbation of the operation point causes the power output to oscillate in steady-state, although this effect can be marginalized by reducing the fixed step size in the perturbation process. The fixed step size also represents the core of another issue of this MPPT method- reduced tracking speed [20]. This inherently reduces the algorithm's speed and, therefore, its adaptability when faced with a fast transient response [21]. The step size must therefore represent the balance between steady-state oscillations and the tracking speed.

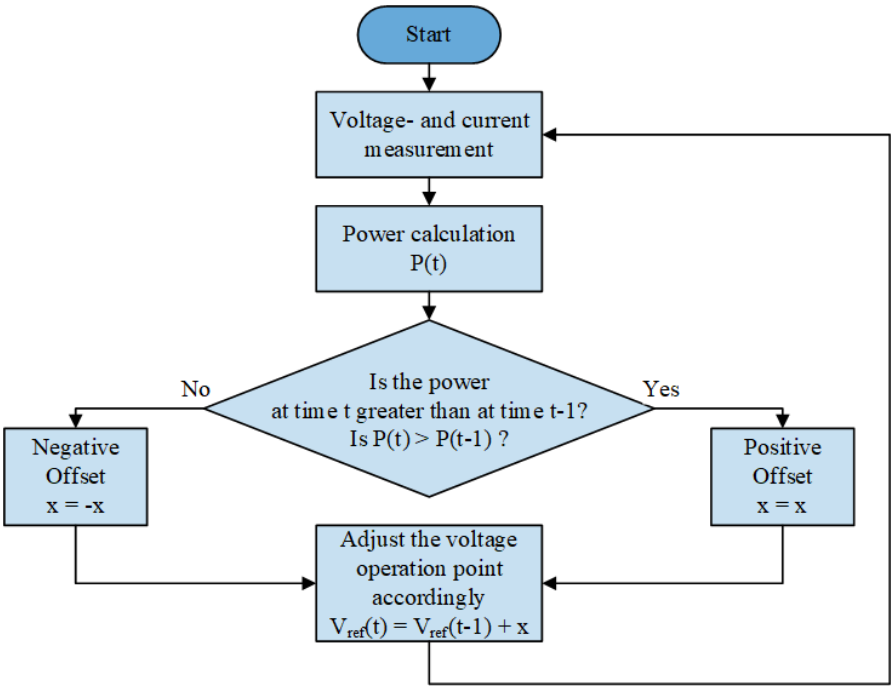

Figure 2-4 P&O algorithm flowchart

As the focus on renewable energy sources is greater than ever, the topic of operating PV systems in terms of the control strategy is frequently featured in scientific literature. Because of the immense amount of literature covering different takes on PV control, review articles such as the one previously mentioned article written by Motahhir, El Hammoumi, and El Ghzizal in 2020 [20] are particularly valuable in the pursuit of establishing the current standing on the development of the topic. By reviewing a series of peer-reviewed articles on the topic of MPPT algorithms, the article concludes that despite there are fast responding MPPT methods that imbue high efficiency, it does not make up for their cost and complexity compared to simpler methods such as the P&O method when applied in a commercial context. In an earlier study from 2016, covering the comparison of different MPPT algorithms not requiring soft computing, the authors Hlaili and Mechergui propose an MPPT algorithm that works on the premise of using the relationship between the open-circuit voltage and the temperature in combination with the relationship between the irradiation and the short circuit current with a variable step size [21]. With the use of PSIM™ software, the authors are able to use their proposed MPPT algorithm to produce results similar to the performance of the incremental conductance method. This includes step response, steady-state oscillations, and efficiency. Nevertheless, the article concludes by stating that although the proposed MPPT algorithm shows satisfactory results, the simplicity of the P&O- and incremental conductance method makes them more suitable for commercial applications. A series of optimized MPPT strategies are covered in Mohapatra, Nayak, Das and Mohanty's review article from 2017, where their scope cover MPPT strategies during partial shading of the PV system [22]. In this article, a review of previously covered hybrid or optimized MPPT strategies is conducted, showing how complex and computer-based algorithms have their benefits when faced with more complex working operations.

HES Control

Since HES systems consist of at least two forms of energy storage, often with different response times, their control system, therefore, has an equal number of constituents, reflecting their time constants. It is common for HES systems to be featured in DC microgrids, where DC-coupling architecture is implemented, whereas another primary energy source is used, and the HES system undertakes a governing role in terms of maintaining the bus voltage [23]. Alternatively, in microgrid configurations where the battery constituent of the HES system poses as the principal power source, its control system must then undertake a power-based control mode to saturate the load demand by regulating the current of the HES system [23]. Another operation mode is to assign the HES system to undertake a bus voltage governing mode, whereas alternate sources pose as the main power contributors with respect to the control system. The principal control theory to perform this control strategy uses the closed cascade feedback loop. This effectively enables the control system to address the DC bus voltage while at the same time ensuring that the power share of the battery system automatically accounts for the surplus- or deficit of energy in the bus. As shown in Figure 2-5, the cascade's outer loop regulates the DC bus error and feeds the inner control loop with a dynamic battery current setpoint. The battery current error is then regulated by the second controller and drives the PWM generator for the buck-boost converter. By regulating both the voltage and current in the same cascade, the control system is able to account for potential voltage drops as the battery discharges.

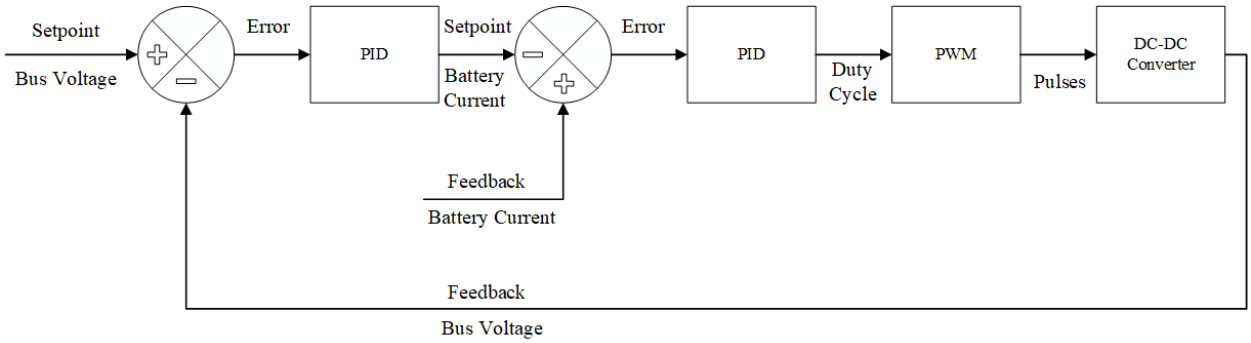

Figure 2-5 Concept control loop of the battery control system.

As mentioned above, the difference in response time between the battery system and the supercapacitor system must be encapsulated by the control system. The functionality of the supercapacitor, as a constituent of this thesis' proposed microgrid application, is based on compensating for the battery's lacking response time. In a more practical sense, it is also desirable to relieve the battery system from the stress caused by radically changing its operation, which is established to reduce the battery's lifetime [24]. It is, therefore, common to encounter HES systems containing components with a quicker response time than the battery itself, which often incorporate the bulk of the storage capacity. The HES control must therefore facilitate a function, whereas the faster-reacting supercapacitor is allowed to rapidly impose its effect on the microgrid and phase out as the battery takes over the initiative with its superior storage capacity when it is able to catch up with the load response. This can be imposed by means of several different methods, such as fuzzy logic- or rule-based control, although it is common to undertake a filter-based control [24]. One particularly common technique is high-frequency transient filtering, which is based on what control theory refers to as low-pass filtering [25]. In the instance where the HES system undertakes a governing role with respect to the DC bus voltage, it is this parameter that is filtered. The high-frequency voltage transient filtering can be derived analytically by equation (2.4) and (2.5),

$$V_{ref,bat}(t) = V_{ref,bus}(t) \cdot C_f\left(t, T_s\right) \text{[V]}, \tag{2.4}$$

$$V_{ref,sc}(t) = V_{ref,bus}(t) - V_{ref,bat}(t) \text{ [V]}, \tag{2.5}$$

where $V_{ref,bat}(t)$ represents the reference voltage of the battery controller [V], $V_{ref,bus}(t)$ represents the reference voltage of the DC bus [V], $C_f(t,T_s)$ represents the filtering function as a function of the time constant, and $V_{ref,sc}(t)$ represents the reference voltage of the supercapacitor [V] [25]. In practical terms, this means that whenever a deviation of the DC bus voltage occurs, the filtering system filters out the portion of deviations that inherits a certain time constant or deviation speed and feeds it to the supercapacitor part of the HES system. By setting the reference of the supercapacitor cascade control to zero, it will only address the quicker deviations, regulating them towards zero, while the battery part is tasked with maintaining the DC bus at its reference voltage and only being exposed to the slower deviations.

As with the case of the MPPT control, the increasing focus on renewable energy integration and streamlining the power distribution systems has resulted in a substantial amount of research being conducted on the control strategies of HES systems in recent years. Consequentially, there is a tremendous amount of scientific literature available on the topic on which this thesis capitalizes. Articles covering the control strategy and power management of HES systems containing supercapacitors and batteries in PV based microgrids are particularly relevant. Konara, Kolhe, and Sharma's article from the

spring of 2020 covers this exact topic implemented in DC couple architecture [23]. They implement both current mode control and voltage mode control in a hierarchical control architecture using filter-based control to undertake a load profile with varying time constants in a simulation program. The report concludes that this makes for a good and robust system architecture where the supercapacitor successfully helps the battery saturate the load demand. Furthermore, it is concluded that in addition to advancing the penetration of renewable energy into the power infrastructure, the proposed control system also improves system dynamics and stability and consolidates the battery's life expectancy by reducing its stress. Later the same year, the same authors, i.e., Konara, Kolhe, and Sharma, published another article on hierarchical control architecture in grid connected microgrids [25]. They showed that the filter-based control principles are also valid for AC coupled architectures. Both articles also conclude that these systems' dynamic response makes them ideal for EV charging applications and emergency power applications for disaster relief, in addition to undertaking industrial applications.

When it comes to this control principle's applicability to real-life installation, the conference paper, [26], written by Mehdi et al., has shown that the filter-based control of HES systems can realistically be applied in real-life applications. This was done by performing experiments on a test bench where the filtering control strategy was used, and both voltage- and current modes were implemented in an experimental microgrid. The experimental results were then compared to similar results from a simulation model. The conference paper concludes the experiment by stating that the system is applicable given the supercapacitor is of sufficient capacitance. A study where the HES system compensates for the dynamic fluctuations of the load sharing using fuzzy logic instead of filter-based control was conducted by Javed et al. in their article [24] from 2019. This study is particularly applicable because of its use of actual PV data from Sultanpur, India. They conclude that when sufficient data is available, the fuzzy logic approach provides a reliable yet simple and effective control system.

2.2 Synchronous Generator

Constant-speed-regulated salient pole synchronous generators are among the most popular means of producing power, be it from fossil fuels fired to produce heat and drive a turbine, a prime mover, or from renewable energy sources such as hydropower or wind power [27]. Attaining to the existing power grids, the generators strive to deliver constant AC voltage and frequency. Moreover, with the emergence of distributed energy sources in the power infrastructure, generator control systems that provide a quick response in a stable and efficient operation is particularly needed [27, 28].

There are primarily two parameters that determine the stability of a generator system [29, 30]:

- Terminal AC voltage
- Frequency

Usually, the frequency parameter is the same for the entire power system and is therefore classified as a global parameter as opposed to the terminal AC voltage output. This parameter's reference value is more likely to change from node to node in the power system and is therefore classified as a local parameter due to its dependency on the local system requirements [29]. Consequentially, this requires the two parameters to be controlled separately in different controllers.

The frequency controller relies on the proportionality between the active power input and the resulting frequency as a basis for its regulation and is therefore commonly called "load frequency control" or "automatic generation control" (AGC) [29-31]. It uses the generator shaft's rotation speed as the governing body, implementing speed governing control on the mechanical power input. By keeping the

rotation speed of the generator shaft constant at a reference value, the generator's output frequency may then be kept stable at the desired value [29-31]. In the instance of a hydropower plant, the speed governor may take the form of a flow control valve, influencing the speed of the water that drives the water turbine and thus the generator shaft. The generator's terminal AC voltage output, however, is controlled by an excitation-based controller [29, 30]. Relying on the relation between the terminal voltage and the reactive power flow, the voltage controller utilizes a field exciter to regulate the generator's terminal voltage, thus forming an excitation system [29]. The application of the excitation system in a feedback loop with the purpose of regulating the terminal voltage is also often referred to as "automatic voltage regulation" (AVR) [28-30]. Figure 2-6 shows the synchronous generator with its two control systems [30].

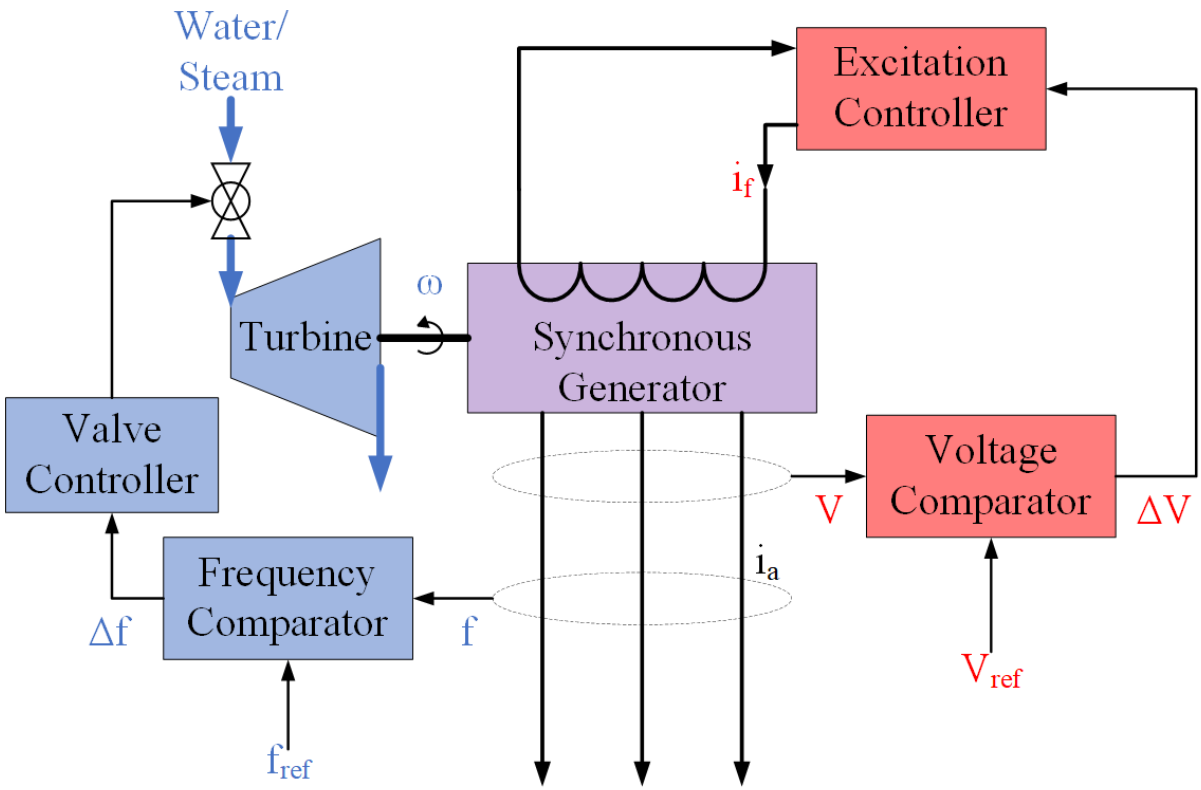

Figure 2-6 Conceptual diagram of the turbo-generator's frequency control and voltage excitation control.

The active- and reactive power output of salient pole synchronous generators, *P* and *Q* can be expressed by equation (2.6) and (2.7), respectively.

$$P = \frac{E_f \cdot V_t \cdot \sin(\delta)}{X_d} - \frac{V_t^2}{2} \cdot \left(\frac{1}{X_d} - \frac{1}{X_q}\right) \cdot \sin(2\delta) \text{ [W], and} \quad (2.6)$$

$$Q = \frac{E_f \cdot V_t \cdot \cos(\delta)}{X_d} - \frac{V_t^2}{X_d} - V_t^2 \cdot \left(\frac{1}{X_d} - \frac{1}{X_q}\right) \sin^2(\delta) \text{ [VAr]}, \quad (2.7)$$

respectively, where E_f is the source voltage [V], V_t is the terminal voltage [V], X_d is the direct reactance [Ω], Xq is the quadrature reactance [Ω], and δ is the load angle [27].

2.2.1 Automatic Voltage Regulation

As mentioned above, when the voltage excitation system is applied as a feedback loop with the purpose of regulating the generator's terminal voltage, it is commonly referred to as an AVR system. A typical configuration of the voltage excitation system applied as an AVR loop is shown in Figure 2-7 [29, 30]. The system is comprised of the following components- a voltage sensor, an amplifier, an exciter, and the generator itself. It works in the following way: A comparator is used to compare the terminal voltage reference, V_{ref}, to the terminal voltage measured by the voltage sensor, V_s. The error of the comparator is then fed through the amplifier, generating the amplified error voltage, V_A, which then drives the exciter. A common realization of the exciter is using a DC generator, whereas the amplified voltage signal, V_A, is treated as a control signal that the DC generator, or exciter, uses to derive the appropriate field voltage, V_f. The field voltage, V_f, is then applied to the generator rotors' field windings which then drives the terminal voltage, V_t, on the stator of the generator.

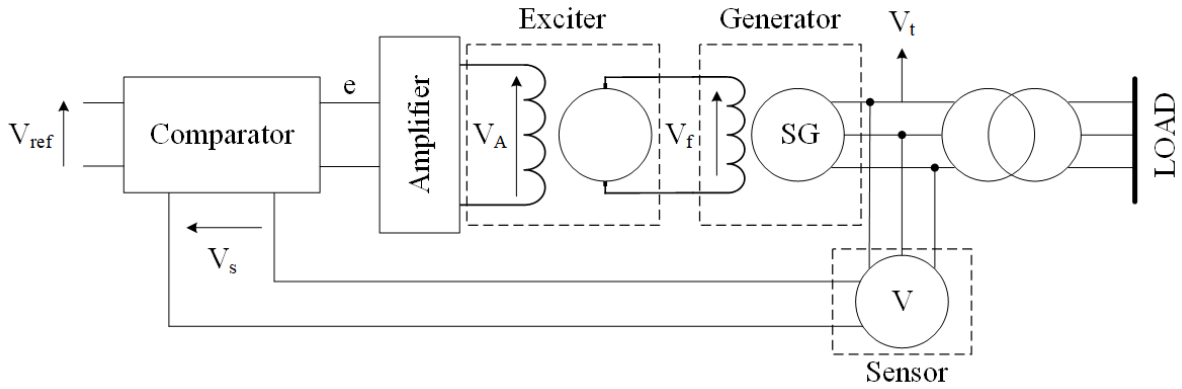

Figure 2-7 Automatic voltage regulator system.

Each of the AVR systems components' functions can be described mathematically as first-degree transfer functions, G, expressed as shown in equation (2.8).

$$G(s) = \frac{K}{1 + s \cdot T}, \tag{2.8}$$

where K is the gain and T is the time constant [29, 30]. The system can then be depicted as a block diagram, as shown in Figure 2-8, and each component's characteristics' transfer function is accounted for, forming a feedback loop [29, 32].

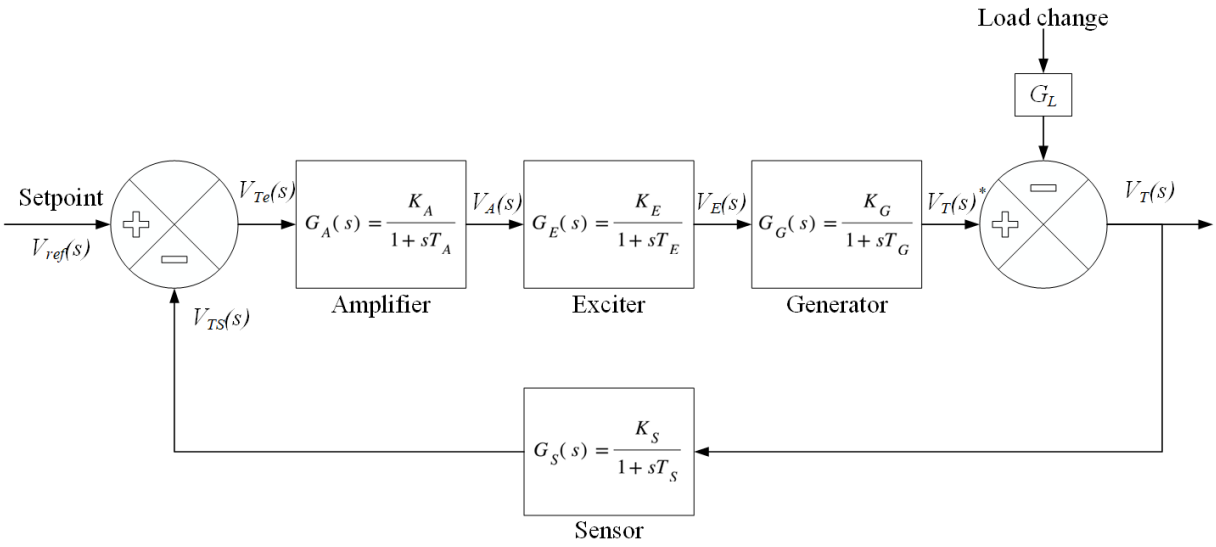

Figure 2-8 AVR system depicted as a block diagram with transfer functions.

With the use of the transfer functions, posing a linearized model of each component, the entire AVR system can mathematically be comprised and simplified into a single transfer function as shown in equation (2.9)

$$G_{AVR}(s) = \frac{V_T(s)}{V_{ref}(s)} = \frac{sK_AK_EK_GT_S + K_AK_EK_G}{(1+sT_A)(1+sT_E)(1+sT_G)(1+sT_S) + K_AK_EK_GK_S}, \tag{2.9}$$

shows this as a simplified relation between the present terminal voltage of the generator and its reference value [29, 30, 32]. However, it stands to mention that without a regulator in the feedback loop, there will persist a steady-state error in the system [29, 32]. Therefore, implementing a PID controller between the first comparator block and the amplifier is commonplace. In addition to eradicating the steady-state error, the regulator will also improve the overall dynamic response, reducing potential overshoots, rise time, and settling time [29, 32]. Figure 2-9 shows the AVR feedback loop and how it is implemented with the PID regulator installed [29, 32].

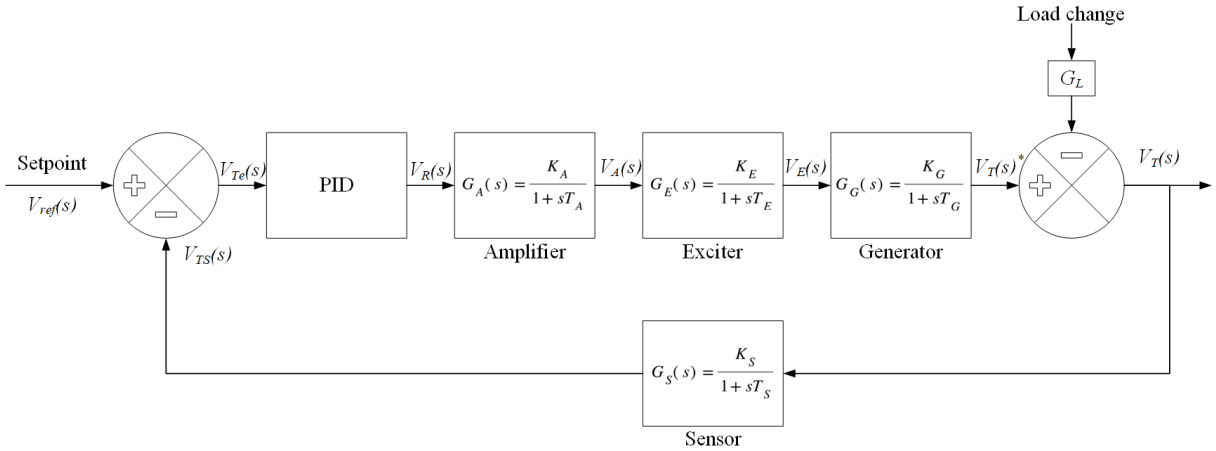

Figure 2-9 AVR system depicted as a block diagram with transfer functions and PID regulator.

The subject of AVR is a thoroughly researched topic which makes for a vast amount of available literature covering the concept. This makes research articles such as [29], written by Micev, Ćalasan,

and Oliva in 2021, particularly valuable as it provides a comprehensive analysis based on research of the vast literature available. Their article provides an analysis of AVR system design and robustness with the use of equalized optimization algorithm where, with their meticulous research of existing literature, they are able to present realistic AVR component characteristics in terms of their transfer function gains, K, and time constants, T. According to their article, amplifiers typically yield a gain, K_A, in the interval between 10 and 40, and a time constant, T_A, in the range from 0.02 to 0.1 [s], whereas the most common combination is an amplifier gain of 10 and a time constant of 0.1 [s]. The exciter, however, usually inherits a lower gain constant compared to the amplifier, whereas the former often yields a gain, K_E, in the range from 1 to 10. Its time constant often resides somewhere in the interval between 0.4 to 1 [s]. A common combination is a gain constant equalling 1 at a time constant of 0.4 [s]. The synchronous generator itself is reportedly known to yield a gain constant, K_G, from 0.7, representing no loaded generator, to a constant of 1, representing a nominally loaded generator. Its time constant, T_G, usually takes place between 1 to 2 [s], whereas the most common configuration is to set both the gain constant and the time constant equal to 1. Finally, the characteristics of the sensor usually applied for this application yield a gain constant, K_S, in the range between 1 and 2, and a time constant, T_S, ranging from 0.001 to 0.06 [s]. The authors are able to conclude that by running the AVR using the equalized optimization algorithm for optimizing the PID regulator on a system yielding these typical characteristics, they achieved an improved step response.

Furthermore, regarding the topic of what type of exciter one can utilise to impose AVR on the generator, the research article [28], written by Nøland and Lundin in 2016, provides an in-depth evaluation of the different excitation system's step time response in the context of the Scandinavian practice and requirements. They cover the most common types of exciter systems, being the static excitation system, the conventional brushless rotating system with a rotating diode bridge, an improved brushless rotating system with both a stationary and a rotating thyristor bridge, a conventional 3-stage permanent magnet system with a rotating diode bridge, a 2-stage permanent magnet system with rotating thyristor bridge, and finally, a 2-stage permanent magnet system with a rotating IGBT chopper. The authors conclude, through experimental no-load tests along with simulation tests, that both the classical- and the permanent magnet exciter with a rotating thyristor bridge are able to satisfy the requirements set by Statnett and Svenska Kraftnett, i.e., 90 % of a 0.05 per unit step response within 0.5 seconds. On the other hand, the brushless exciter configuration with a rotating diode bridge did not satisfy the requirements.

2.2.2 AC-DC Rectifier Bridge

In order to Conjoin AC components to a DC microgrid an AC-DC conversion is required. In the case of the hydropower generator, this allows for its produced power to be imposed onto the DC bus. The conversion process from AC to DC is known as rectification, where the periodically reversing direction of alternating current is converter over to one direction flow [14].

A common solution for three-phase rectification is through using the three-phase diode rectifier bridge shown in Figure 2-10 [33, 34]. This design is usually selected for its straightforward construction and inexpensive components. The circuit primarily consists of two groups of three diodes positioned at the top and bottom levels. The top group has their cathode side interconnected while the bottom group are connected on their anode side. Thereby, the connected diode on the top with the highest positive voltage will conduct while the other will not, due to be reverse bias [14]. As for the bottom group of diodes, the connected diode with the highest negative voltage will conduct. With this sequential exchange between the diodes, there is always at least one conductive diode in each group to facilitate the flow of the a DC current, i_{dc}.

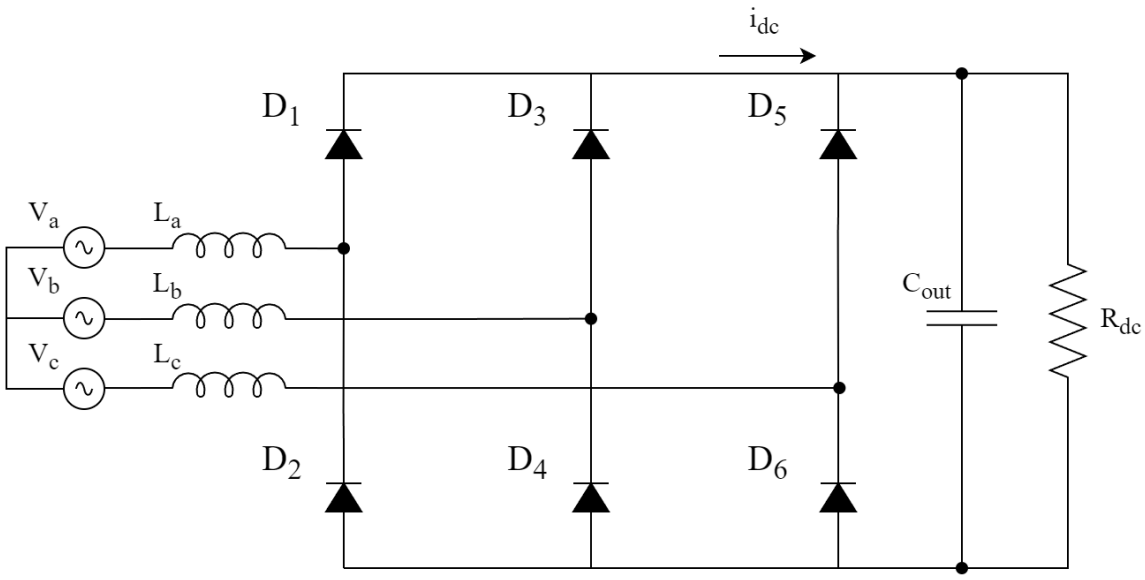

Figure 2-10 Three-phase diode rectifier bridge.

With the principle described above, the voltage waveforms conversion for an ideal case is shown in Figure 2-11. It shows how each diode conducts for 120º, but since there always are two diodes conducting, each pair of diodes will conduct for 60º rather than 120º.

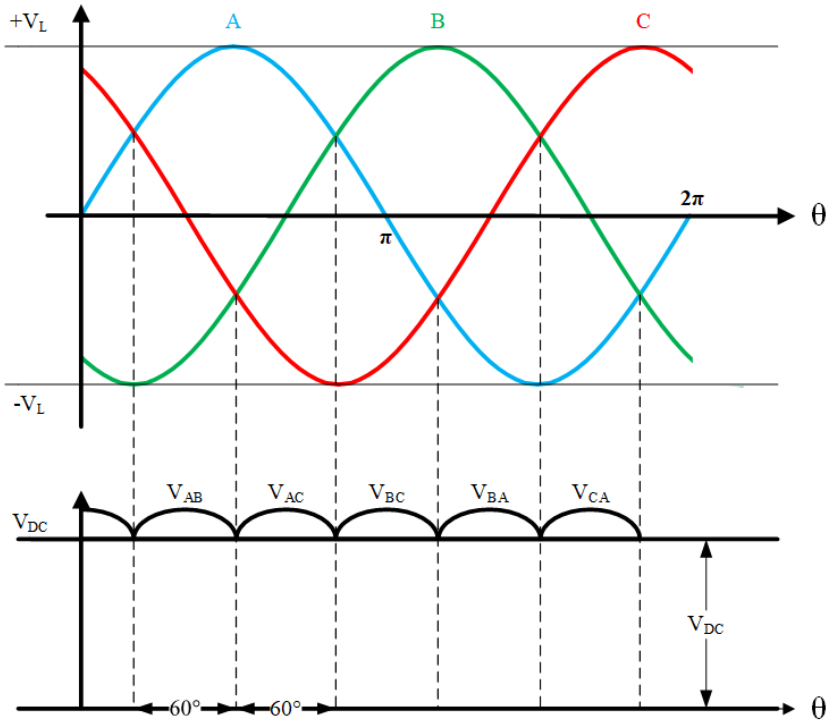

Figure 2-11 Three-phase diode rectifier bridge conduction waveform.

The average value of the DC side voltage can be described mathematically by considering a 60º segment in the DC waveform shown above using equation (2.10)

$$V_{DC} = \frac{1}{\pi/3}\int_{-\frac{\pi}{6}}^{\frac{\pi}{6}} \hat{V}_{LL}\cos\theta \cdot d\theta = \frac{3}{\pi}\hat{V}_{LL}\ [\mathrm{V}], \tag{2.10}$$

where $\hat{V}_{LL}$ is the peak line to line voltage [V] [14].

While the three-phase diode bridge rectifier is an effective and inexpensive solution for AC-DC conversion, its passive design makes it unable to assume control of the DC output. A PWM switch-based topology, however, is a more comprehensive alternative which enables controlling the converter's output [33, 34]. This type of converter is usually referred to as an active rectifier and can consist of several series-connected PWM controlled switches, such as IGBTs or MOSFETs, to regulate the rectification procedure. This type of rectifier has been researched and implemented in various applications, where several researchers has discussed their operation in their research. The research article, [33], written by de Freitas, Menegáz and Simonetti in 2016, reviews various rectifier topologies used with synchronous generators. The paper focuses on the AC to DC stage and compares the characteristics of numerous rectifier topologies such as diode bridge-, multilevel- and matrix converters. It discusses the six-switch converter operating as one of the predominantly used choices for its high-power factor rectification.

An illustration of the three-phase full-bridge two-level AC-DC rectifier is shown in Figure 2-12. The PWM signal is generated by a VSR controller in order to provide the desired DC voltage level. The VSR controller is presented in more depth in subchapter 2.1.3.

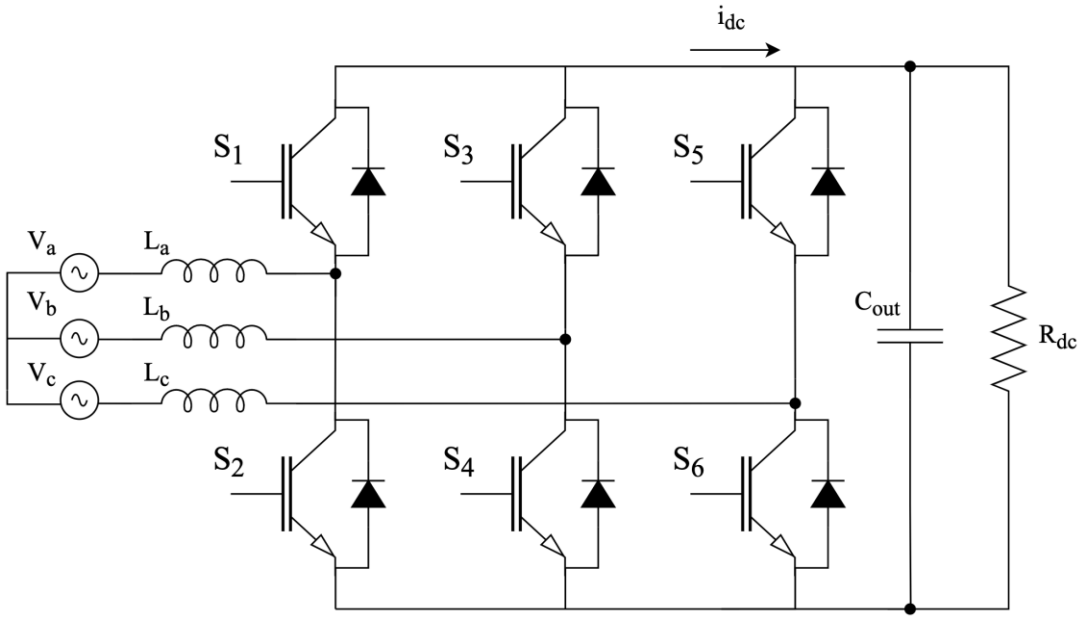

Figure 2-12 Circuit diagram of a full-bridge two-level AC-DC rectifier.

The high switching frequency originating from the PWM- signal generator can contaminate the microgrid with a high order of harmonic pollution [35, 36]. This can directly affect the power quality of the generator, which can have further ramifications on sensitive equipment residing in the system. In order to diminish the switching noise, a common strategy is to install a passive filter between the AC-DC converter and the generator. The L-filter design is commonly used with converters having a high switching frequency and a brief attenuation [35, 36]. For reducing high amounts of current harmonics, a high value of inductions should be incorporated, but to high can become quite expensive.

In order to properly intergrade the L-filter, the inductions value have to be determent in accordance with the systems specifications [35]. This is realized by calculating the phase current, i_{phase} [A], as a function of power, P [W], and the phase voltage, v_{phase} [V], with equation (2.11).

$$i_{phase} = \frac{P/3}{v_{phase}} [\text{A}]. \tag{2.11}$$

Thereby, based on the systems maximum voltage drop, which is limited to 20 % of the phase voltage, the maximum induction, $L_{Filter.max}$, can be obtained using formula (2.12) [35],

$$L_{Filter.max} = \frac{0.2 \cdot v_{phase}}{2 \cdot \pi \cdot f \cdot i_{phase}} [\text{H}], \tag{2.12}$$

where, f is the frequency [Hz]. The L_{Filter} is selected based on the calculated $L_{Filter.max}$. With valid filtering adjustments, the harmonics distortion can be reduced, resulting in a smoother sinewave on the AC side.

2.2.3 VSR Control

A commonly employed control system for active VSRs is PWM based control that utilises the voltage oriented control method to configure the pulses of an active full-bridge's IGBT switches to attain the DC voltage setpoint [37]. The control method is derived from the control of three-phase induction motors, which is based on controlling the flux producing components separately from the torque producing components with vector control. Similarly, the vector control approach used in VSR controlled convert's three-phase voltages and line currents into a stationary reference frame based on the grid frequency, introducing the dq frame [37]. This allows controlling the reactive- and active power separately, much like the flux and torque in the induction motor control [37]. An outer control loop is used to attain the DC bus voltage and sets the operating point for the active power component of the dq-frame [37, 38]. The inner control loop, in charge of the active- and reactive power components, i_d and i_q, forms the framework for a reference voltage waveform which is then used to drive a PWM generator that in turn drives the active rectifiers IGBT switches [37, 38].

As mentioned above, the control system requires the control parameters, i.e., voltage and current, to be transformed into the dq-frame through park transformation. This is done with the use of equation (2.13),

$$\begin{bmatrix} d \\ q \\ 0 \end{bmatrix} = \frac{2}{3} \cdot \begin{bmatrix} \sin(\theta) & \sin\left(\theta - \frac{2\pi}{3}\right) & \sin\left(\theta + \frac{2\pi}{3}\right) \\ \cos(\theta) & \cos\left(\theta - \frac{2\pi}{3}\right) & \cos\left(\theta + \frac{2\pi}{3}\right) \\ \frac{1}{2} & \frac{1}{2} & \frac{1}{2} \end{bmatrix} \cdot \begin{bmatrix} a \\ b \\ c \end{bmatrix}, \tag{2.13}$$

where the time-variant three-phase voltage- and current components, v_{abc} and i_{abc}, are transformed into a two-phase orthogonal coordinate system with the basis on an imposed rotation θ, resulting in the components- v_d, v_q, i_d, and i_q [39]. The imposed angle, θ, is usually determined in relation to the frequency of the AC waveform by the use of a "Phase Locked Loop" (PLL) [40]. Figure 2-13 shows the geometric relationship between the three-phase abc-projections and the Park transformed dq-projections with angle θ [41].

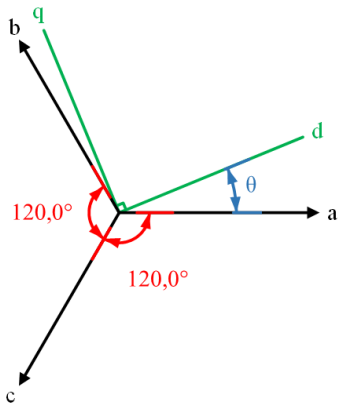

Figure 2-13 Projections of Park transformation.

The orthogonal nature of the dq-projections allows the current and voltage to be expressed as complex numbers, whereas the d-phase represents the real component and the q-phase represent the imaginary component so that the voltage can be expressed with equation (2.14)

$$v_s = v_d + j \cdot v_q [\mathrm{V}], \tag{2.14}$$

and the current with equation (2.15).

$$i_s = i_d + j \cdot i_q [\mathrm{A}]. \tag{2.15}$$

This allows the Kirchhoff's voltage law, applied to the active rectifier, to be expressed, showing the mathematical relationship in equation (2.16)

$$L \cdot \frac{di_d}{dt} + R \cdot i_d - L \cdot \omega \cdot i_q + v_d = u_d [\mathrm{V}], \tag{2.16}$$

for its active component and equation (2.17)

$$L \cdot \frac{di_q}{dt} + R \cdot i_q + L \cdot \omega \cdot i_d + v_q = u_q [\mathrm{V}], \tag{2.17}$$

for its reactive component, where u_d and u_q are the rectifiers output voltage's d and q components, L is the total line inductance, R is the total line resistance, ω is the reference angular frequency, and v_d and v_q are the active- and reactive voltage references [37, 38]. Since each term in the equation described in equations (2.16) and (2.17) are time-variant, it is common to use a closed-loop regulation to account for the system's varying nature [37]. The conversions in equation (2.18)

$$L \cdot \frac{di_d}{dt} + R \cdot i_d = \left(K_p + \frac{K_i}{s} \right) \cdot \left(i_{d,ref} - i_d \right) [\mathrm{V}], \tag{2.18}$$

And equation (2.19)

$$L \cdot \frac{di_q}{dt} + R \cdot i_q = \left(K_p + \frac{K_i}{s} \right) \cdot \left(i_{q,ref} - i_q \right) [\mathrm{V}], \tag{2.19}$$

for the active- and reactive current regulators, respectively, can then be applied, forming the basis of the feed-forward decoupling control shown in Figure 2-14 [37].

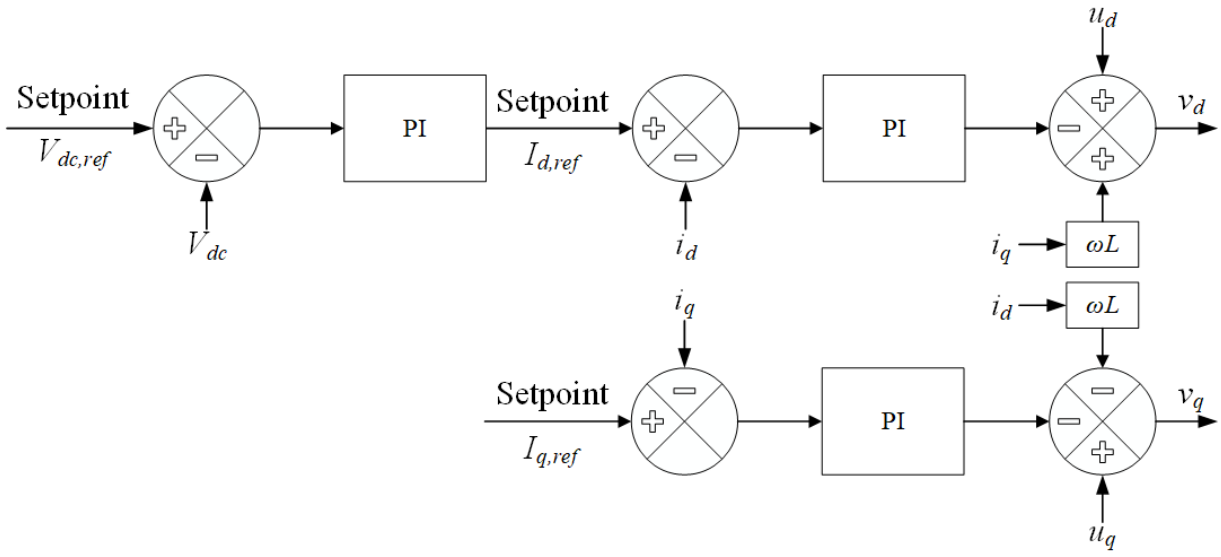

Figure 2-14 VSR controller's feed-forward decoupling control.

The reference voltage waveform is continuously generated in the dq-frame as the feed-forward decoupling controller's output, satisfying the relationship in equations (2.16) and (2.17), while simultaneously incorporating the necessary current values along with the active- and reactive voltage drops across the inductor and the resistor [37, 38]. However, in order to impose the reference voltage waveform to the PWM generator, it must be transformed into three-phase a-, b-, and c- components. An inverse Park transformation can then be used, aligning the a-phase to the q-axis, re-introducing the phase angle, θ, and imbuing a ± 2π/3 radians phase shift between the phases [39]. Mathematically, this can be expressed by equation (2.20)[39]

$$\begin{bmatrix} a \\ b \\ c \end{bmatrix} = \begin{bmatrix} \sin(\theta) & \cos(\theta) & 1 \\ \sin\left(\theta - \frac{2\pi}{3}\right) & \cos\left(\theta - \frac{2\pi}{3}\right) & 1 \\ \sin\left(\theta + \frac{2\pi}{3}\right) & \cos\left(\theta + \frac{2\pi}{3}\right) & 1 \end{bmatrix} \cdot \begin{bmatrix} d \\ q \\ 0 \end{bmatrix}. \tag{2.20}$$

By using two-level PWM, the reference voltage waveform is used to drive the rectifier's IGBT switches. This is done by running the sinusoidal reference voltage waveform over a triangle carrier signal. Each intersection between the carrier signal and the sinusoidal a-, b-, or c-phase then marks the width of the pulses of the PWM generator [42].

Figure 2-15 shows a conceptual sketch of how the three-phase pulse width modulation is carried out in relation to the intersections between the phases and the carrier signal [42]. Doing this continuously based on the reference voltage allows the creation of pulses that incorporates the entire VSR control mechanisms.

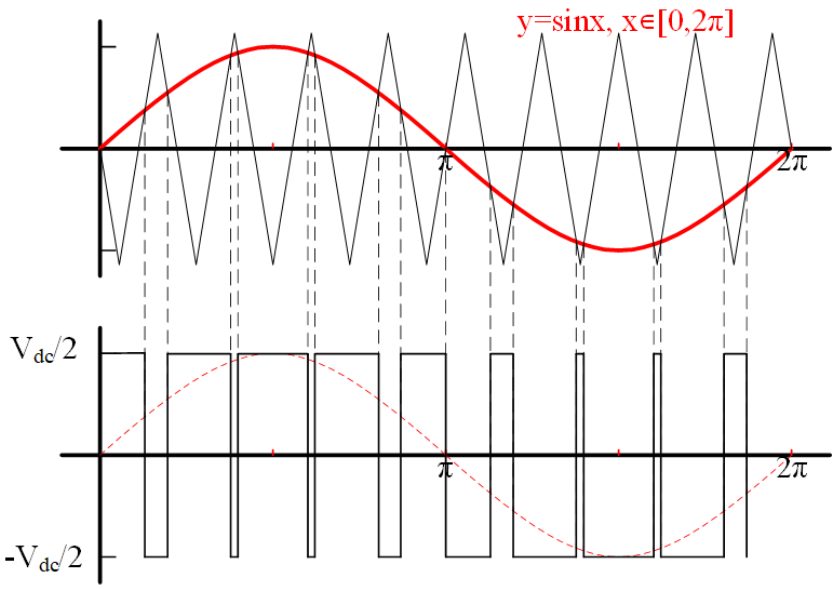

Figure 2-15 Two-level pulse width modulation concept sketch.

2.3 Hierarchical Control Theory

It is widely accepted that hierarchical control theory is necessary in order to properly conjoin microgrid components that inherit different characteristics, namely time constants, response times, or bandwidths [43-46]. It's the ability to overcome this complication, along with facilitating a varying control objective along the system architecture, that makes hierarchical control theory the pervading control theory for micro- and smartgrid control with the implementation of the following control levels:

- Primary level.
- Secondary level.
- Tertiary level.

In short, the hierarchical control theory is based on obtaining its objectives by breaking down complex problems into smaller, less complex sub-problems and rearranging them into a hierarchical system [43]. The sub-problems, i.e., Underlying control systems and components, are arranged hierarchically in a structure resembling a tree where objectives, tasks, and commands, carried out by the control system, move down the hierarchy from superior to subordinate nodes. Oppositely, perceived data and parameters at the bottom of the hierarchy travel upwards to the top nodes, allowing the decision-making organs at the top of the hierarchy to perform based on information inputs. Figure 2-16 shows a conceptual sketch of the control hierarchy where the nodes make up a tree shape and the response time of the nodes increase along the hierarchy [46].

Another distinguishing feature of this control theory with regards to the vertical relations along the hierarchy is that even though the lower-level nodes are conducted by the superior nodes, they can also perform their own sub-control objectives separately [46]. In the context of smartgrid system architecture, this means that a control node of the physical layer can separately ensure the continuous function of the primary control mechanisms while accommodating directions from the tertiary control in the application layer, facilitated by the secondary control through the network layer.

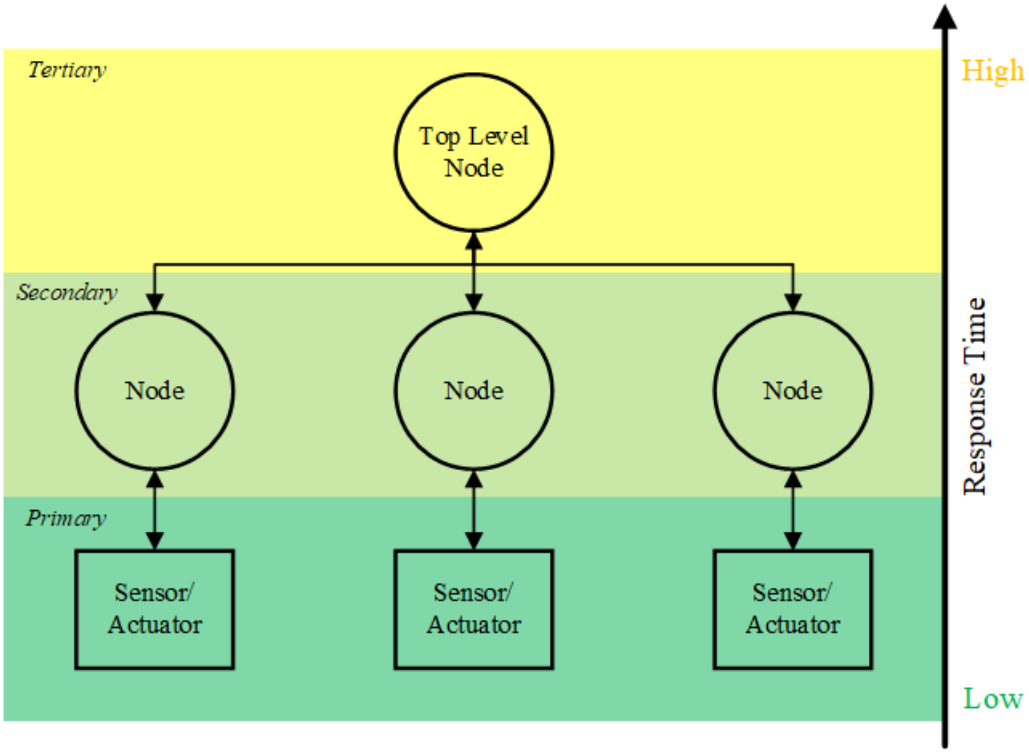

Figure 2-16 Hierarchical control topology.

2.3.1 Primary control

As shown in Figure 2-16, the most fundamental level of the hierarchical control topology is the primary control. This control level is usually dedicated to tending to the physical layer's most basic needs or the requirements for the system to be classed as workable. In the context of a DC microgrid operation, the primary control is tasked with maintaining the voltage level across the DC bus. For instance, if the DC bus contains a battery system, the primary controller could be tasked with operating a DC-DC buck-boost converter with the objective of regulating the DC bus voltage while saturating the load demand. The buck-boost converter's short time constant, i.e., the switching frequency, ensures a fast response time if the system experiences a sudden change of load or DC bus voltage level [47]. This is also an example of the primary level using a multi-objective controller [47]. In this thesis' instance, the energy storage systems and VSR controller are mainly controlled in the primary control level with regard to voltage stabilization.

In addition to maintaining the DC bus, the primary control level is also responsible for facilitating the power sharing between the microgrid's components [45, 48]. There are primarily three strategies for accomplishing this:

- Passive load sharing.
- Active load sharing.
- Hybrid passive- and active load sharing.

A passive load-sharing scheme shares the load between the parallel-connected converters based on the components' capacity [49]. This is achieved using droop control and is a fairly popular strategy of paralleling multiple energy sources, although it is susceptible to reference drift and is a somewhat inferior load regulation [50]. The active load sharing scheme, however, uses a master-slave based

regulation to share the load. Whatever power module is selected as the master will then handle loads within its rating as if it was working singly as the only module until the load supersedes its capacity, in which case the discrepancy will be covered by slave modules, automatically supplying a power proportional to their capacity [50].

Primary control in microgrids is a subject that has been significantly researched over the later years as a consequence of the emergence of smart technology. The subject is therefore well covered in the literature in articles, reports, and conference papers. Particularly interesting is the primary control level's role in voltage- and current regulation with power electronic equipment in the context of the surrounding hierarchical control in microgrids. Dudiak, Conka and Kolcun cover this exact topic with the implementation of renewable energy sources and energy storage systems in their article, [47]. Furthermore, with the prominence of DC microgrids in newer grid installations, the topic of DC-DC control and topologies are also highly relevant with regard to primary control systems. The conference paper, [49], written by Dahale, Das, Pindoriya and Rajendran, provides an excellent overview of this and explores different load sharing strategies, especially for DC microgrids. In more recent times, the need to integrate the beforementioned sections of literature into one overall control hierarchy theoretical basis has been a hot topic within the subject. With regards to this, one can highlight [45] as an excellent review article written by Yamashita, Vechiu and Gaubert, where they especially emphasise the hierarchical control for building microgrids and how one can carry out a variety of control strategies across every level of the hierarchy.

2.3.2 Secondary control

As a moderator between the primary- and the tertiary control level, the secondary level is generally tasked with providing the necessary stability to comply with the public grid. It also includes facilitating more complex operations such as load predictions, weather forecasting, or power trading for the application layer. In microgrid installations, the secondary control level usually operates between the microgrid's physical layer and the public grid, regulating the voltage and frequency towards certain stability requirements, benefitting from the primary control level's own robustness and stability [47]. Being the mediator of the surrounding control levels, the secondary control level also rectifies any discoordination between the top layer functions and the physical layer, e.g., power mismatches or alterations of control strategies [45]. As shown in Figure 2-16, the control level inherently incorporates a higher response time than the subsequent level and can vary from seconds to minutes, dependent on its magnitude. When it comes to implementing the secondary control level into the control hierarchy, there are generally two topologies to follow [45]:

- Centralized control topology
- Decentralized control topology

Centralized control topology uses a single master controller connected to several nodes, where the master controller is singly in charge of maintaining the systems control and optimization. This inherently means that the central master controller must inhibit an exceptional data storage capacity as well as an extensive computational power [45]. Although the control system is naturally fast and precise, its considerable computational cost and its high bandwidth communication makes this topology not particularly suitable for microgrid installations over geographically large areas. Another inherent flaw in the centralized control topology is the absolute dependency on the central master controller to function for the entire system to operate at all. Figure 2-17 illustrates the centralized control topology as a conceptual block diagram.

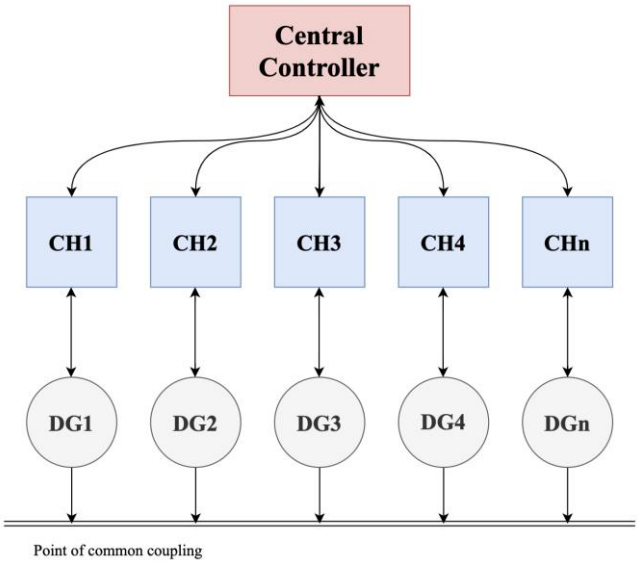

Figure 2-17 Block diagram of centralized control topology.

As opposed to the centralized control topology, the decentralized counterpart allows each node to operate individually without relying on a central master controller. The nodes are interconnected, which allows locally performed measurements and information to be shared among the nodes and enables each node to evaluate and determine the best solutions individually [45]. The absence of a central master controller eliminates the flaw of being entirely dependent on a single controller to function. In essence, this makes the system, as a whole, immune to single-point failure. On the negative side, this control topology incorporates a limited system stability compared to the centralized option. Furthermore, without any additional communication links, power electronic converters can only operate on local measurements. In general, the decentralized control topology is inherently dependent on a sufficient information flow between the nodes to pose as a viable topology option. Figure 2-18 shows the topological structure of the decentralized control option.

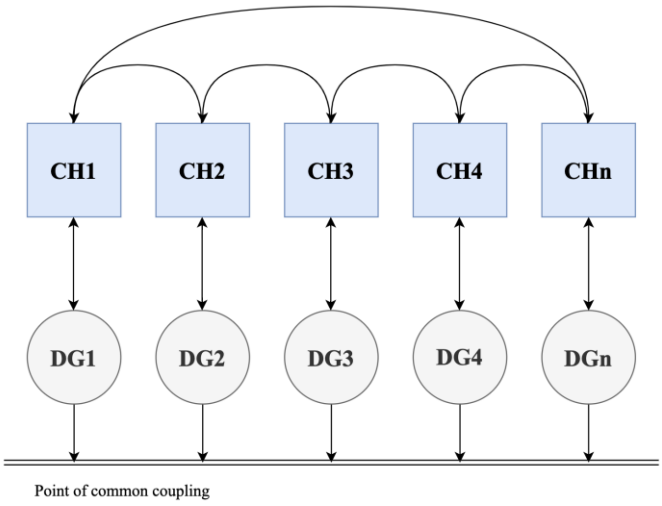

Figure 2-18 Block diagram of decentralized control topology.

2.3.3 Tertiary control

In terms of response time, the tertiary level inherits the most time-consuming control operations. Often by tapping into the application layer, the tertiary level enables the smartgrid to perform top-level mechanisms, which in turn provides each distributed generator with optimal references with regard to the infrastructural situation [45]. As for the type of data to access from the application layer, it is common for microgrid installations to access meteorological data in order to formulate a mode of operation that facilitates weather-based, non-dispatchable energy sources in the microgrid. Furthermore, as the power markets become ever more compounded and power trade serves as a source of stability and inertia for the grid, it is becoming more prevalent to adopt power market considerations in the tertiary control level of microgrids [45]. For instance, if the tertiary level is able to predict a period of high energy prices, the microgrid can prepare for this by making sure the energy storage systems in the microgrids are sufficiently charged for that period, rendering the system less dependent on grid power. Such scenarios are also advantageous from the infrastructural point of view as the public grid becomes less subject to stress.

2.4 Proposed System

With all the theoretical groundwork established in the sections above, a conjoined system of each of the constituents named above may be formed, with the use of hierarchical control approach. The proposed system for undertaking the described issue in chapter 1 is a PV based DC microgrid, using a HES system to facilitate energy storage. Additionally, a hydropower generator system in effectively added to the system in order to address the NWA concept. Therefore, the proposed system can be broken down into five subsystems:

- PV system
- Battery system
- Supercapacitor system
- Load system
- Hydropower generator system

Figure 2-19 shows the entire proposed microgrid solution this thesis undertakes in the pursuit of electrifying Norwegian DC-based industry.

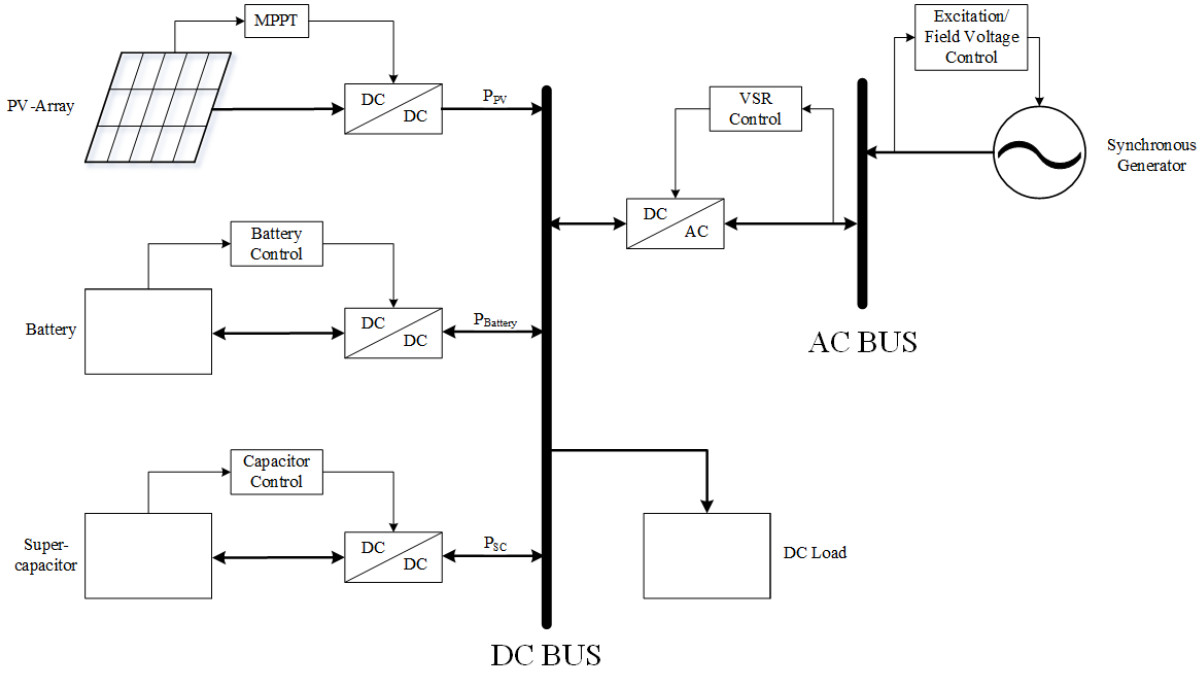

Figure 2-19 Microgrid topology of proposed system solution.

Since this thesis aims to characterize the effect of this system's physical layer alone, emphasizing the amount of power, flexibility, and system stability one can gain from it, the system does not feature a grid connection. However, technically, the operation of the AC side radically simplify the process of implementing an impending grid connection in the future.

3 Method

This chapter presents the methodology behind the simulation and analysis conducted in this thesis. First, the reasoning behind the load cases and modes of operation are established, followed by a detailed description of how the proposed microgrid model is designed. Finally, a rundown of every control system and how it is realised in the simulation model is presented in the context of the microgrid component concerned.

3.1 Preliminary Methodology Description

With a significant amount of local energy production, the implementation of distributed energy in a microgrid structure shows great promise in the context of electrifying land-based chemical industries. However, in order to inject the necessary amount of power, it is likely that several sources must be integrated into the microgrid. As these sources, along with the other components, don't necessarily inherit the same characteristics, the three-level hierarchical control structure is necessary to integrate them properly. The proposed system in this thesis implements a DC microgrid specifically because of its ability to effectively facilitate the energy storage system and to easier address DC loads. Therefore, the primary control level will work towards sustaining the DC bus voltage while also saturating a load demand, using control methods that are relevant to the present energy sources. This thesis will use a model representation of a microgrid using a realistic land-based industry scenario to analyse, characterise, and discuss the proper component- and control system application of such an arrangement. Special emphasis will be taken on how to operate the physical layer to facilitate the higher-layer mechanisms of the three-level hierarchical control structure and its ability to satisfy the requirement of electrifying a land-based industry scenario. This part will describe how the analysis of the component- and control system application is performed and how one can produce relevant results in the pursuit of this.

In order to properly analyse the microgrid's performance during different operation modes and load scenarios, a simulation model is constructed in *Simulink*™. The conceptual footing of the microgrid composition, on which the simulation is based on replicating, is shown in Figure 2-19. The outcome results are obtained by running the microgrid simulation model on the following two load cases:

- **Load case 1** subjects the microgrid model to conditions with a varying load profile and a varying solar irradiation pattern.

- **Load case 2** subjects the microgrid model to conditions with a constant, high load demand and while no irradiance is present to drive the PV system. The generator system operates at reduced capacity as well.

In load case 1, both the load profile and the irradiance are set to semi-realistic patterns in order to generate a load sharing profile suggestive of what one could expect in a real-life application. The occurring load sharing profile is then one of the parameters that determine the propriety of the suggested component- and control system application. Equally, the microgrid's ability to keep the DC voltage stable at its reference is an indicator of the validity of the selected control system application. This thesis defines an acceptable DC bus voltage deviation of ± 3 %.

The following section conveys the methodology behind constructing the simulation model used to analyse the microgrid's component- and control system application. In order to encapsulate the proposed microgrid structure's propriety in the context of saturating the load demand of a DC load based chemical industry to attain the NWA concept, i.e., the ability to electrify without major grid investments, three different operation modes are analysed by running the load cases presented above. Each of the operation modes constitutes the following three microgrid components:

- PV system with a rated effect of 100 kW operated at MPPT conditions.
- Synchronised hydropower generator with a rated effect of 85 kVA operated at nominal speed.
- Battery pack of 20 batteries with 12 V and a combined rated capacity of 290 Ah

The first and second mode of operation incorporates a HES system made of both a battery- and a supercapacitor system, whereas the third mode of operation only uses the battery system. The entire microgrid, as it is modelled in Simulink, is shown in Figure 3-1.

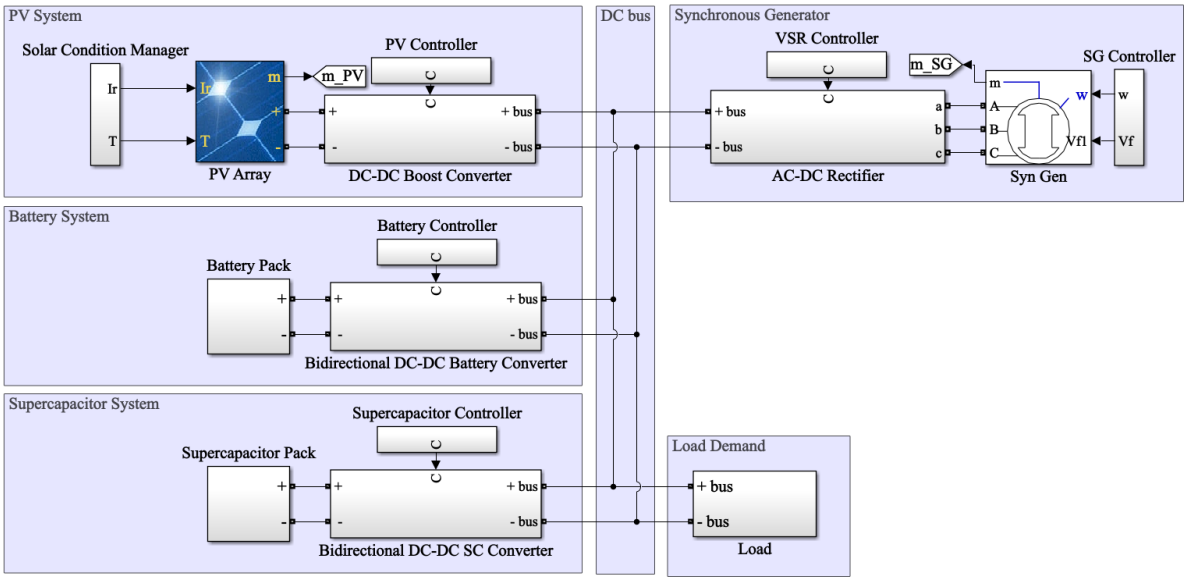

Figure 3-1 Simulation model constructed in Simulink.

3.2 Microgrid Model Design and Function

The model used to simulate the behaviour of the microgrid with the various component- and control applications consist of several subsystems interconnected with a DC bus. In order to encapsulate the behaviour during a component composition one can expect to encounter in the defined scope, the model uses a hydropower generator to represent a dispatchable energy source. Furthermore, in an attempt to attain the NWA concept, PV energy is added to represent a non-dispatchable and intermittent energy source. In order to impose a production pattern on the system, a load is added to represent the consumption of the chemical industry during production. As a means of administering a way of storing surplus energy in the system, a battery and supercapacitor are added. The system can thus be divided into the following subsystems:

- PV system.

- Battery system.
- Supercapacitor system.
- Hydropower generator system.
- Load system.

Each of the model's subsystems is described in the following sections.

As mentioned earlier, the system is designed to undertake three different modes of operation:

- **Mode of operation 1** uses the HES system to regulate the DC bus voltage while the generator system constantly operates at nominal speed and a fixed field voltage, generating a constant power during the entire operation through a passive rectifier.

- **Mode of operation 2** employs an excitation-controlled generator at nominal speed, generating semi-constant power. This mode uses a passive rectifier between the AC and DC sides and the HES system regulates the DC bus

- **Mode of operation 3** uses the generator system to regulate the DC bus voltage through a VSR controlled active rectifier. The generator operates at nominal speed and exciter-controlled field voltage based on the terminal voltage, while the battery system operates in current-mode and undertakes the saturation of the load demand.

The first load case is imposing a varying load profile to the microgrid and running the PV system with a semi-realistic irradiance pattern, whereas both the load profile and the irradiance sequence are designed to challenge the robustness of the active governing systems. This load case is intended to trigger the event where there occurs a power surplus or deficit in the DC bus due to a mismatch between total produced power and the load at the time. Since the mismatch will manifest itself as an increase in DC bus voltage, the dedicated DC bus voltage governor must then compensate for this surplus or deficit by altering its operation point. However, if the changes in the load outdo the DC bus voltage governor's response time, which is likely to happen in this load case, a spike in the DC bus voltage will occur for the duration the battery takes to catch up with the load demand. For the first and second load case, the supercapacitor system must rectify this spike, with its superior response time compared to the battery, in order to maintain the required stability of the system. However, in the third mode of operation, where the HES system is replaced with the synchronous generator, or rather, replaced with the generator's change of operation point with respect to the DC bus voltage. The second load case is a supposedly worst-case scenario representing an instance where a constantly high load over time is saturated in conditions where the PV system is unable to produce any power due to low irradiance, and the hydropower generator has a reduced production due to low precipitation. This load case is meant to indicate how the system would cope in a challenging scenario energy wise and indicate why a sufficient amount of distributed power injection into the microgrid is detrimental in order to attain the NWA concept if a sustainable operation is to be obtained. Furthermore, in order to encapsulate the supercapacitor's effect for mode of operation one and two and to help determine the most appropriate component application of the thesis, the load cases are simulated for a component application both with- and without the supercapacitor. This effectively adds up to four simulations each for modes of operation 1 and 2, while mode of operation 3 has two simulations.

3.2.1 PV System

The PV system incorporates the following:

- PV array, rated at 100 kW.
- PV boost converter.
- MPPT controller.

Since this thesis uses irradiance levels that vary over time, the solar condition manager feeds a sequential irradiation signal to the PV array model whilst the temperature is kept constant under STC, i.e., 25 °C. In order to simulate representative, real-life representations for solar power production, the PV array model uses predetermined module specifications from the PV manufacturer *SunPower™*, where the utilised module type is *SPR-305E-WHT-D*. An overview of the module's specification is listed in Table 3-1 [51].

Table 3-1 Single PV module specification of SunPower™ SPR-305E-WHT-D.

Parameter	Symbol	Value	Unit
Maximum Power	P	*305.226*	[W]
Cells per module	-	*96.000*	-
Open-circuit voltage	V_{OC}	*64.200*	[V]
Short-circuit current	I_{SC}	*5.960*	[A]
Voltage at maximum power point	V_{mppt}	*54.700*	[V]
Current at maximum power point	I_{mppt}	*5.580*	[A]
Temperature coefficient of V_{OC}	-	*- 0.272*	[%/°C]
Temperature coefficient of I_{SC}	-	*0.062*	[%/°C]
Dimensions		*1559 x 1046 x 46.0*	[mm]

With the module type described above, the PV array utilised for the simulation model uses a combination of 66 strings with five series-connected modules on each string. This results in a combined power of roughly 100 kW under standard test conditions. The resulting PV array's characteristics are presented in Table 3-2. As opposed to examining the actual component sizing, this thesis aims at the utilised DC microgrids control strategy and the component application, whereas the analysis performed in this thesis is not concerning the PV arrays sizing itself but rather its utilisation. However, this particular sizing can be justified by the area required. Using the dimensions from the table above, it can be derived that a combined area of approximately 600 m^2 is required to provide the rated capacity, which is likely to be available in sites of the application considered in this thesis.

Table 3-2 PV array STC characteristics.

Parameter	Symbol	Value	Unit
Rated Power	P	*100 725*	[W]
Open-circuit voltage	V_{OC}	*321*	[V]
Voltage at maximum power point	V_{mppt}	*273*	[V]
Nominal voltage	V_{nom}	*250-321*	[V]
Short-circuit current	I_{SC}	*393*	[A]
Current at maximum power point	I_{mppt}	*368*	[A]
Nominal Current	I_{nom}	*320-393*	[A]

The amount of power produced by the PV array is dependent on its exposure to solar irradiance, which is defined by the solar condition manager. As mentioned above, this is where the solar irradiance levels are defined. In order to realistically encapsulate the sun's daily pattern, the irradiance level is set to a

varying sequence reminiscent of this. Figure 3-2 shows the solar irradiance sequence, set by the solar condition manager, as it is implemented in the first load case of the simulation model. The fast-changing nature of the sequence helps to both underline the influence of the supplied PV power on the DC microgrid and test the robustness of the control system.

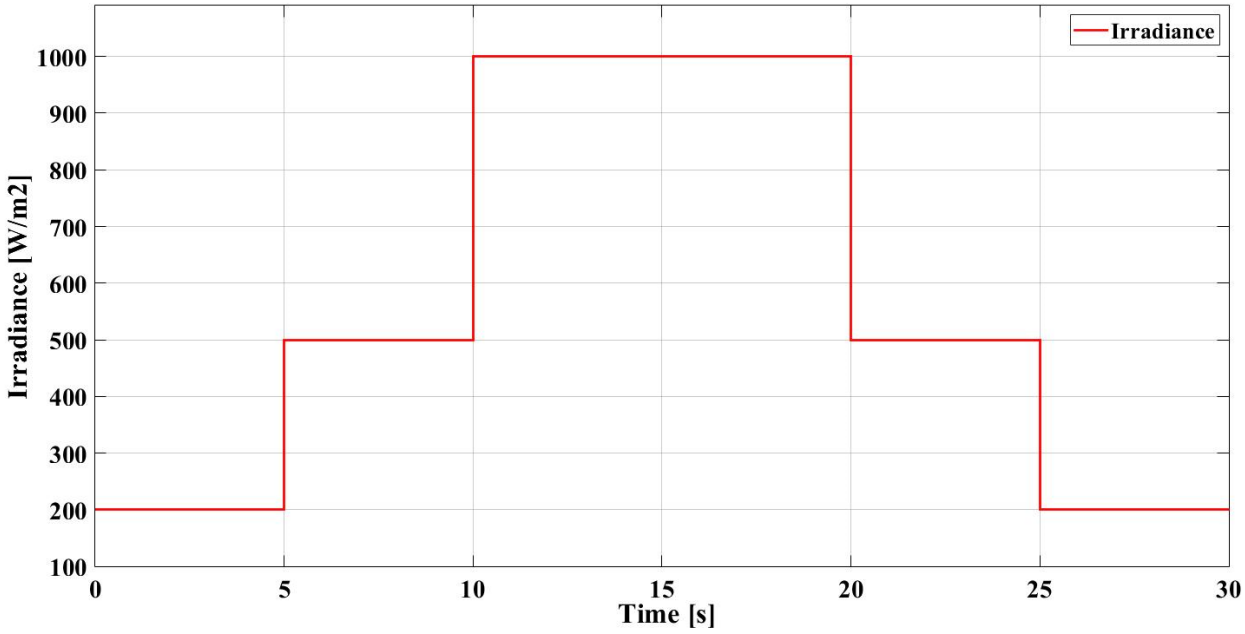

Figure 3-2 Irradiance sequence for the simulation model's sun conditions.

The PV system is assimilated to the DC bus with the help of a DC-DC boost converter. Primarily, there are two reasons for this. The first is to facilitate an operation that attains the maximum power point, and the second is to ramp the operating voltage to an appropriate level with regards to the DC bus voltage level, which is 500 V. The modelling of the DC-DC boost converter is done according to the theoretical basis presented in subchapter 2.1.1 and the equivalent circuit diagram in Figure 2-2. The PV array characteristics and the DC bus voltage reference are defined as design parameters, and the boost converter components are sized with these in mind. Figure 3-3 reveals the DC-DC boost converter as built in the simulation model.

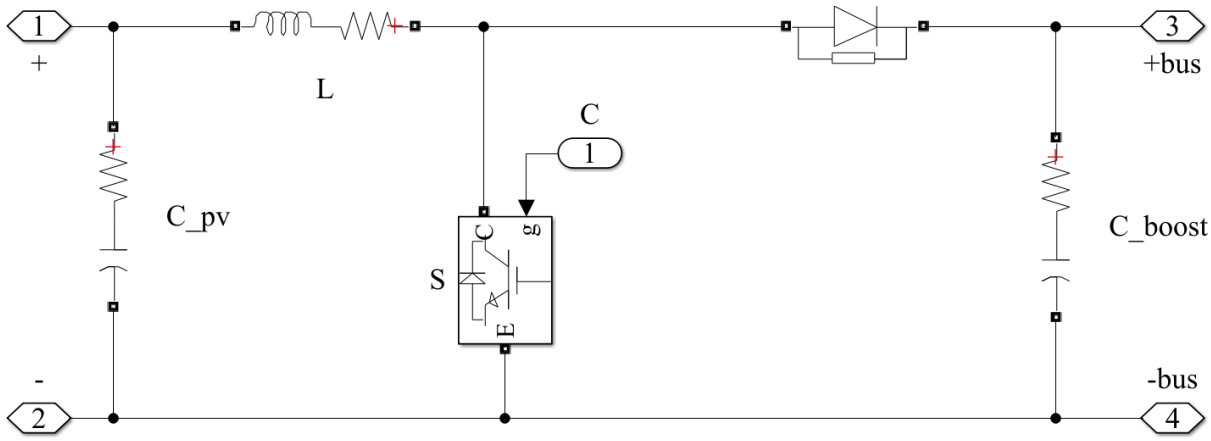

Figure 3-3 DC-DC boost converter used in the PV system simulation model.

The modelling of the boost converter involves sizing its reactive components to facilitate the desired voltage- and current levels. To do this, equation (2.2) and (2.3) from subchapter 2.1.1 is utilised with the premise of a switching frequency, f_s, equal to 5000 Hz. Additionally, the input capacitor, C_pv, is defined. Its capacitance is selected based on reducing the ripple voltage entering the converter. In order to undertake a non-ideal scenario, series resistances are added to each reactive component. This is to emulate the realistic ohmic losses incorporated in such components in real life. Table 3-3 lists the parameters concerning the PV system boost converter.

Table 3-3 Characteristics of the PV system's DC-DC boost converter.

Parameter	Symbol	Value	Unit
Input voltage	V_{in}	*250-321*	[V]
Switching frequency	f_s	*5000.00*	[Hz]
Input capacitance	C_{PV}	*100.00*	[µF]
Input resistance	R_{in}	*0.10*	[mΩ]
Inductor	L	*5.00*	[mH]
Inductor resistance	R_L	*5.00*	[mΩ]]
Output capacitance	C_{boost}	*24000.00*	[µF]
Output resistance	R_{out}	*0.10*	[mΩ]
Output voltage	V_{out}	*500.00*	[V]
Input current	I_{in}	*402.90*	[A]
Output current	I_{out}	*201.50*	[A]
Ripple voltage	ΔV	*0.30*	%
Ripple current	ΔI	*2.30*	%

To maintain the operation of the PV array at its maximum power point, the boost converter's IGBT switch requires a control signal. A P&O MPPT algorithm is then utilised to establish the operating point in which the optimal combination of voltage and current in the PV array is obtained. Figure 3-4 illustrates how the IGBT switch control signal is generated in the simulation model, whereas the MPPT algorithm, fed with the PV's voltage and current, produces a duty cycle which is further translated into pulses by a PWM generator. The PWM generator uses the switching frequency, f_s, and the sampling time of the model, *Ts*, which equals 10 µs, to generate the pulses driving the IGBT switch. The P&O MPPT algorithm is written as a MATLAB code and can be viewed in Appendix A – MPPT Algorithm.

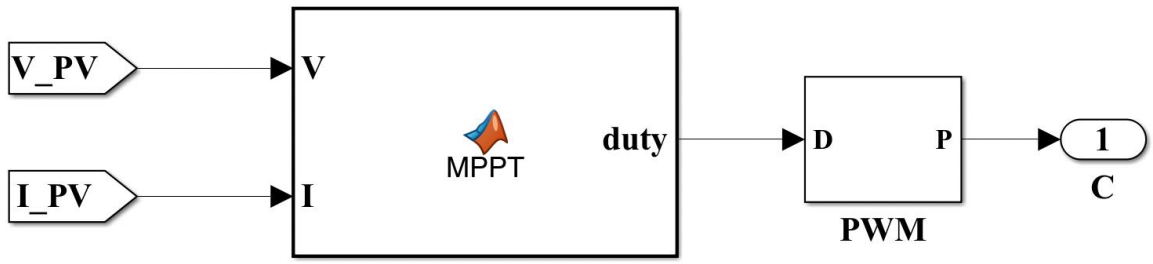

Figure 3-4 Control system of the simulation models PV system.

3.2.2 Battery System

The battery system is made of the following:

- Battery pack.
- Buck-Boost converter.
- Battery controller.

Like the PV system, the battery model selected for this subsystem is a predefined battery type defined by Simulink's battery model. Because of its relevance to the complete system, the more modern lithium-ion battery type is selected, whereas the entire battery bank is made of 20 batteries connected in series where each battery has a rated voltage of 12 V and a total capacity of 290 Ah.

The discharging- and charging characteristics, $E_{discharge}$ and E_{charge}, on which the Simulink's lithium-ion battery model is based, are explained in equation (3.1) and (3.2), respectively [52],

$$E_{discharge} = E_0 - K \cdot \frac{Q}{Q - it} \cdot i^{'} - K \frac{Q}{Q - it} \cdot it + A \cdot Exp(-B \cdot it)\ [\text{V}], \text{ and} \tag{3.1}$$

$$E_{charge} = E_0 - K \cdot \frac{Q}{it + 0.1 \cdot Q} \cdot i^{'} - K \cdot \frac{Q}{Q - it} \cdot it + A \cdot Exp(-B \cdot it)\ [\text{V}], \tag{3.2}$$

where E_0 is the constant voltage [V], K is the polarisation constant [V/Ah], Q is the maximum battery capacity [Ah], it is the extracted capacity [Ah], i' is the low-frequency current dynamics [A], A is the exponential voltage [V], Exp is the exponential zone dynamics [V], and B is the exponential capacity [Ah^{-1}].

The justification for the battery bank's sizing is twofold. The first consideration is facilitating the DC bus's reference voltage of 500 V, and the second consideration is based on how long the battery system can be expected to saturate the load demand in scenarios of lower power production from the alternative power sources. The capacity of 290 Ah is selected based on being able to saturate this simulation model's highest load demand, i.e., 69 kW, for an hour when operating with no alternative power production injecting and the battery is at full capacity. However, the emphasis of this thesis is on the analysis of the battery's component- and control system application rather than the appropriate sizing. Table 3-4 shows the battery pack's relevant characteristics according to the scope of this thesis.

Table 3-4 Simulation model's battery characteristics.

Parameter	Symbol	Value	Unit
Nominal voltage	V_{nom}	*240.00*	[V]
Rated capacity	A_{rated}	*290.00*	[Ah]
Initial state of charge	SoC_{int}	*50.00*	%

A bidirectional DC-DC converter is required in order to facilitate both charging- and discharging of the battery system. The battery system can then handle both a surplus- and a deficit of energy in the DC bus by compensating, as explained in subchapter 3.2. Utilising the theory portrayed in subchapter 2.1.2, the buck-boost converter is modelled to approach this requirement of bidirectionality. The model's buck-boost converter is constructed using the equivalent circuit diagram presented in Figure 2-3, whereas its inductor, L_B, and capacitor, C_B, are designed to reduce the ripple current- and voltage, respectively. Similar to the PV system's boost converter, the reactive components used in the battery system's buck-

boost converter are added with small resistances in order to emulate ohmic losses similar to what can be expected in a real-life installation. The model of the buck-boost converter used in this system is shown in Figure 3-5.

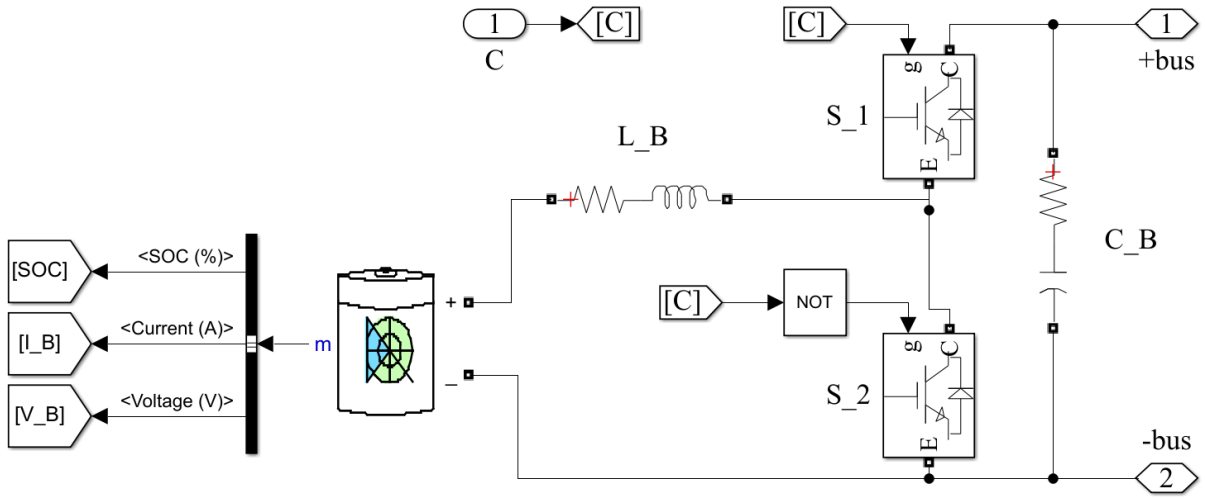

Figure 3-5 Bidirectional DC-DC buck-boost converter used in the battery system.

Based on the current mode of operation, the battery controller can undertake two different control strategies. In the first two modes of operation, the battery system is tasked with regulating the DC bus voltage and does so with the cascade feedback loop approach presented in subchapter 2.1.3 and Figure 2-5. The "outer" feedback loop in this instance regulates the error between the actual DC bus voltage and its reference value of 500 V with a PI voltage controller. Its output then drives a dynamic reference for the "inner" control loop, which regulates the battery current to its dynamic reference point with another PI controller. The current controller's output, i.e., the duty cycle, then enters a PWM generator and is translated to pulses for the IGBT switches, S_1 and S_2. Figure 3-6 shows the control loop of this control strategy as it is designed in the Simulink model, where PI_V is the "outer" voltage controller and PI_I is the "inner current controller. The voltage controller's output signal is also added a saturation limit to its parameters.

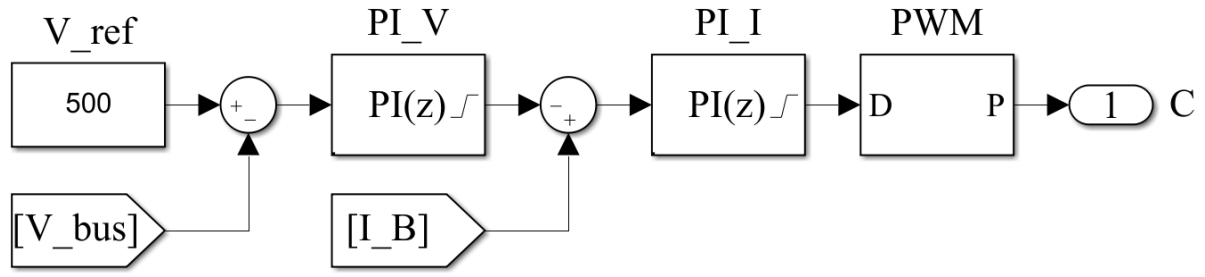

Figure 3-6 Simulation model's battery control system.

In the third mode of operation, the battery system undertakes current-mode operation. The basis of this control strategy is the same as the previous but without the "outer" voltage controller, as this parameter is to be regulated by the synchronous generator in this mode, which leaves the battery to address the load saturation. Since the power is proportional to the current, the battery's control system in this mode of operation is based on regulating towards a current setpoint which is determined by subtracting the

other power producing components from the load, thus compensating for any discrepancies in the power accounting.

For the control system to generate acceptable accuracy and transient response, the two PI controllers have to be tuned with this in mind. By applying the trial-and-error method, the parameters of the two controllers' proportional bands, P_V and P_I, can be established. To eliminate the control system's steady-state error, the integral parameter, I_V and I_I, is introduced and followed by a readjustment of the proportional bands. The PI controllers implemented proportional band, and integral parameters for every mode of operation are listed in Table 3-5. Since the third mode of operation only requires a current controller, the voltage PI controller is removed from this mode. Furthermore, since the battery pack's characteristics are unchanged throughout the different control strategies, the current PI controller inherits the same parameters across the modes.

Table 3-5 Battery controllers PI parameters.

Parameter	Symbol	Value, Mode 1 and 2	Value, Mode 3	Unit
Proportional (PI_V)	P_V	*0.850*	-	-
Integral (PI_V)	I_V	*10.000*	-	-
Proportional (PI_I)	P_I	*0.010*	*0.010*	-
Integral (PI_I)	I_I	*10.000*	*10.000*	-

3.2.3 Supercapacitor System

When the response of the load changes surpasses the response of the battery system, the supercapacitor is needed to limit the resulting DC bus voltage deviations by providing a superior response time compared to the battery. The supercapacitor system encompasses the following:

- Supercapacitor bank.
- Buck-Boost converter.
- Supercapacitor controller.

Like with the case of the battery, the supercapacitor is modelled after a specified supercapacitor function block in Simulink [53]. This is defined as a series of capacitors forming a capacitor bank. In the supercapacitor system used specifically for this simulation model, the supercapacitor bank comprises a rated capacitance of 300 F and a voltage rating of 240 V. Table 3-6 shows the characteristics of the supercapacitor used in this thesis' simulation model.

Table 3-6 Simulation model's supercapacitor characteristics.

Parameter	Symbol	Value	Unit
Rated capacitance	C_{rated}	*300.00*	[F]
Rated voltage	V_{rated}	*240.00*	[V]
Series resistance	R	*8.90*	[mΩ]
Number in series	-	*18.00*	-
Number in parallel	-	*1.00*	-
Initial voltage	V_{int}	*240.00*	[V]
Operating temperature	T	*25.00*	°C

The supercapacitor model in Simulink is based on the output voltage characteristics, V_{SC} shown in equation (3.3) [53],

$$V_{SC} = \frac{N_s \cdot Q_T \cdot d}{N_p \cdot N_e \cdot \varepsilon \cdot \varepsilon_0 \cdot A_i} + \frac{2 \cdot N_e \cdot N_s \cdot R \cdot T}{F} \cdot \sinh^{-1}\left(\frac{Q_T}{N_p \cdot N_e^{\,2} \cdot A_i \cdot \sqrt{8 \cdot R \cdot T \cdot \varepsilon \cdot \varepsilon_0}}\right) - R_{SC} \cdot i_{SC} \text{ [V]}, \quad (3.3)$$

where N_s is the number of series supercapacitors, Q_T is the electric charge [C], d is the molecular radius, N_p is the number of parallel supercapacitors, N_e is the number of layers of electrolytes, ε is the permittivity of the material, ε_0 is the permittivity of free space, A_i is the interfacial area between the electrodes and the electrolyte [m^2], R is the ideal gas constant, T is the operating temperature [K], F is the Faraday constant [V], R_{SC} is the total resistance [Ω], and i_{SC} is the supercapacitor current [A].

Like the battery system, the supercapacitor's bidirectionality is facilitated with the use of a buck-boost converter. The buck-boost converter used in the simulation model is designed according to the theory presented in subchapter 2.1.2 and the equivalent circuit showed in Figure 2-3. The resulting buck-boost converter model is shown in Figure 3-7. Resistors are added to the reactive components to mimic real-life ohmic losses.

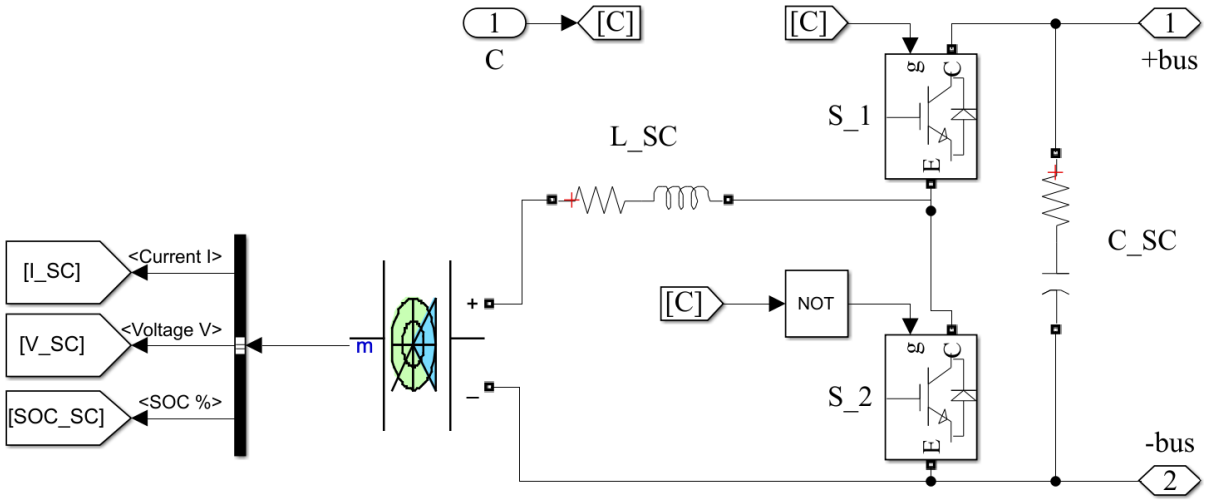

Figure 3-7 Bidirectional DC-DC buck-boost converter used in the supercapacitor system.

As the battery system is the main DC bus voltage regulator in the system's first two modes of operation, the essence of the supercapacitor's function is to accommodate or assist the battery system in accomplishing this. The operating point of the supercapacitor must never overtake the battery system fully but simply provide the benefits of a fast-reacting response time. The control strategy selected to manifest this function is called "high-frequency voltage transient filtering", where the DC bus voltage is the parameter concerned. In practical terms, this entails isolating the differentiated, quicker voltage changes in the DC bus from the slower ones. The way this is incorporated into the Simulink model is by low-pass filtering the DC bus voltage by the use of Simulink's low-pass filter block. This voltage is then used as a feedback signal to the battery controller. The differentiated voltage is generated by subtracting the low-pass filtered voltage from the original bus voltage, as shown in Figure 3-8, and is then used as a feedback signal for the supercapacitor controller. By setting the setpoint to zero, the supercapacitor controller is set to eliminate any quick changes in the DC bus to zero, while the battery controller is concerned with keeping the low frequency DC bus voltage to its reference of 500 V. As mentioned earlier, the low pass filter design is shown in Figure 3-8 and is derived from equations (2.4) and (2.5). The theoretical basis of this control method is covered in subchapter 2.1.3.

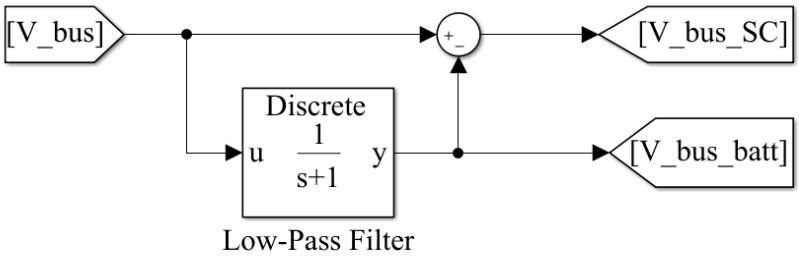

Figure 3-8 Bus voltage low-pass filter for signal differentiation.

The cascade feedback loop approach used in the battery controller is also used in the supercapacitor controller. However, as mentioned above, instead of regulating the bulk of the DC bus voltage to its rated value, i.e., 500 V, the cascade's "outer" voltage controller in the supercapacitor control system regulates disturbances, or peaks, that inherit a certain time constant. Its controller output is then treated as the setpoint of the cascade's "inner" current controller, which regulates the supercapacitor current, much like the setup in the battery controller. The current controller's output, i.e., duty cycle, then drives the PWM generator's pulse output, fed to the IGBT switches, S_1 and S_2.

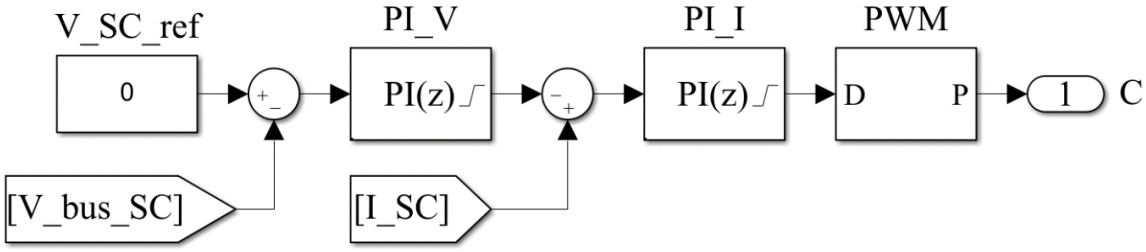

Figure 3-9 Simulation model's supercapacitor control system.

By applying the trial-and-error, the proportional gain, P_V and P_I, are determined based on the bus voltage- and power share plots. Steady-state errors in the two plots are eliminated by introducing suitable integral parameters, I_V and I_I. Preceded by the integral parameter introduction, the proportional was readjusted to achieve satisfactory results, again based on the resulting bus voltage- and power share plots. Table 3-7 shows the PI controller parameters as the model stands currently.

Table 3-7 Supercapacitor controllers PI parameters

Parameter	Symbol	Value	Unit
Proportional (PI_V)	P_V	*19.00*	-
Integral (PI_V)	I_V	*10.00*	-
Proportional (PI_I)	P_I	*0.01*	-
Integral (PI_I)	I_I	*10.00*	-

The function of the battery- and supercapacitor system utilised in the first two modes of operation is commonly merged into one, forming a HES system. Since this can make the overall HES control system exceedingly complex to describe, with all its constituents contributing to the same regulation, the flowchart in Figure 3-10 is created to give a complete overview of all the elements in the entire HES control system.

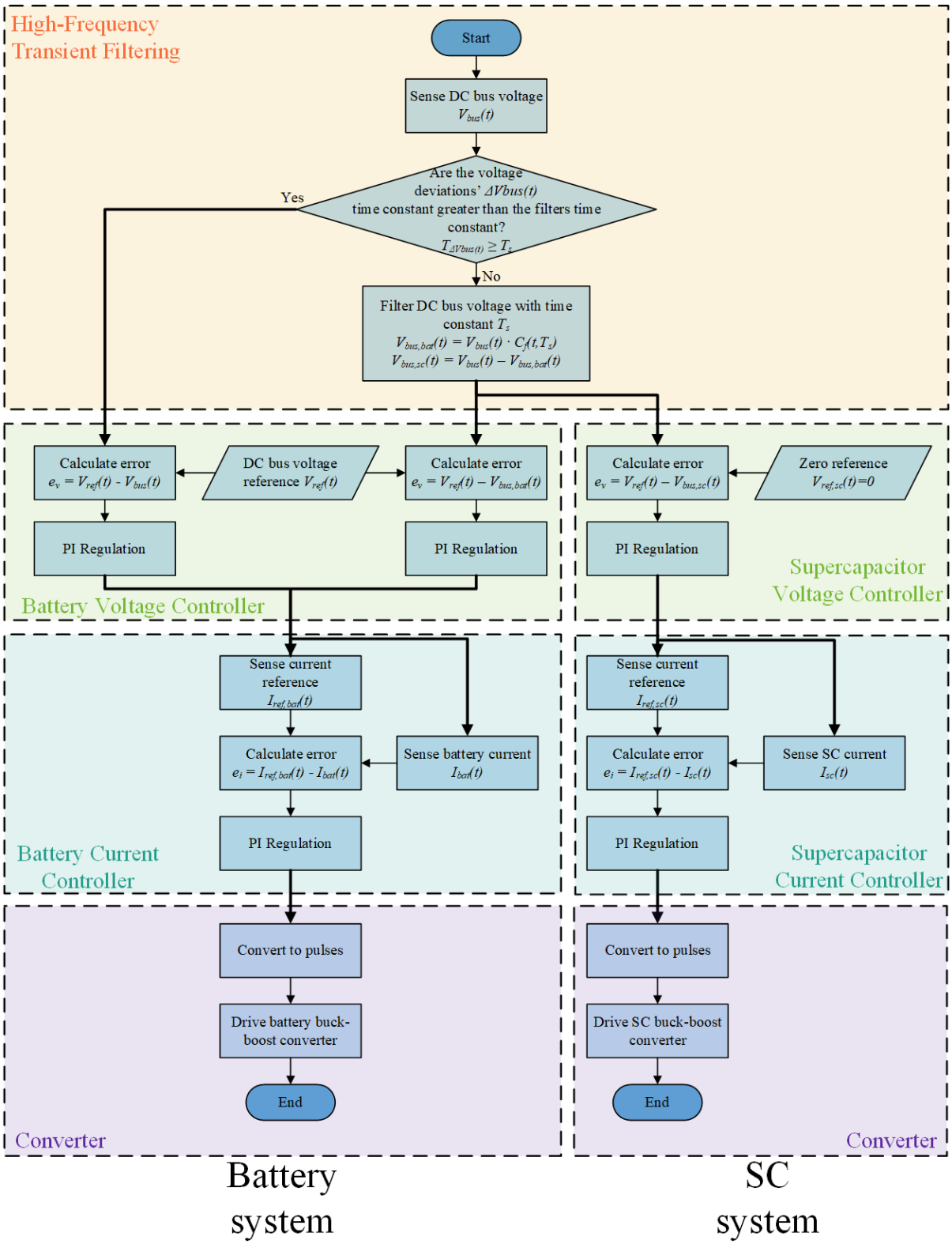

Figure 3-10 HES control system from mode of operation one and two portrayed as a flowchart.

3.2.4 Synchronous Hydropower Generator System

A synchronous hydropower generator system is utilised to represent a dispatchable energy source for the microgrid simulation used in this thesis. The synchronous hydropower generator system consists of the following:

- Salient pole synchronous generator
- Excitation system
- Rectifier (Passive for mode of operation 1 and 2, and active for mode 3)

The synchronous generator model is based on Simulink's function block called Synchronous Machine, where its parameters are programmed in per unit in order to make nominal values clearer [54]. Similar to the battery- and PV model, the synchronous generator function block allows selecting pre-set machine model parameters, which are listed in Table 3-8. The generator block has one selectable and one fixed input parameter, whereas the fixed input of the field voltage, V_f, determines the amount of excitation the generator is subject to, as explained in subchapter 2.2.1. As the selectable input type, mechanical rotation speed, ω, is selected as this represents the output of a speed governor control which drives the AGR in real installations. Locking the input speed as constant at its nominal value allows the system to undertake an ideal AGR scenario, which is desirable as the scope of this thesis aims at the generator in the context of the microgrid rather than its local governing systems. Furthermore, the emphasis of this thesis is on the component application rather than its sizing. Therefore, other than placing the hydro-generator in the "micro hydropower plant" category based on the rated apparent power, as per NVE [55], the generator size is purely based on appropriate sizing conditional to its surrounding components in this thesis' microgrid simulation model.

Table 3-8 Simulation model's synchronous generator characteristics.

Parameter	Symbol	Value	Unit
Frequency	f	*50.00*	[Hz]
Rated voltage	V	*400.00*	[V]
Rated apparent power	S	*85.00*	[kVA]
Nominal speed	n_s	*1500.00*	[RPM]
Pole pairs	N_p	*2.00*	[-]

As the first two modes of operation impose no control of the voltage fed to the DC bus from the AC bus, they both use passive rectifiers to integrate the AC side to the DC side. For simplicity, the simulation model uses Simulink's function block called "universal bridge", where the power electronic device is set to "diodes" and is therefore not controlled. Regardless of the rectifier type, the system requires a passive induction filter in order to reduce harmonics in the AC current waveforms caused by the rectifier, as per subchapter 2.2.2. The equations (2.11) and (2.12) are then used to determine the maximum value for the inductance filter, whereas the parameters used in relation to the modelled filter are listed in Table 3-9. It stands to mention that the maximum filter inductance is calculated with the nominal generator power in mind. Therefore, the actual inductance size is considerably smaller as the generator mainly operates in the 20-40 kW range. Its value is determined by assessing what values produce acceptable waveforms.

Table 3-9 Rectifier filter parameters.

Parameter	Symbol	Value	Unit
Rated power	P	*85.00*	[kW]
Phase voltage	V_{phase}	*400.00*	[V]
Phase current	I_{phase}	*70.83*	[A]
Maximum filter inductance	$L_{filter,max}$	*3.59*	[mH]
Filter inductance	L_{filter}	*2.60*	[mH]

The voltage harmonics are addressed by installing a capacitor bank between the inductance filter and the generator. It is modelled as a three-phase reactive load and imposes its reactive effect on the AC line, cancelling the residing voltage harmonics. Its value has been selected as 10 kVAr as a standard. Figure 3-11 shows the entire hydro-generator system applied for modes of operation 1 and 2.

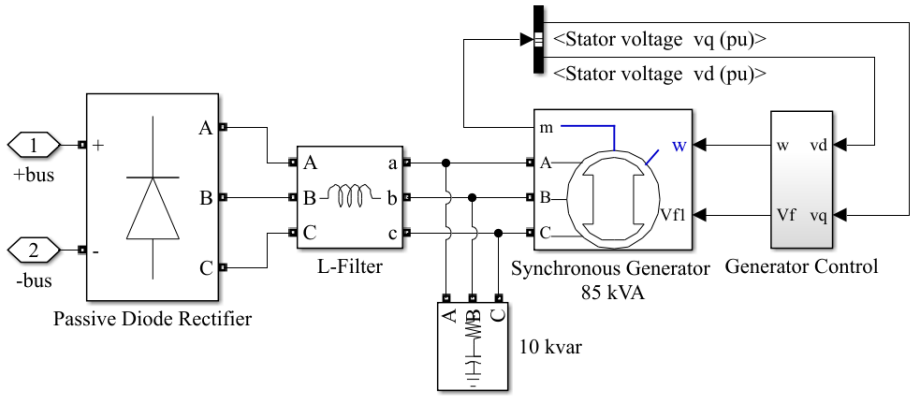

Figure 3-11 Hydro-generator model with passive rectifier configuration

For the final mode of operation, the AC bus is integrated into the DC bus with an active two-level rectifier model. Like the passive rectifier model, the active counterpart also uses the “universal bridge” function block from the Simulink library; however, for this application, the power electronic device setting is set to “IGBT/Diode”, which allows the rectifier to be controlled through a PWM signal. The passive inductance filter and capacitor bank remain the same for this configuration as for the previous one. Figure 3-12 shows the entire hydro-generator system as it is applied for mode of operation 3, with the active rectifier.

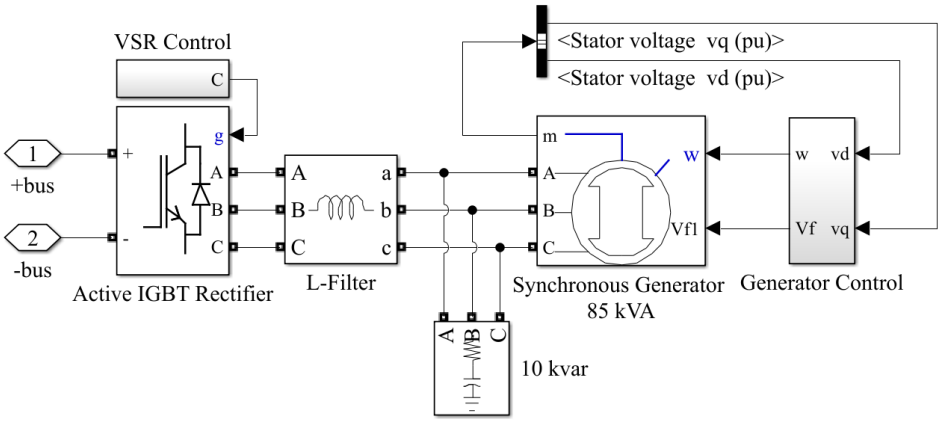

Figure 3-12 Hydro-generator model with active rectifier configuration.

Based on the active mode of operation, the hydro-generator system may undertake three different control strategies imposed by the generator controller. The first mode of operation requires the hydro-generator to inject a constant amount of power into the microgrid during the entire simulation without regard to the DC bus voltage. This is achieved by keeping the speed input, ω, constant at its nominal value, and setting the field voltage input, V_f, constant at a level which corresponds to the desired output power, whereas a field voltage input of 1.460 and 1.115 units corresponds to a generator production 40 and 25 kW, respectively as shown in Figure 3-13. The excitation system control is introduced in the second mode of operation. This allows the hydro-generator to react to the power flow in the system by altering the field voltage input automatically. Following the principles of the controlled AVR presented in subchapter 2.2.1, the excitation system controller regulates the field voltage, *Vf*, subjected to the generator based on the measured terminal voltage's d- and q component compared with terminal voltage reference, V_{ref}. When there occurs a surplus or deficit of energy in the system, the terminal voltage will consequently experience a rise or drop accordingly. The excitation system controller will then compensate for this by adjusting the field voltage, V_f, of the generator. Figure 3-13 shows the generator controller as it is implemented in the hydro-generator system model.

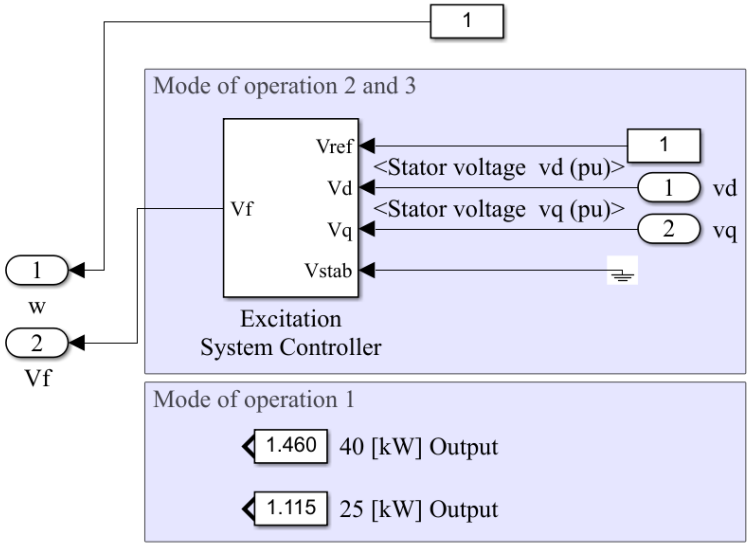

Figure 3-13 Generator controller with each mode of operation.

The third mode of operation utilises the excitation system controller in addition to the control of the active rectifier, namely the VSR controller. This mode of operation requires the hydro-generator system to function as the primary controller of the DC bus voltage, while the battery system undertakes a supplementary role in saturating the load demand. The hydropower generator's functionality in this operation mode is facilitated by applying the voltage-oriented control of the dq components of the AC current and voltage, as presented in subchapter 2.2.3 and drive the active rectifier's IGBT switches with PWM control. As shown in Figure 3-14, the VSR controller undertakes Park transformations of the three-phase AC current and voltage based on the phase angle obtained through a PLL unit. A voltage controller is then used to generate the reference value for the direct component of the current, $I_{d,ref}$, based on the error between the desired DC voltage, $V_{dc,ref}$, and the measured DC voltage V_{dc}, using a PI controller, henceforth referred to as the DC voltage controller. A comparator determines the error between the direct current reference, $I_{d,ref}$, and the measured direct current component from the Park transformation, I_d, which is regulated in a second PI controller, namely the current controller, forming a cascade with the DC voltage controller. Simultaneously, a second current controller regulates the quadrature component of the current, I_q, towards zero. The two current controllers' outputs are then used to form a reference waveform after satisfying the relationships in equations (2.16) and (2.17), using inverse Park transformation with the phase angle obtained from the PLL unit. After converting to pu, in relation to the desired DC bus voltage, the reference waveform is fed through a 2-level PWM generator. This method incorporates the desired DC voltage level and unity power factor, i.e., I_q equals zero, in its pulse width modulation imposed to the active rectifier's switches. When applied together with the excitation system controller, as explained in the previous paragraph, the hydropower generator system should theoretically be able to also address the microgrid's power flow as a secondary control, although the potential effect of the excitation control system is very limited compared to implementing a AGC system. Nevertheless, the battery system is, in this mode of operation, mainly in charge of the load saturation. Figure 3-14 shows the VSR controller as it is implemented in the simulation model.

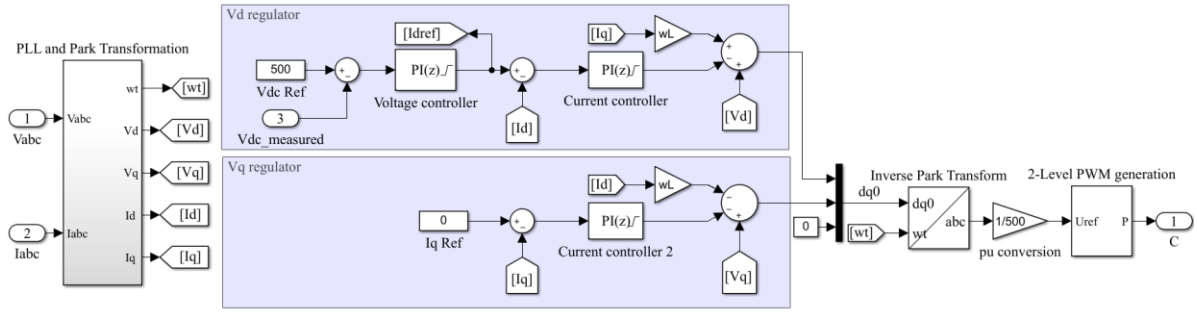

Figure 3-14 VSR controller of the active rectifier model as implemented in the hydro-generator system.

The logical principle of the VSR controller is shown in greater detail in the flowchart in Figure 3-15. This flowchart is useful for determining the information flow of the system.

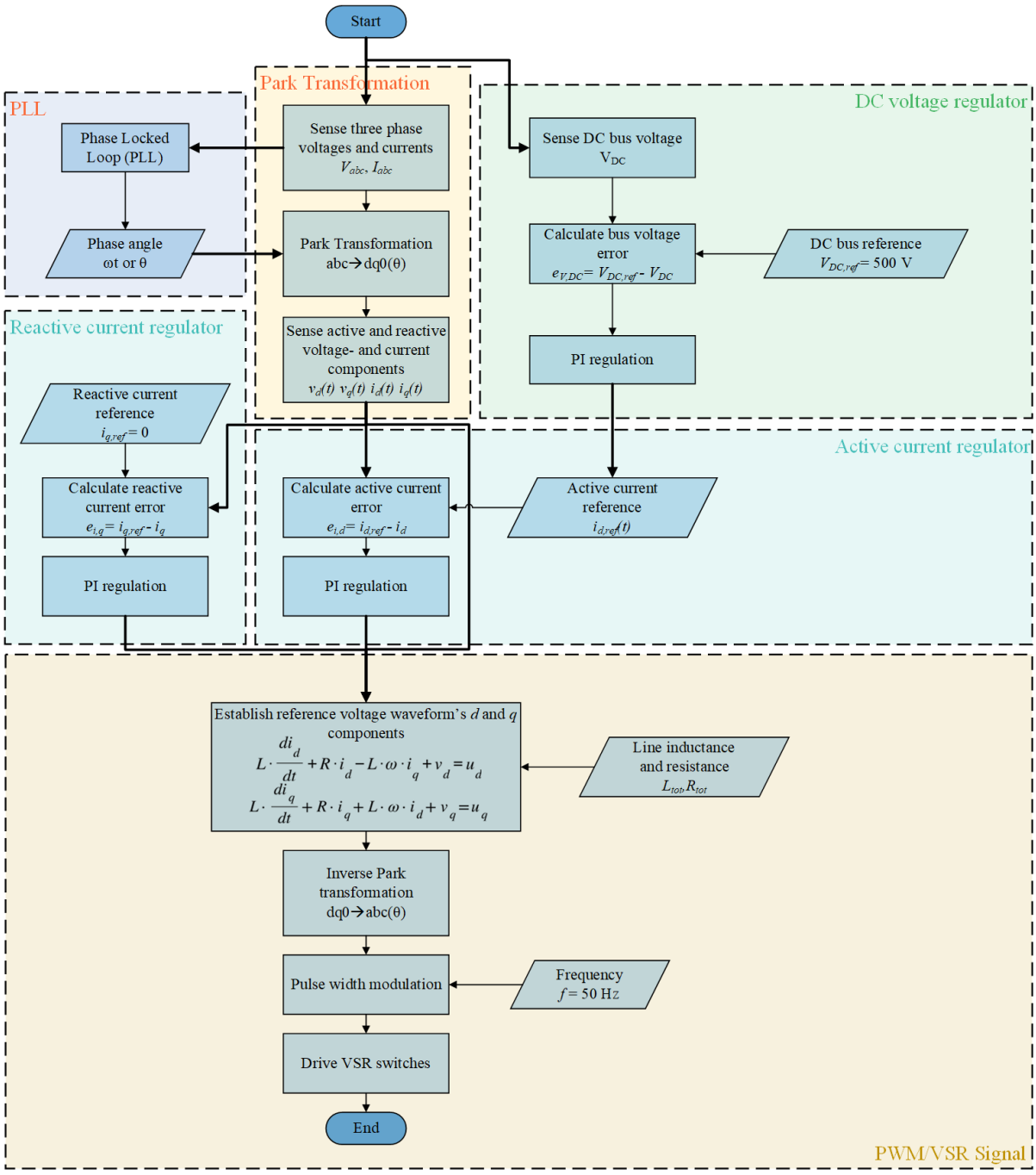

Figure 3-15 VSR controller principle portrayed as a flowchart.

3.2.5 Load Demand

In order to attain the NWA concept and realise the benefits of utilising a DC bus in the microgrid application, the systems load demand is enforced directly to the DC bus. It takes the form of a DC machine load, as opposed to a resistive load, to better represent the nature of a load one could expect to encounter in chemical industry. Furthermore, there are also grounds to justify the connection of an EV with the microgrid's load characterised as a DC machine, which is highly likely on a manufacturing site. This is integrated into the microgrid model through the use of a Simulink function block called One-Quadrant Chopper DC Drive [56]. By setting speed as the defined mechanical input of the block, the

load pattern can easily be fed to the DC machine through a signal generator, like the irradiance levels in the PV system. The relevant parameter settings for the DC machine are shown in Table 3-10.

Table 3-10 Simulation model's DC machine load characteristics.

Parameter	Symbol	Value	Unit
Nominal voltage	V	*500.00*	[V]
Nominal power	P	*52 220.00*	[W]
Acceleration/Deceleration	a	*±500.00*	[rpm/s]
Speed Controller			
Proportional gain	P_v	*400.00*	-
Integral gain	I_v	*1000.00*	-
Current Controller			
Proportional gain	P_{IL}	*20.00*	-
Integral gain	I_{IL}	*200.00*	-
Sampling time	T_{sl}	*10.00*	[µs]

For the sake of the topic of this thesis, which primarily encompasses the component- and control system application of the microgrid proposition at hand, the load profile imposed in this simulation model is designed to test the systems' robustness. In the first load case, this inherently means that the load profile must emphasise the scenario where the introduction of the supercapacitor is essential to maintain the bus voltage criteria. Additionally, the load profile should also "force" the battery- and supercapacitor systems into both injection- and extraction mode to accentuate the validity of the results. Encapsulating these requirements, the selected load profile is the one shown in Figure 3-16. Based on what already can be anticipated from the PV system and its irradiation profile, the load profile in this model facilitates both scenarios of surpluses and deficits to the power balance.

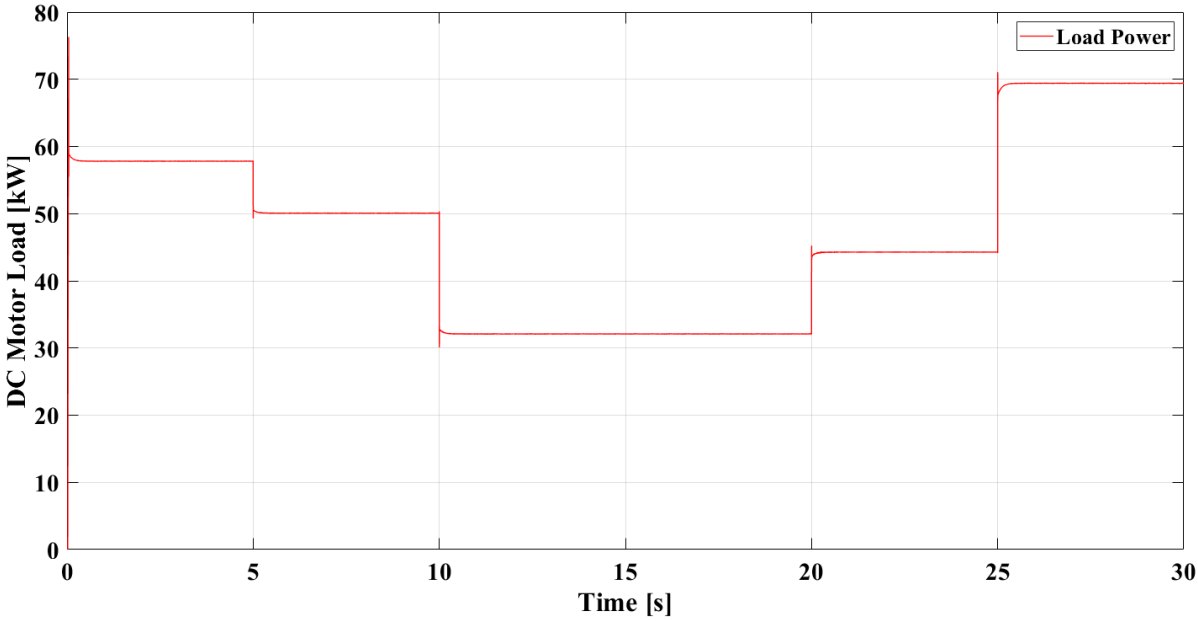

Figure 3-16 Load sequence of the load system

4 Results

This chapter portrays the simulation results of the proposed microgrid solution. The results are regarding the load sharing schemes across each mode of operation during both load cases, the control system's ability to stabilize the DC bus and handling of operation point, as well as power electronic considerations such as filtering and component characteristics.

4.1 Simulation Synopsis

As mentioned earlier, three modes of operation are considered in the simulation model, whereas each mode of operation is simulated with the following premises:

- Each simulation lasts for 30 seconds.
- Each mode of operation undertakes the two aforementioned load cases.
- Each load case is simulated both with- and without the implementation of the supercapacitor, with the exception of mode of operation 3.

The results presented in this section are grouped based on the mode of operation said results depict. Furthermore, each mode-of-operation section is mainly divided into the following three subsections:

- Power shares.
- Control system.
- Power electronics.

Both load cases are presented chronologically in each subsection. The two load cases that the modes of operation are simulating are as follows:

- **Load case 1** undertakes the scenario where the load profile presented in Figure 3-16 is imposed on the microgrid by the DC machine load. The PV array is exposed to a solar irradiance over the same time period equal to the sequence shown in Figure 3-2.
- **Load case 2** represents the instance where no PV power is produced and the generator has a reduced production. At the same time, the load is constantly at its highest value in Figure 3-16, i.e., 69 kW.

4.2 Mode of Operation 1

Mode of operation 1 uses the HES system to regulate the DC bus voltage. The generator system constantly operates at nominal speed and a fixed field voltage, generating a constant power during the entire operation through a passive rectifier.

4.2.1 Power Shares

The simulated power shares to meet the load demand in the first load case, when the supercapacitor is not installed, are displayed in Figure 4-1. In the first 5 seconds, the load consumes 58 kW and steps down first to 50 kW and then to 32 kW during the next 15 seconds. In the last 10 seconds, the load demand increases to 44 kW and eventually to 69 kW. This load pattern is the same for every simulation undertaking load case 1. Since the power produced by the PV array is non-dispatchable and the generator power is constant, the battery system compensates for surplus or absent power in the system. Consequently, the battery system is only discharging in the last 5 seconds of the simulation. The highest charging power is 109 kW, and its highest discharging power is 26 kW.

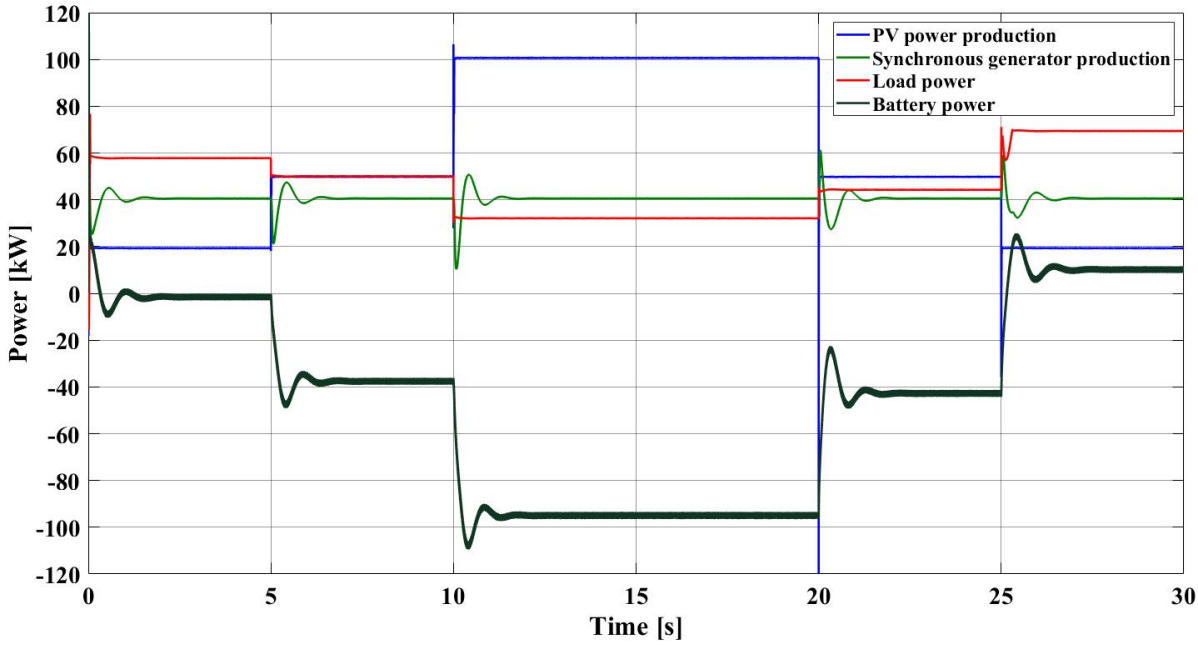

Figure 4-1 The power shares to meet the load demand in mode of operation 1's load case 1 without the supercapacitor.

The simulated power shares to meet the load demand in the first load case, with the supercapacitor installed, are shown in Figure 4-2. The battery pack in this instance is charging with a maximum power of 99 kW and discharges with a maximum power of 37 kW. For the supercapacitor, the maximum charging is 67 kW, and its maximum discharging is 54 kW.

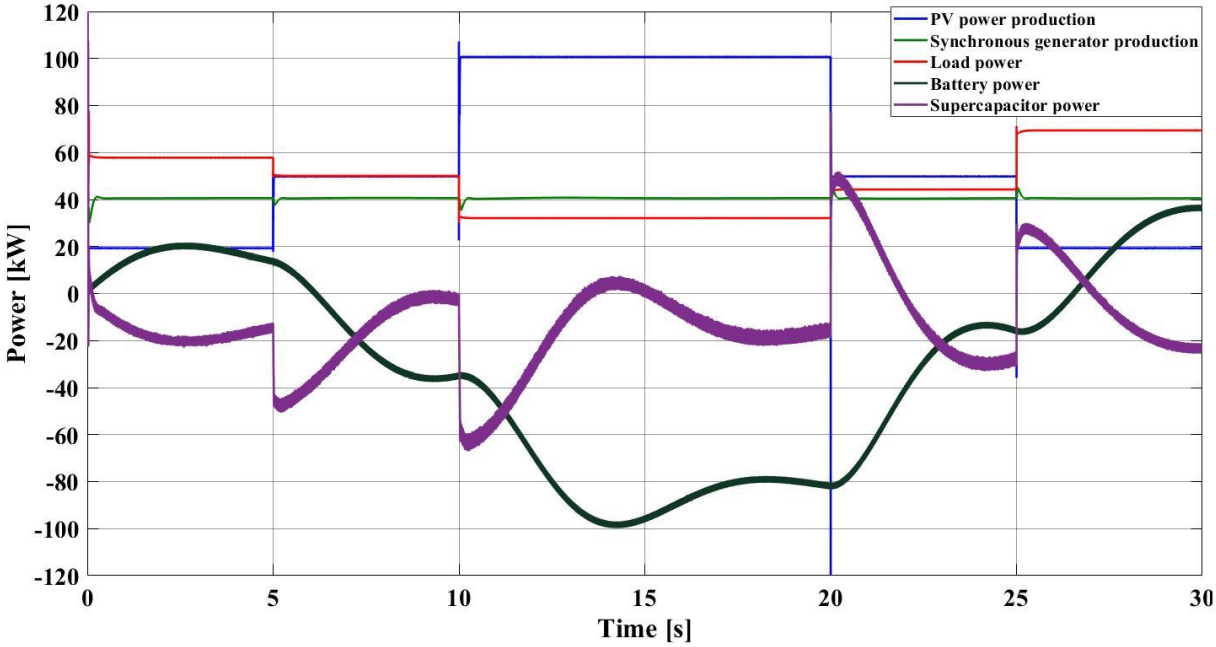

Figure 4-2 The power shares to meet the load demand in mode of operation 1's load case 1 with the supercapacitor.

The power shares to meet the load demand for the second load case, when the supercapacitor is not installed, is plotted in Figure 4-3. As the load is set to 69 kW constantly and the generator is only producing 25 kW, the battery system compensates by providing constant power of 44 kW to the system.

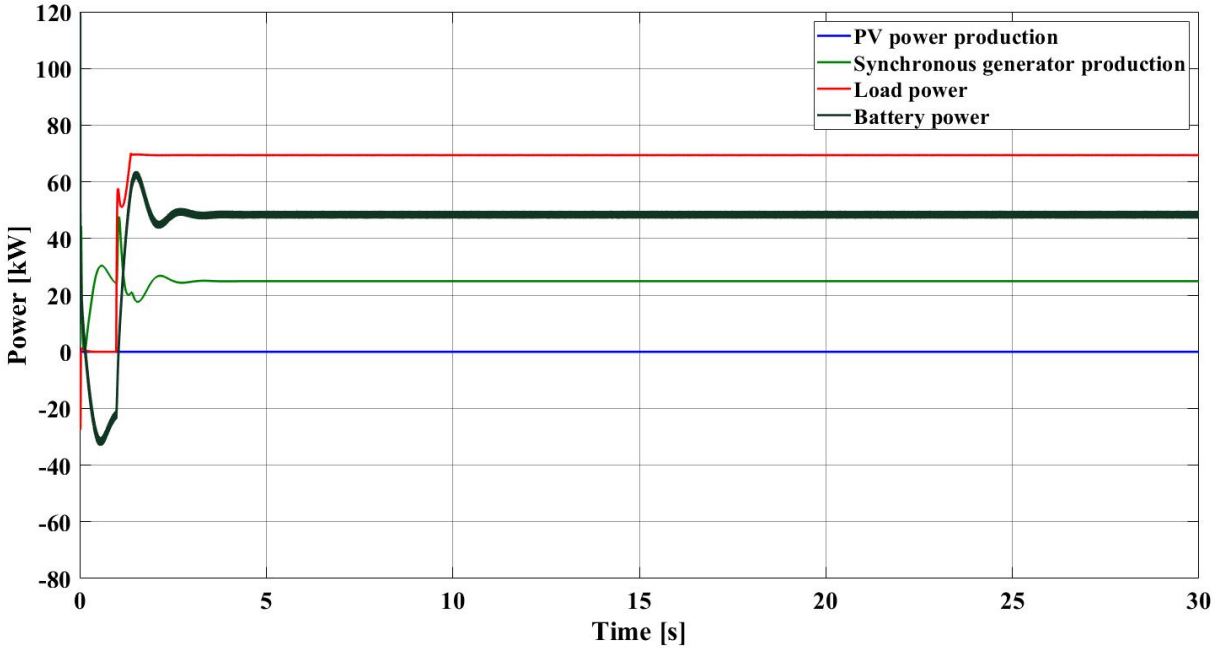

Figure 4-3 The power shares to meet the load demand in mode of operation 1's load case 2 without the supercapacitor.

The power shares to meet the load demand for the second load case, with the supercapacitor installed is shown in Figure 4-4. With the load- and generator production equal to the previous instance, the battery- and supercapacitor collaboration, namely the HES system, saturates the remaining load demand accordingly.

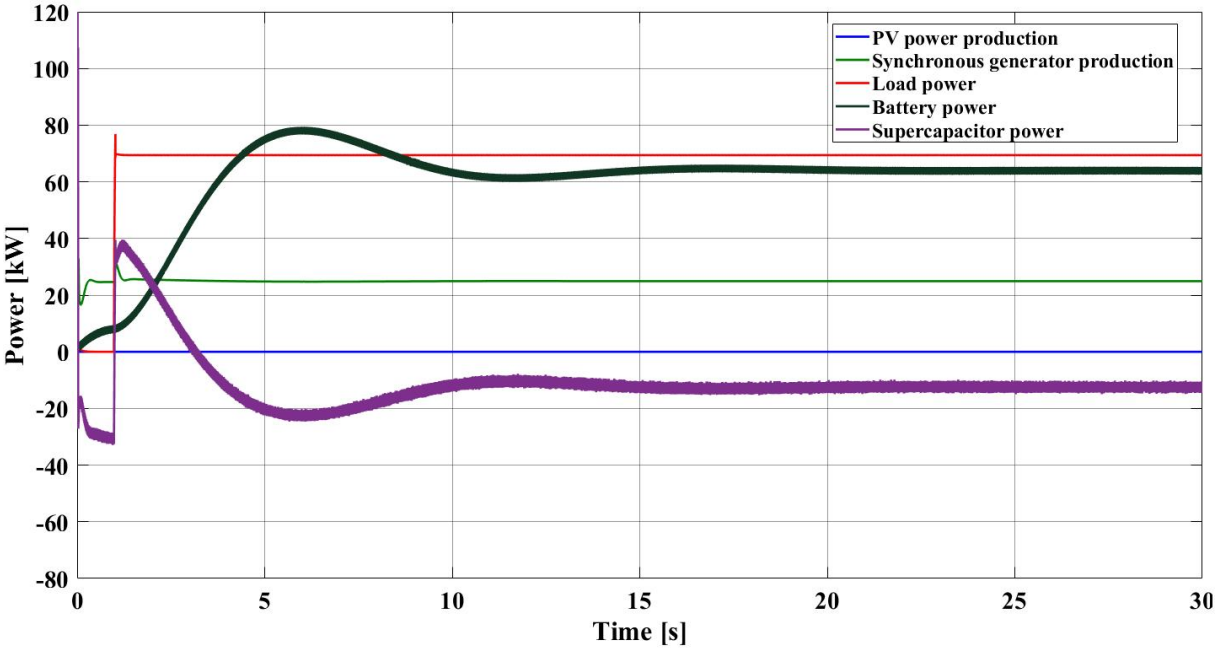

Figure 4-4 The power shares to meet the load demand in mode of operation 1's load case 2 with the supercapacitor.

4.2.2 Control System

Figure 4-5 shows the simulated DC bus voltage plotted together with its reference voltage of 500 V in load case 1 without the supercapacitor installed. The highest measured bus voltage deviations appear at the 10- and 20 seconds mark, where first, its 82 V above- and 93 V below the reference value.

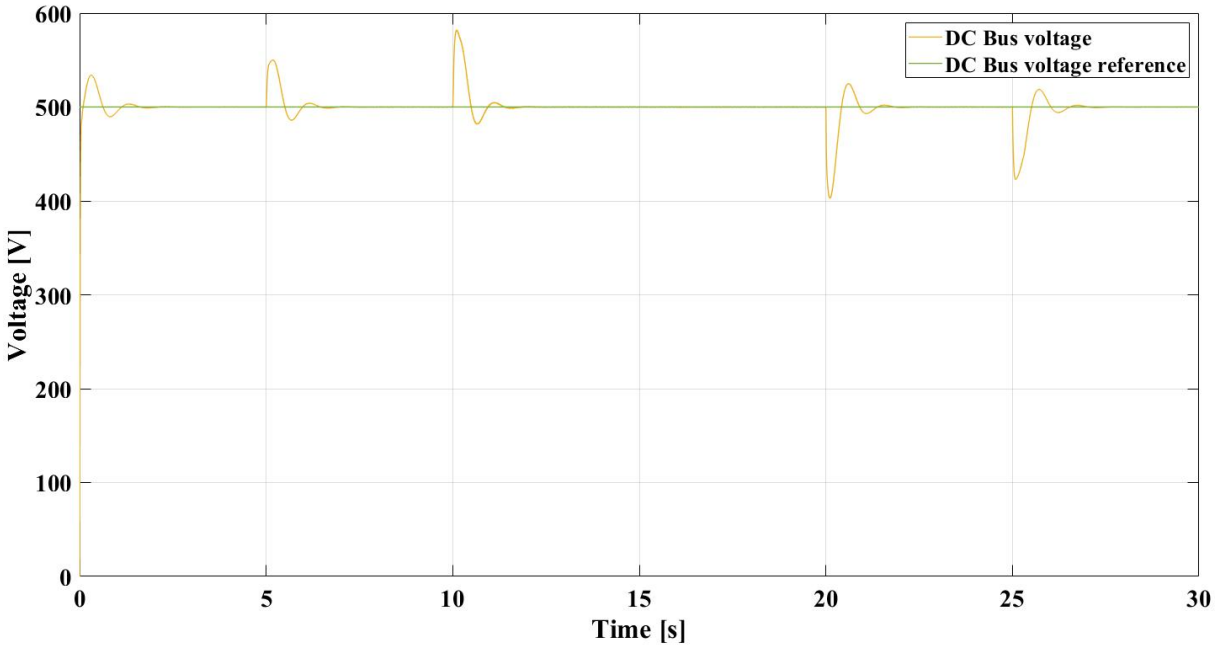

Figure 4-5 DC bus voltage with its reference voltage in mode of operation 1's load case 1 without the supercapacitor.

The DC bus voltage plotted together with its voltage reference of 500 V in load case 1 with the supercapacitor installed is shown in Figure 4-6.

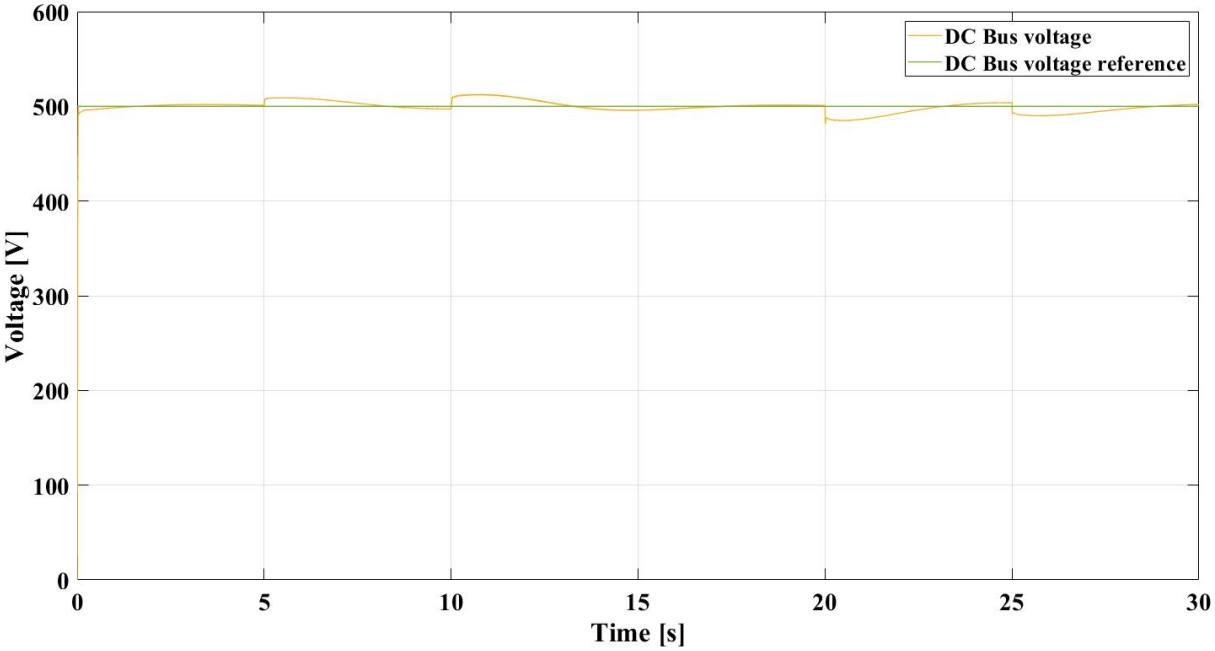

Figure 4-6 DC bus voltage with its reference voltage in mode of operation 1's load case 1 with the supercapacitor.

Figure 4-7 shows a closer look at the DC bus voltage from the previous figure compared to the battery- and supercapacitor voltage control signals. The bus voltage deviates by 13 V above the reference and 15 V below when the system implements the supercapacitor.

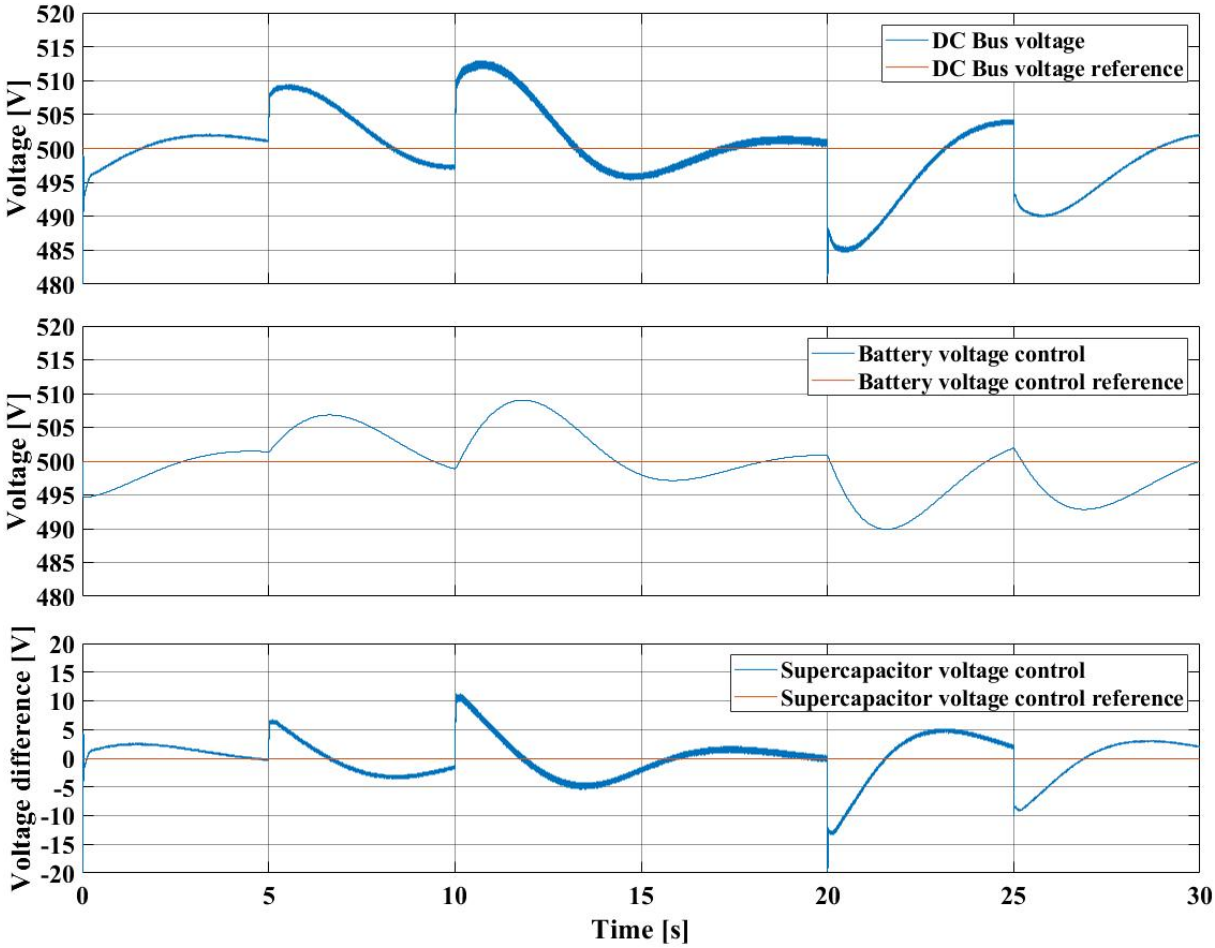

Figure 4-7 DC bus-, battery-, and supercapacitor voltage with the reference voltages in mode of operation 1's load case 1.

Figure 4-8 shows the DC bus voltage plotted together with its reference of 500 V in load case 2 without the supercapacitor installed. The largest voltage deviation is measured at 85 V.

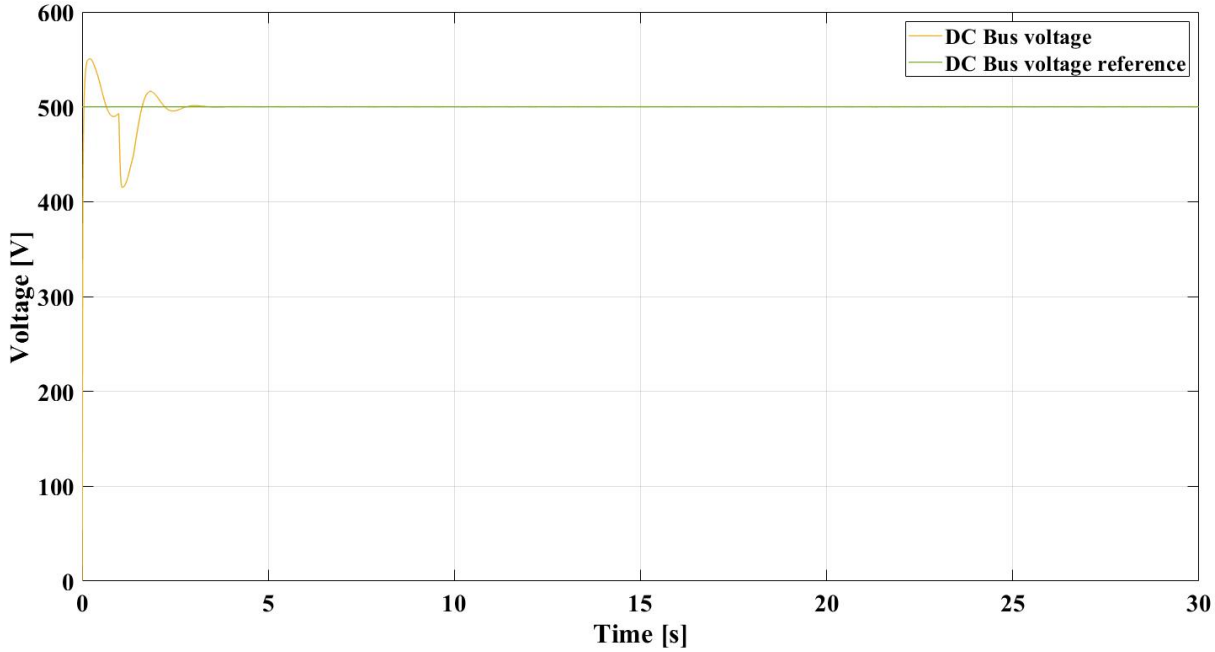

Figure 4-8 DC bus voltage with its reference DC bus voltage in mode of operation 1's load case 2 without the supercapacitor.

The DC bus voltage plotted with its reference of 500 V in load case 2 when the supercapacitor is installed is shown in Figure 4-9.

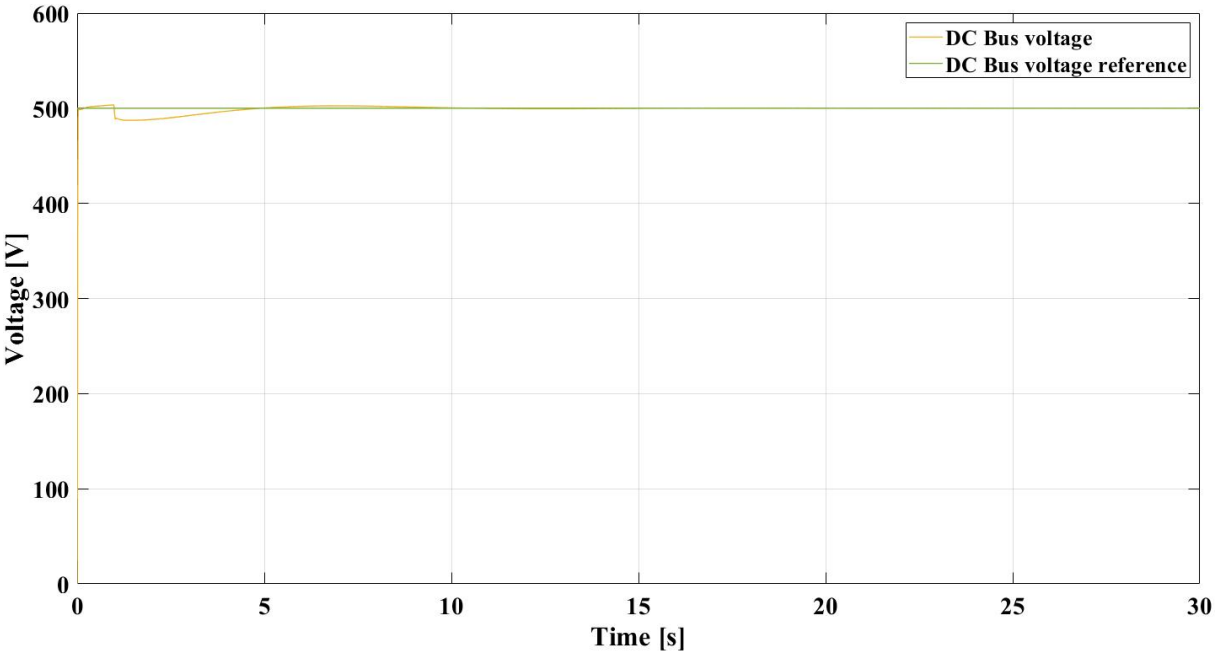

Figure 4-9 DC bus voltage with its reference DC bus voltage in mode of operation 1's load case 2 with the supercapacitor.

Figure 4-10 shows a closer look at the DC bus voltage from the previous graph compared to the battery- and supercapacitor voltage control signals. The bus voltage deviates by 4 V above the reference and 13 V below when the supercapacitor is installed.

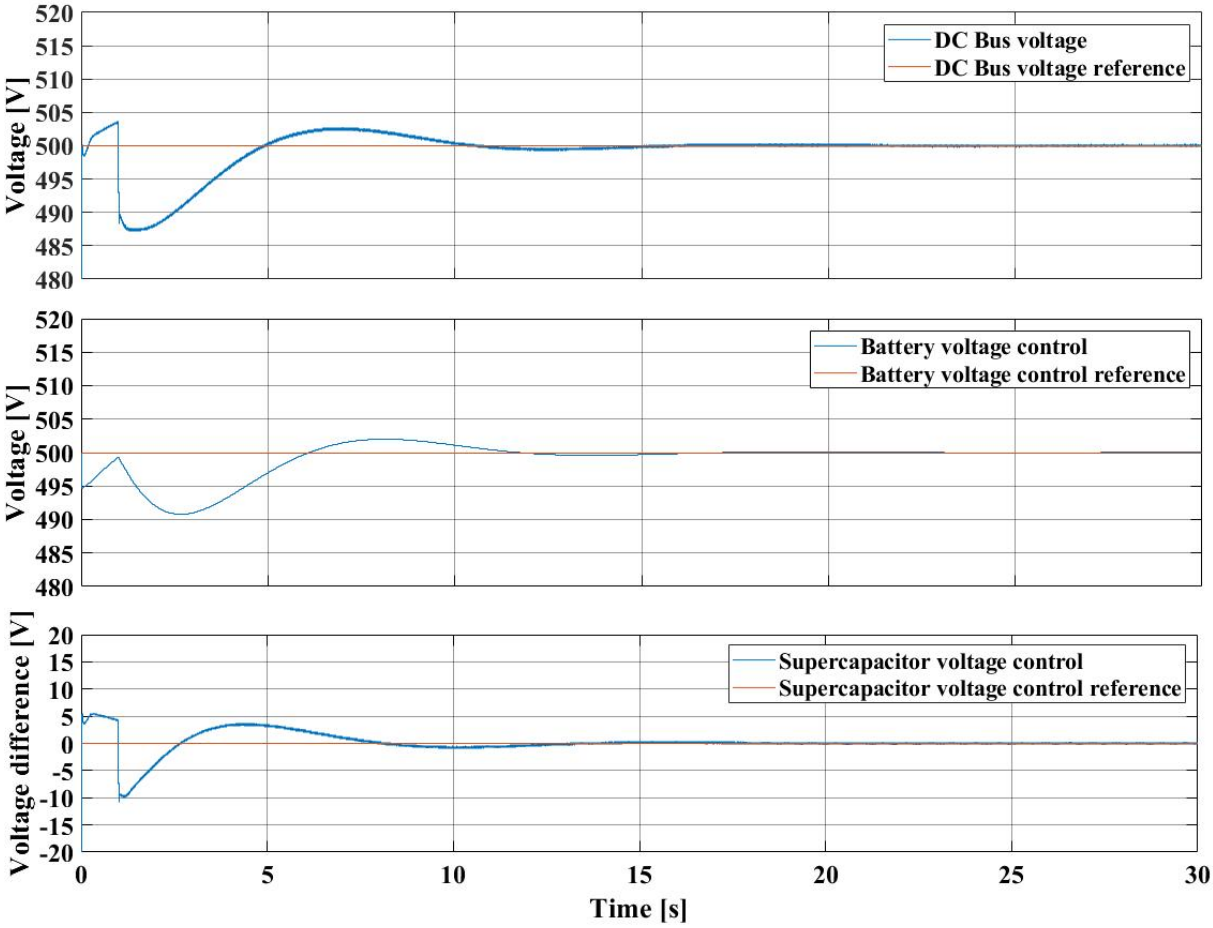

Figure 4-10 DC bus-, battery-, and supercapacitor voltage with the reference voltage in mode of operation 1's load case 2.

4.2.3 Power Electronics

The simulated varying PV power production from the 100 kW rated PV array is shown in Figure 4-11, where the produced power varies from around 20 kW to 100 kW. The PV power profile is applied in every simulation of load case 1.

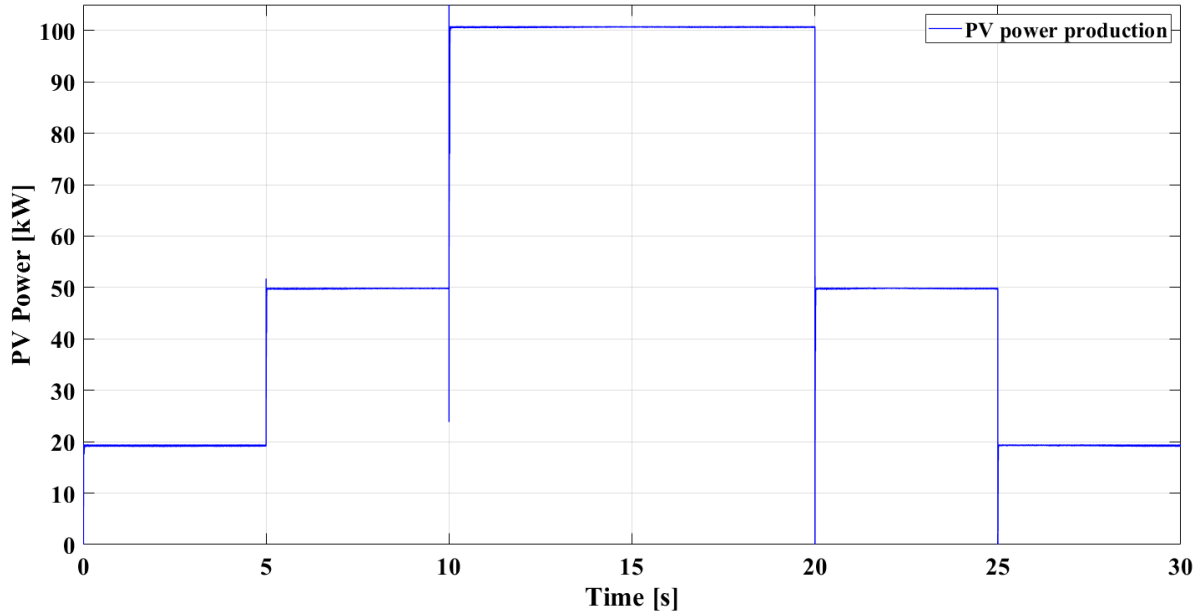

Figure 4-11 PV array power production sequence for every mode of operation's load case 1.

The corresponding PV voltage and -current plotted together with irradiance sequence is shown in Figure 4-12. The graph shows the PV voltage varying approximately from 250 to 275 V and the PV current approximately from 75 to 370 A.

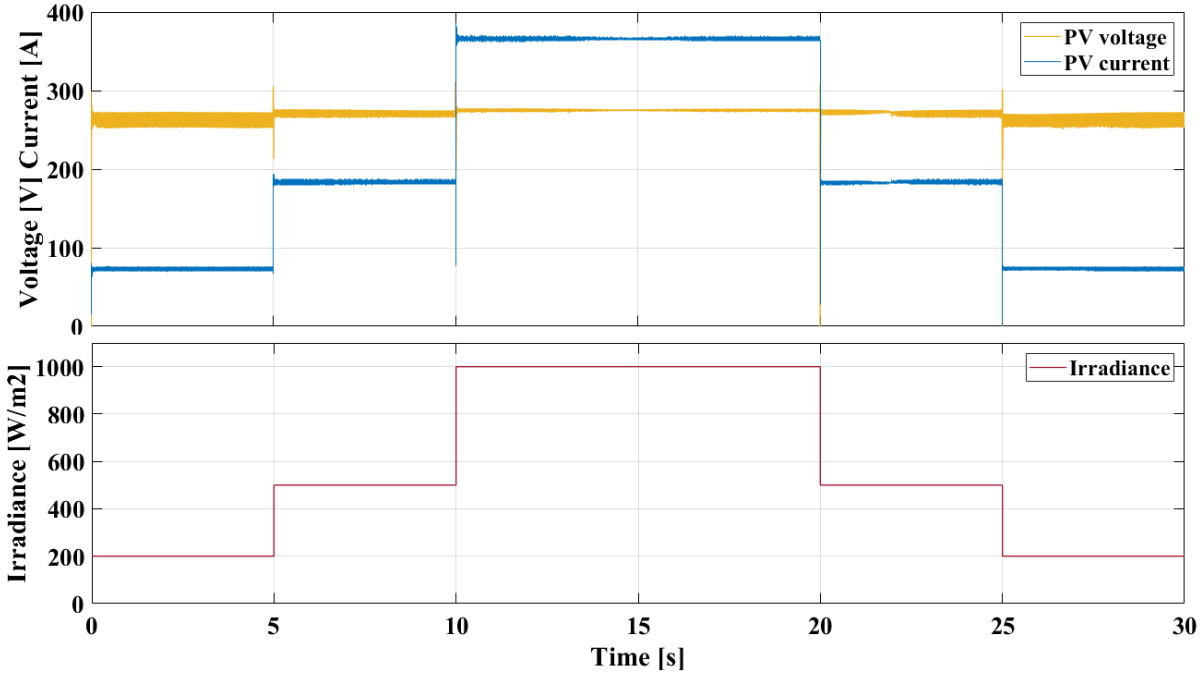

Figure 4-12 PV array voltage and -current every mode of operation's load case 1.

The battery output voltage, current, and state of charge in load case 1 without the supercapacitor installed are plotted in Figure 4-13. The battery voltage varies approximately from 258 to 266 V. The apex of the measured current is approximately -408 A when charging and 96 A when discharging. The state of charge plot indicates when the battery is charging or discharging by either an increase or decrease in the battery's SOC.

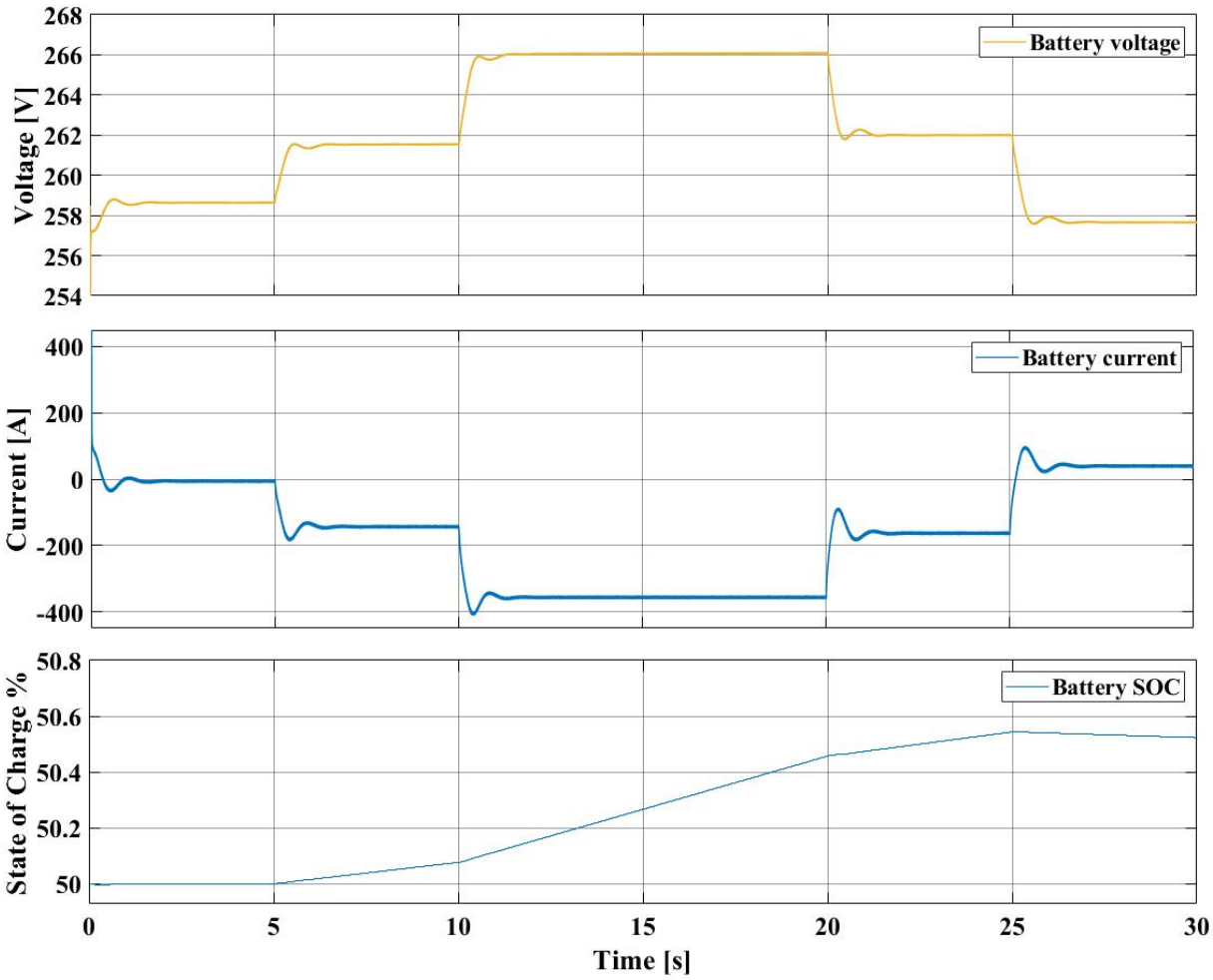

Figure 4-13 Bidirectional battery voltage, -current and SOC in mode of operation 1's load case 1 without the supercapacitor.

The battery output voltage, current, and SOC in load case 1 with the supercapacitor installed are plotted in Figure 4-14. The battery voltage varies from approximately 255 to 266 V, and the largest measured current is approximately -370 A when charging and 150 A when discharging. The battery's state of charge shows its discharging during the first 6 seconds, then charging until 27 seconds into the simulation and discharging for the last 3 seconds.

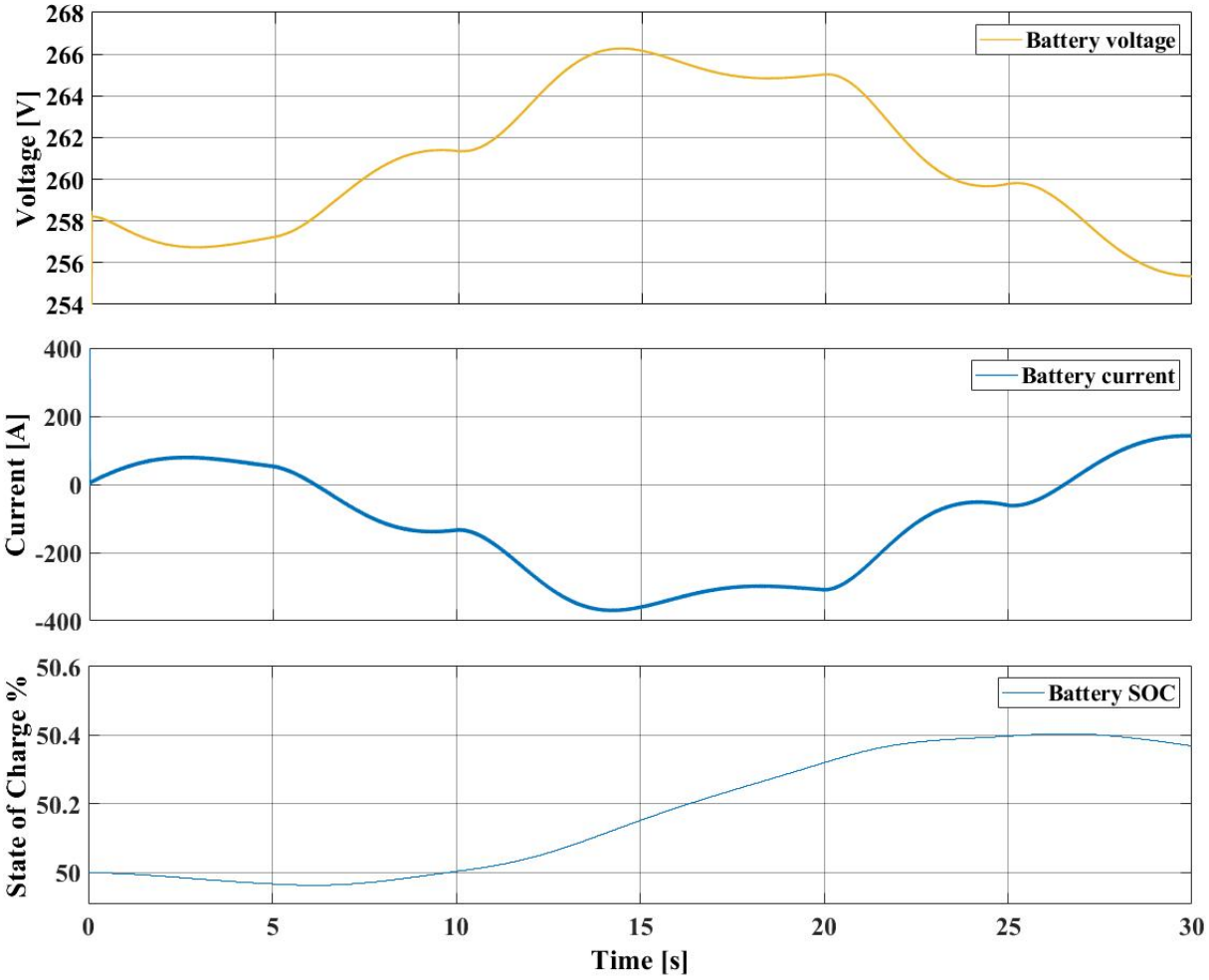

Figure 4-14 Bidirectional battery voltage, -current and SOC in mode of operation 1's load case 1 with the supercapacitor.

The supercapacitor output voltage, current, and SOC in load case 1 are plotted in Figure 4-15. The supercapacitor voltage varies approximately from 240 to 246 V, and the largest measured current is approximately 268 A while charging and 214 A during discharging. The state of charge shows that the supercapacitor is charging during the first 13 seconds, discharging from 13 to 15 seconds, charging from 15 to 20 seconds, discharging from 20 to 22 seconds, charging from 22 to 25 seconds, discharging from 25 to 27 seconds, and charging for the last 3 seconds of the simulation.

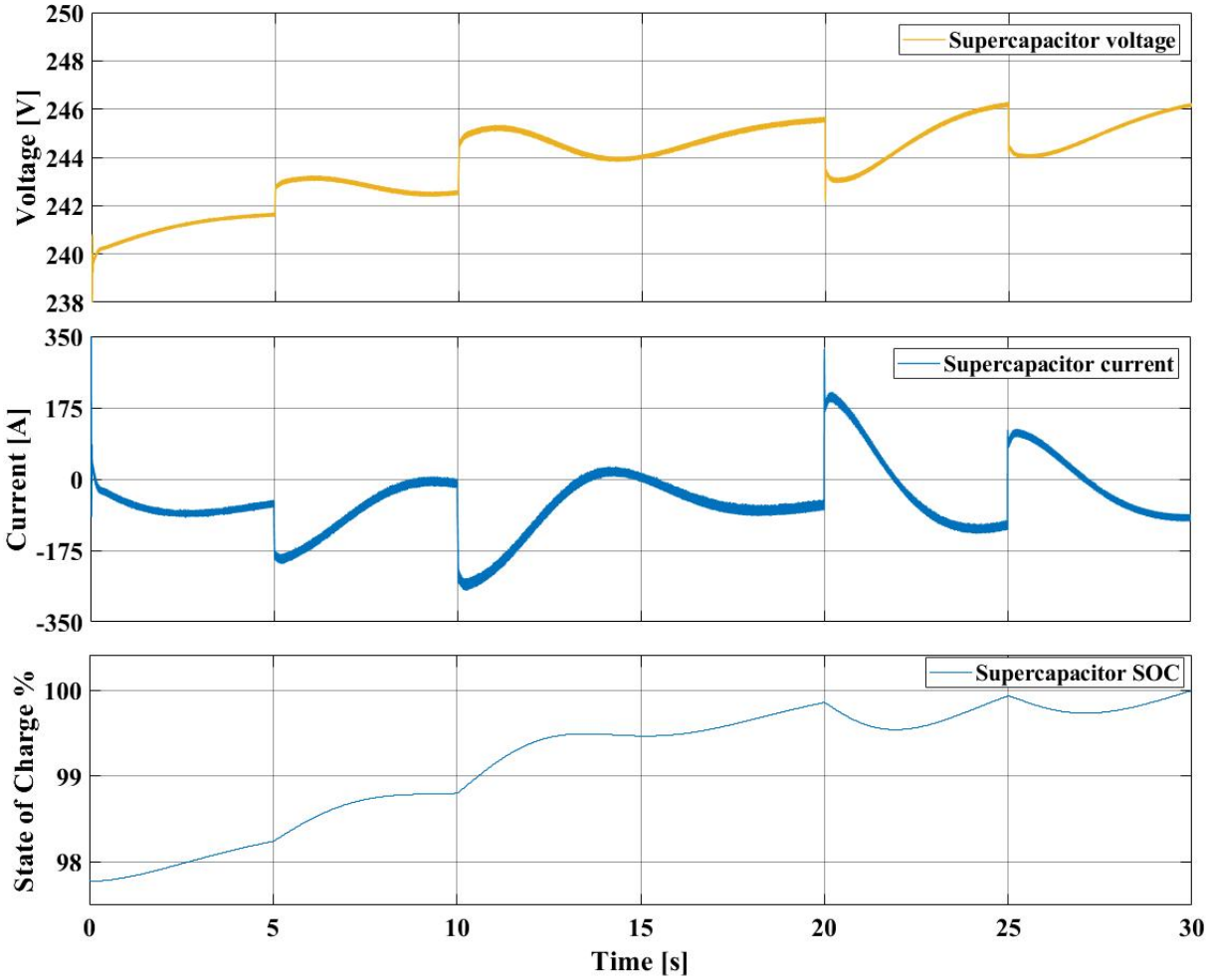

Figure 4-15 Bidirectional supercapacitor voltage, -current and SOC in mode of operation 1's load case 1.

The battery output voltage, current, and SOC in load case 2 without the supercapacitor installed are plotted in Figure 4-16. The battery voltage has a peak at approximately 260 V and reaches a steady-state at 254 V, while the current peaks at 250 A and reach a steady-state at approximately 190 A. The battery's state of charge shows a constant decrease after the load demand is stabilized.

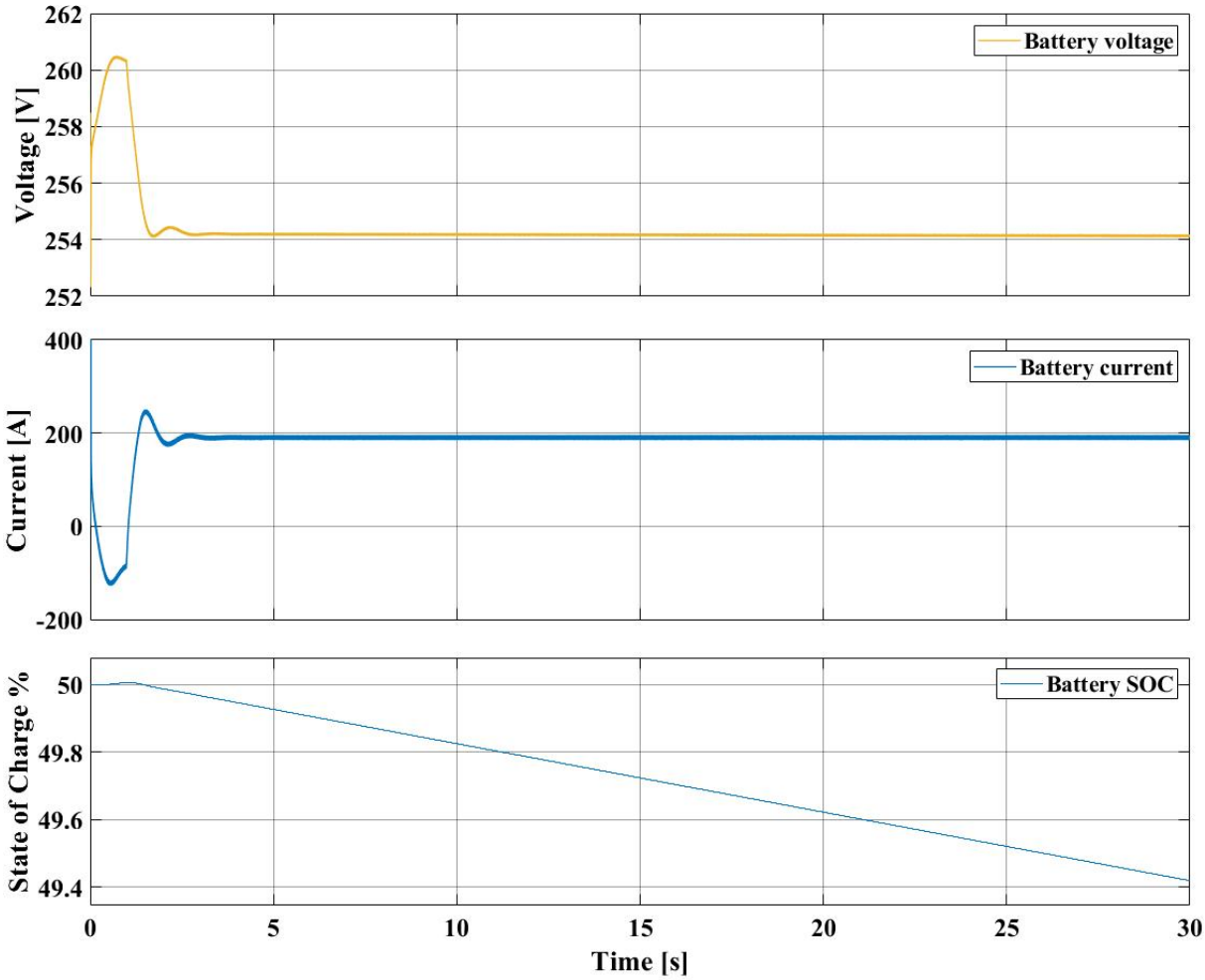

Figure 4-16 Bidirectional battery voltage, -current and SOC in mode of operation 1's load case 2 without the supercapacitor.

The battery output voltage, current, and SOC in load case 2 with the supercapacitor installed are plotted in Figure 4-17. The battery voltage is at its largest at approximately 258 V and reaches steady-state a little below 253 V, while the current has a peak at approximately 316 A and reaches steady-state at approximately 250 A. The battery's state of charge shows a constant decrease after the system enters steady-state.

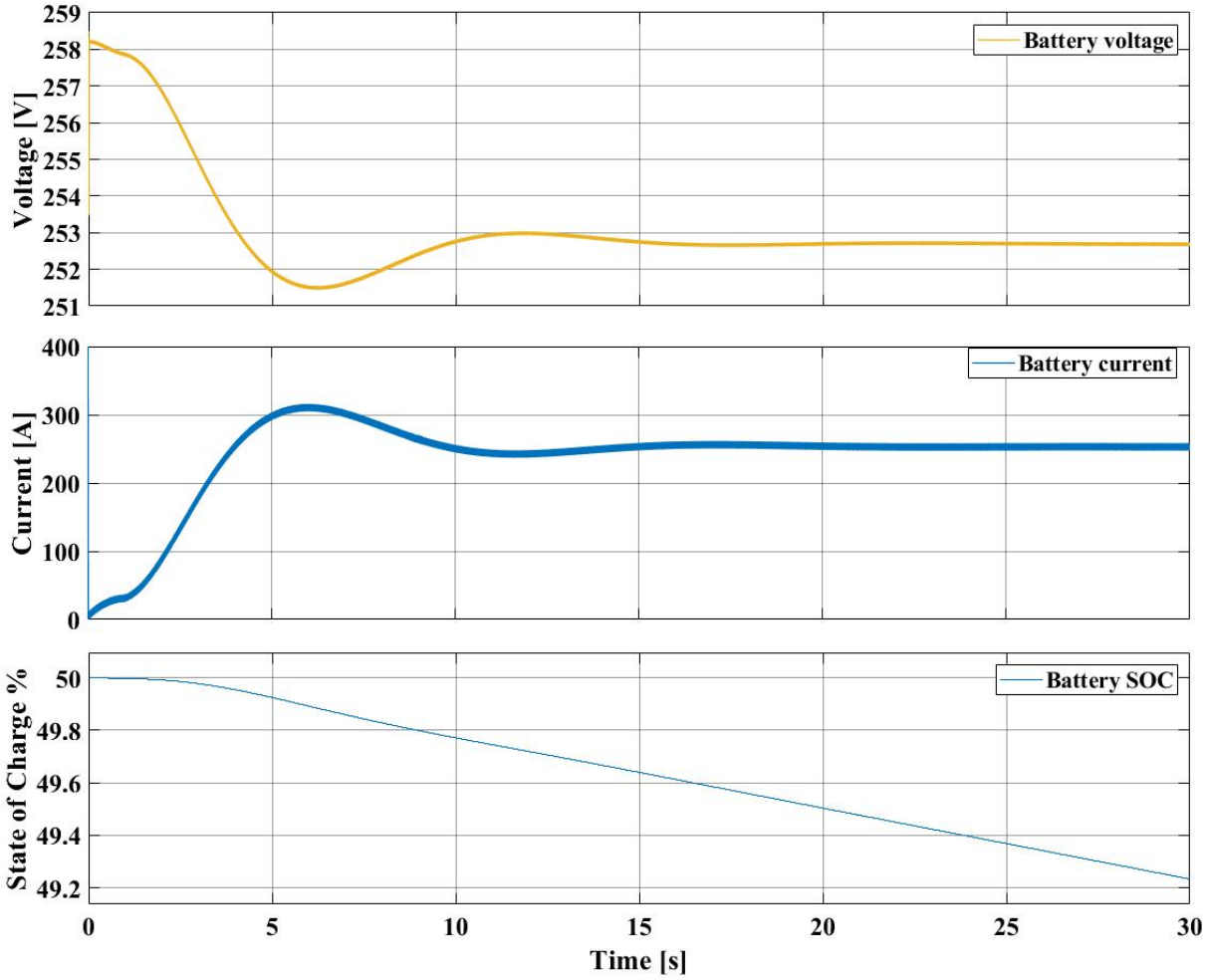

Figure 4-17 Bidirectional battery voltage, -current and SOC in mode of operation 1's load case 2 with the supercapacitor.

The supercapacitor output voltage, current, and SOC in load case 2 are plotted in Figure 4-18. The supercapacitors voltage varies approximately from 239 to 245 V. The largest measured current is slightly below -100 A while charging and approximately 170 A during discharging. Steady-state is reached at approximately -50 A. The supercapacitor state of charge shows a constant increase after the load has stabilized.

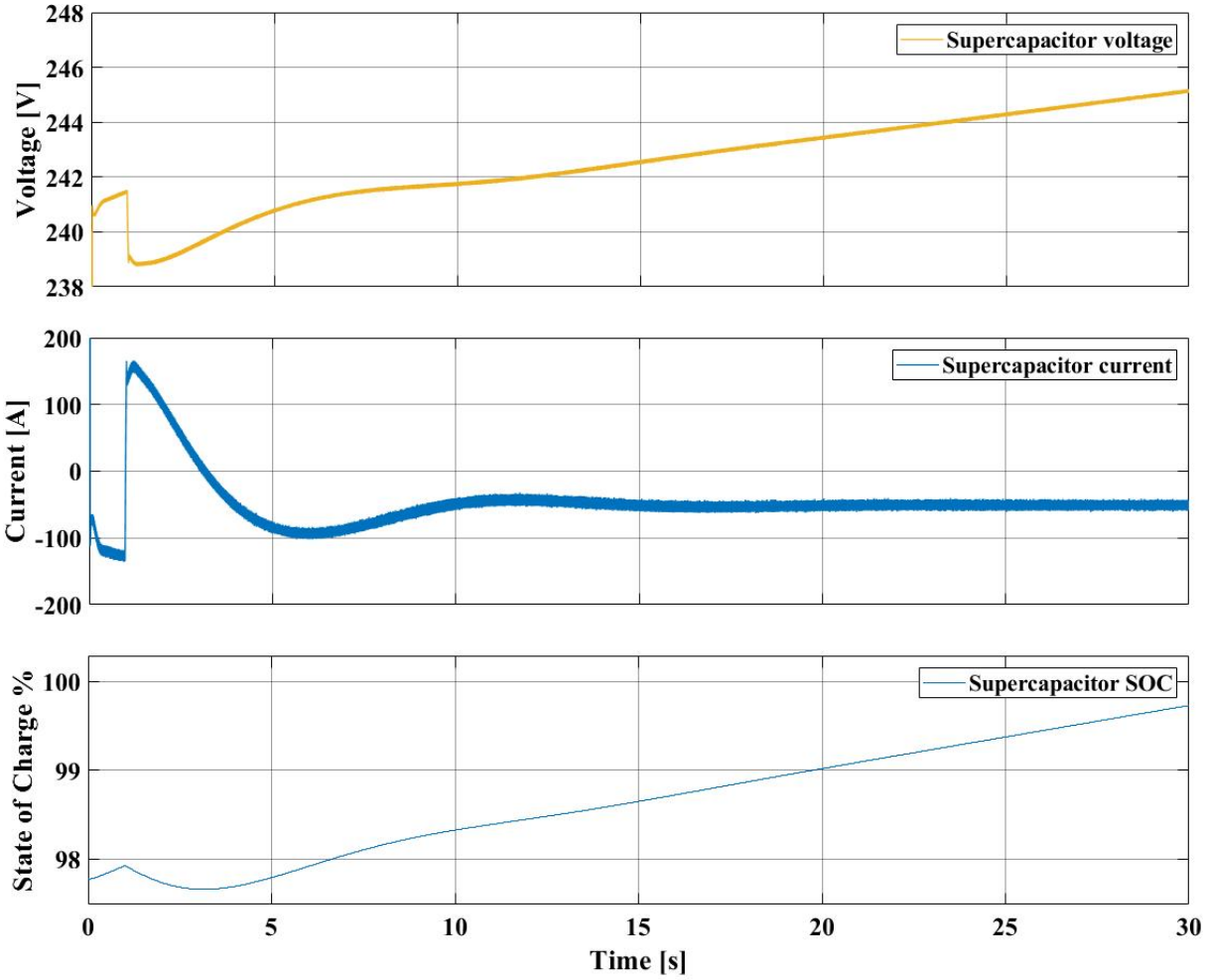

Figure 4-18 Bidirectional supercapacitor voltage, -current and SOC in mode of operation 1's load case 2.

4.3 Mode of Operation 2

Mode of operation 2 uses the generator with an excitation-controlled field voltage based on the generator's terminal voltage. Essentially, this mode also uses the HES system to regulate the DC bus voltage. Also, this mode uses a passive rectifier for the generator system.

4.3.1 Power Shares

The simulated power shares to meet the load demand in load case 1 without the supercapacitor installed are displayed in Figure 4-19. Since the power produced by the PV array is non-dispatchable, the generator and the battery system compensate for surplus or absent power in the system. The battery pack is charging with a maximum power of 95 kW and discharging with a maximum power of 12 kW. The generator delivers 40 kW at steady-state.

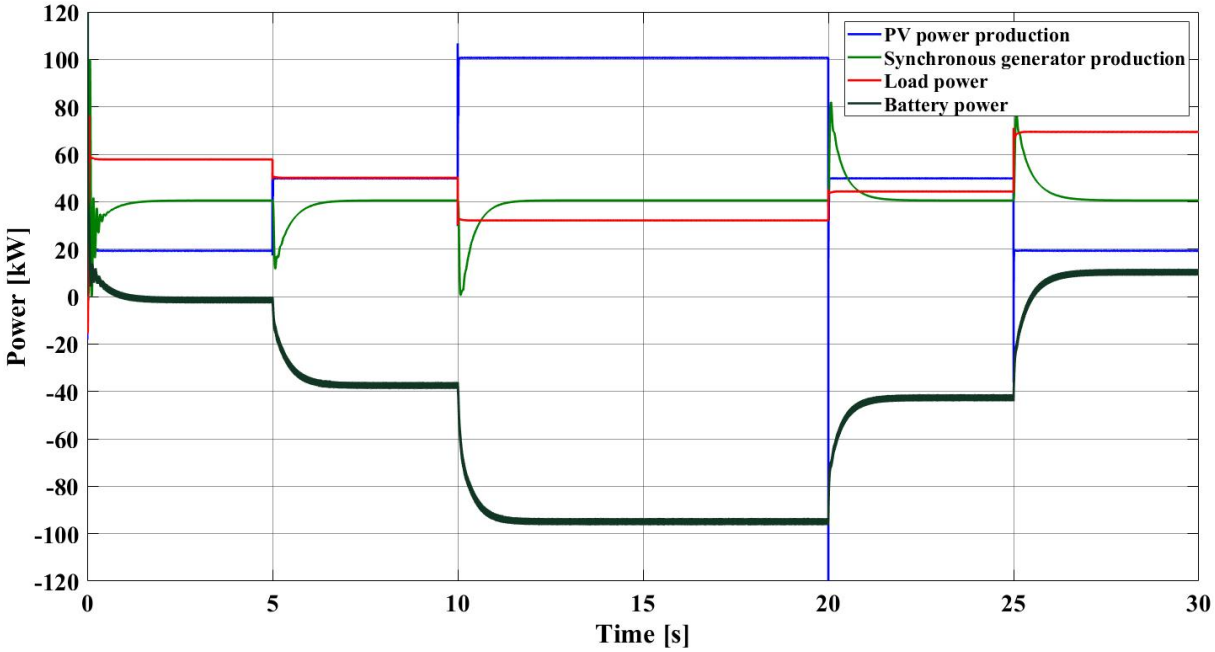

Figure 4-19 The power shares to meet the load demand in mode of operation 2's load case 1 without the supercapacitor.

The simulated power shares to meet the load demand in load case 1 with the supercapacitor installed are shown in Figure 4-20. In this situation, the generator-, supercapacitor-, and battery systems compensate for any surplus or absent power in the system. The generator's power production varies from 31 to 50 kW, although it settles to 40 kW in steady-state. The battery pack is charging with a maximum power of 95 kW and discharging with a maximum power of 34 kW. For the supercapacitor, the maximum charging is 64 kW, and its maximum discharging is 40 kW.

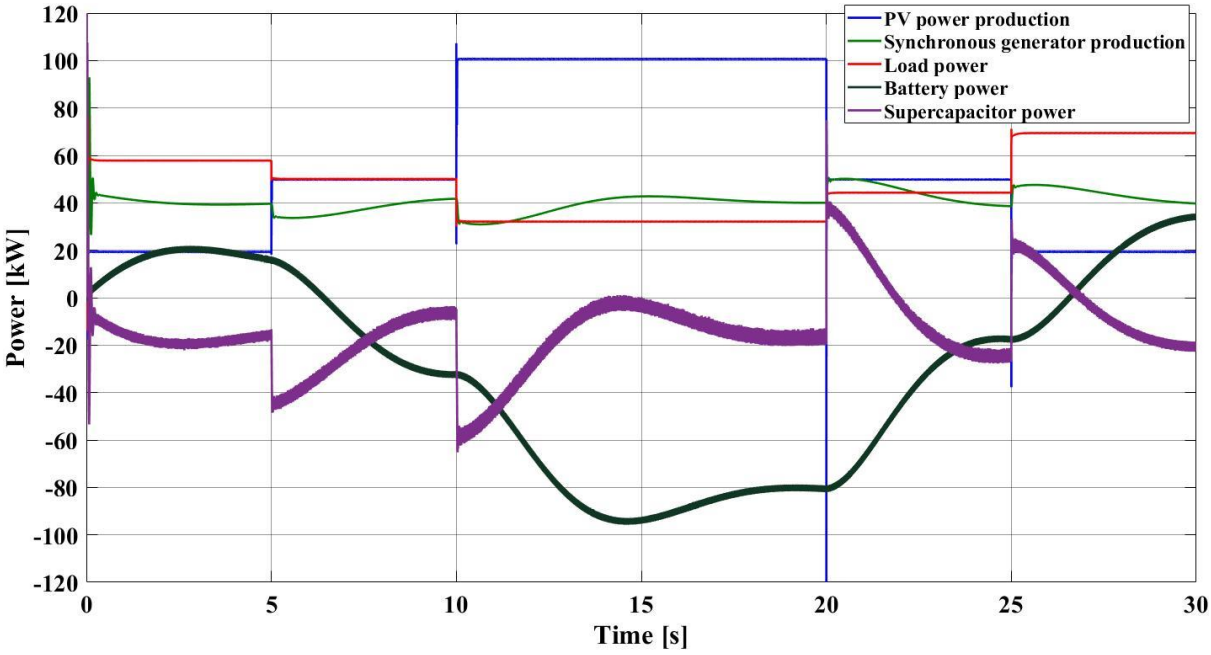

Figure 4-20 The power shares to meet the load demand in mode of operation 2's load case 1 with the supercapacitor.

The power shares to meet the load demand in load case 2 without the supercapacitor installed is plotted in Figure 4-21. As the load demand is set to 69 kW constantly throughout the simulation, the generator, along with the battery system, are compensating for the required load. The generator provides 25 kW, and the battery system provides 44 kW to the system in steady-state.

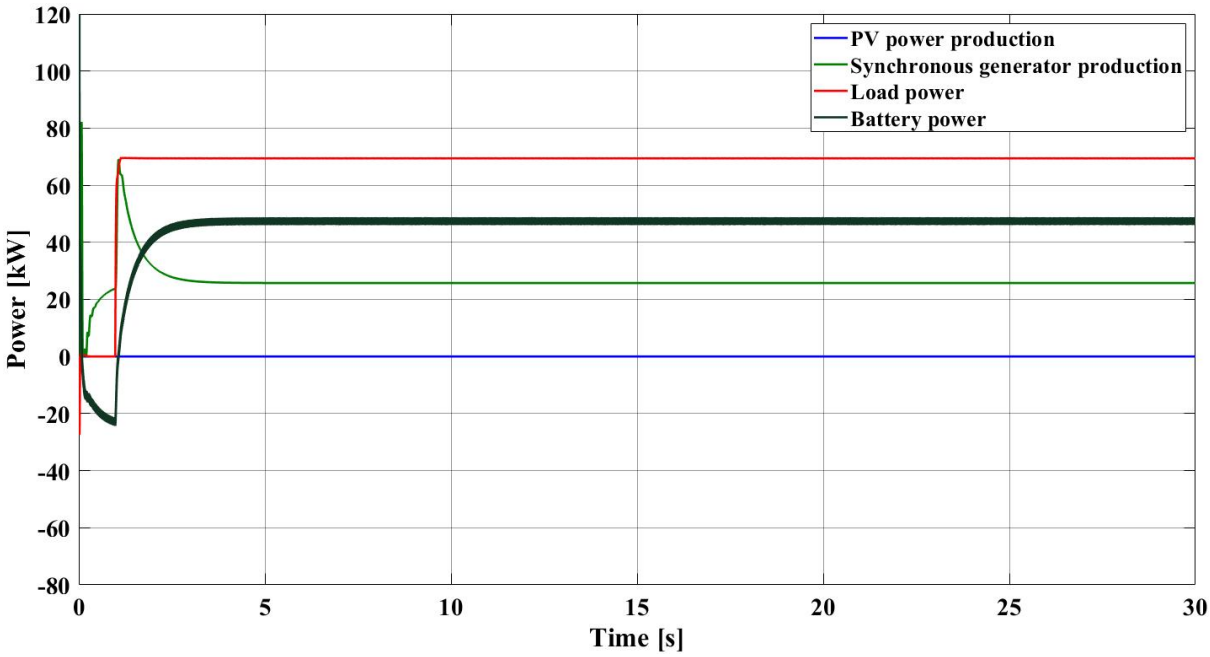

Figure 4-21 The power shares to meet the load demand in mode of operation 2's load case 2 without the supercapacitor.

The power shares to meet the load demand in load case 2 with the supercapacitor installed is shown in Figure 4-22. As the load demand is constantly consuming 69 kW and the generator is constantly producing 40 kW in steady-state, the battery- and supercapacitor systems provide the remaining power.

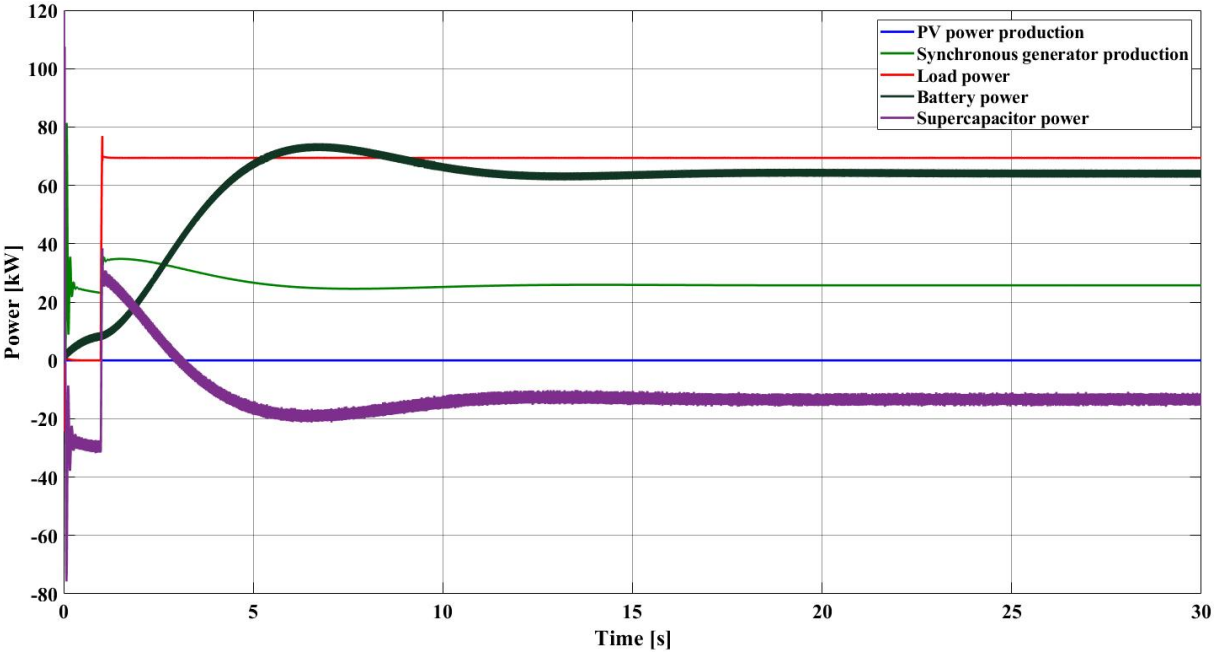

Figure 4-22 The power shares to meet the load demand in mode of operation 2's load case 2 with the supercapacitor.

4.3.2 Control System

Figure 4-23 shows the simulated DC bus voltage in load case 1 without the supercapacitor installed, plotted together with its reference voltage of 500 V. The highest measured bus voltage deviations, occurring at the 10- and 20 seconds mark, were at 69 V above and 70 V below the reference value, respectively.

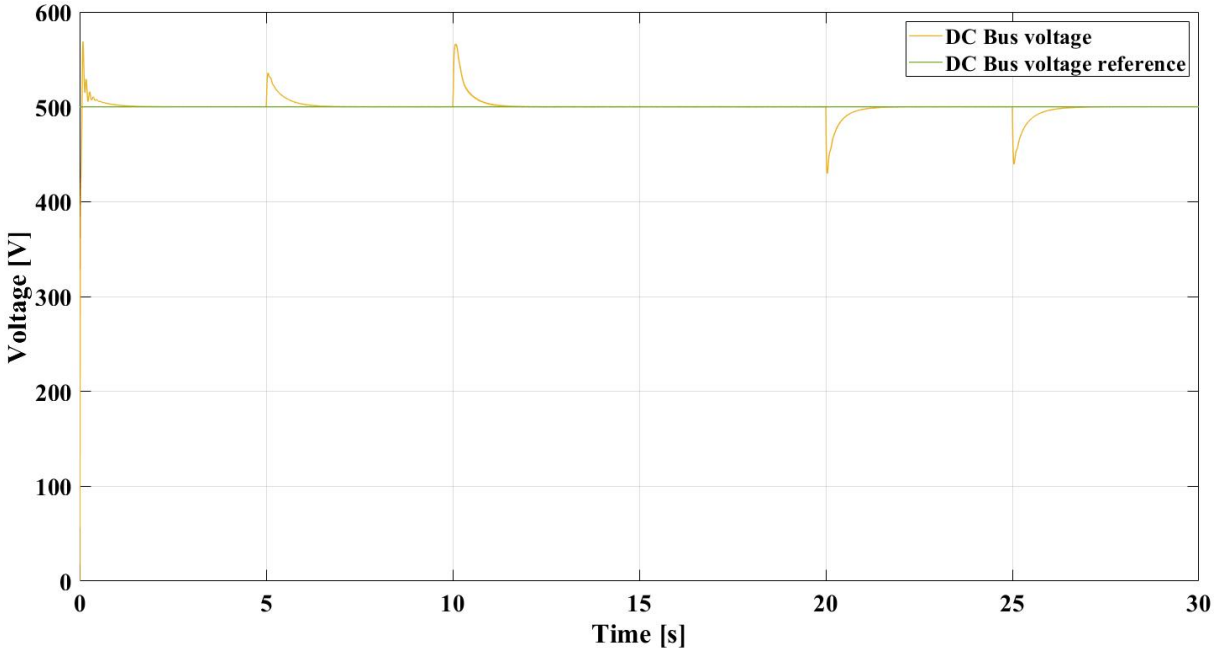

Figure 4-23 DC bus voltage with its reference voltage in mode of operation 2's load case 1 without the supercapacitor.

The DC bus voltage plotted together with its voltage reference of 500 V in load case 1 with the supercapacitor installed is shown in Figure 4-24.

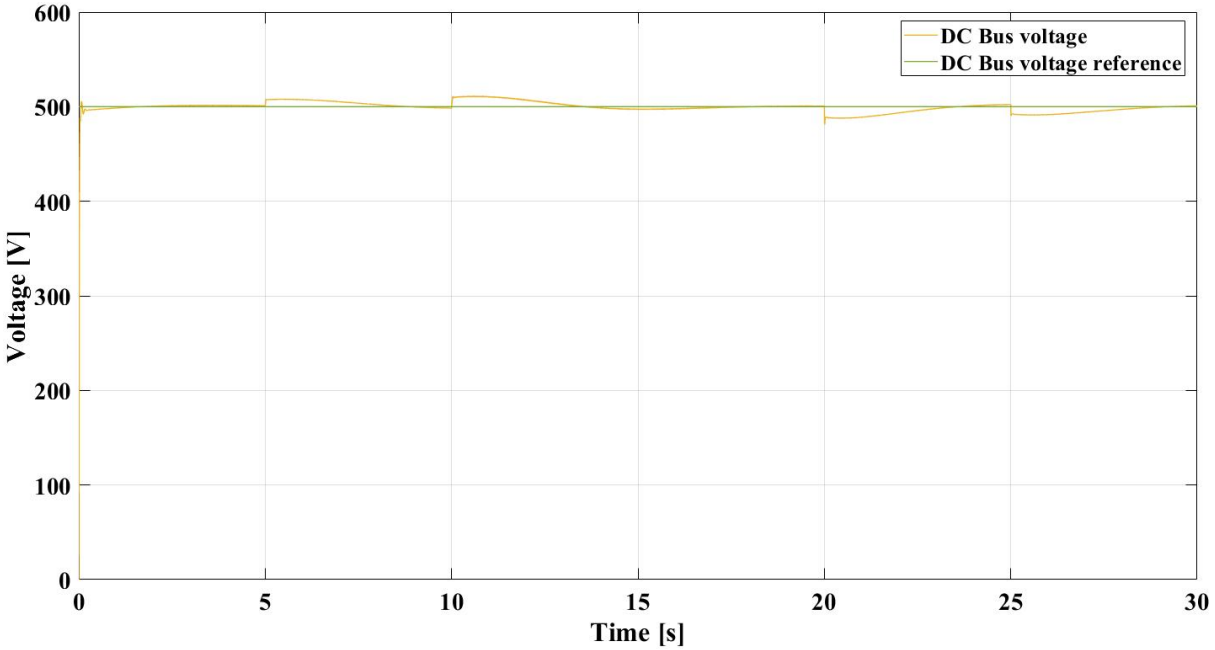

Figure 4-24 DC bus voltage with its reference voltage in mode of operation 2's load case 1 with the supercapacitor.

A closer look at the DC bus voltage in load case 1 with the supercapacitor installed, portrayed together with the battery and the supercapacitor voltage control signals, are shown in Figure 4-25. The bus voltage deviates by 11 V above the reference and 12 V below.

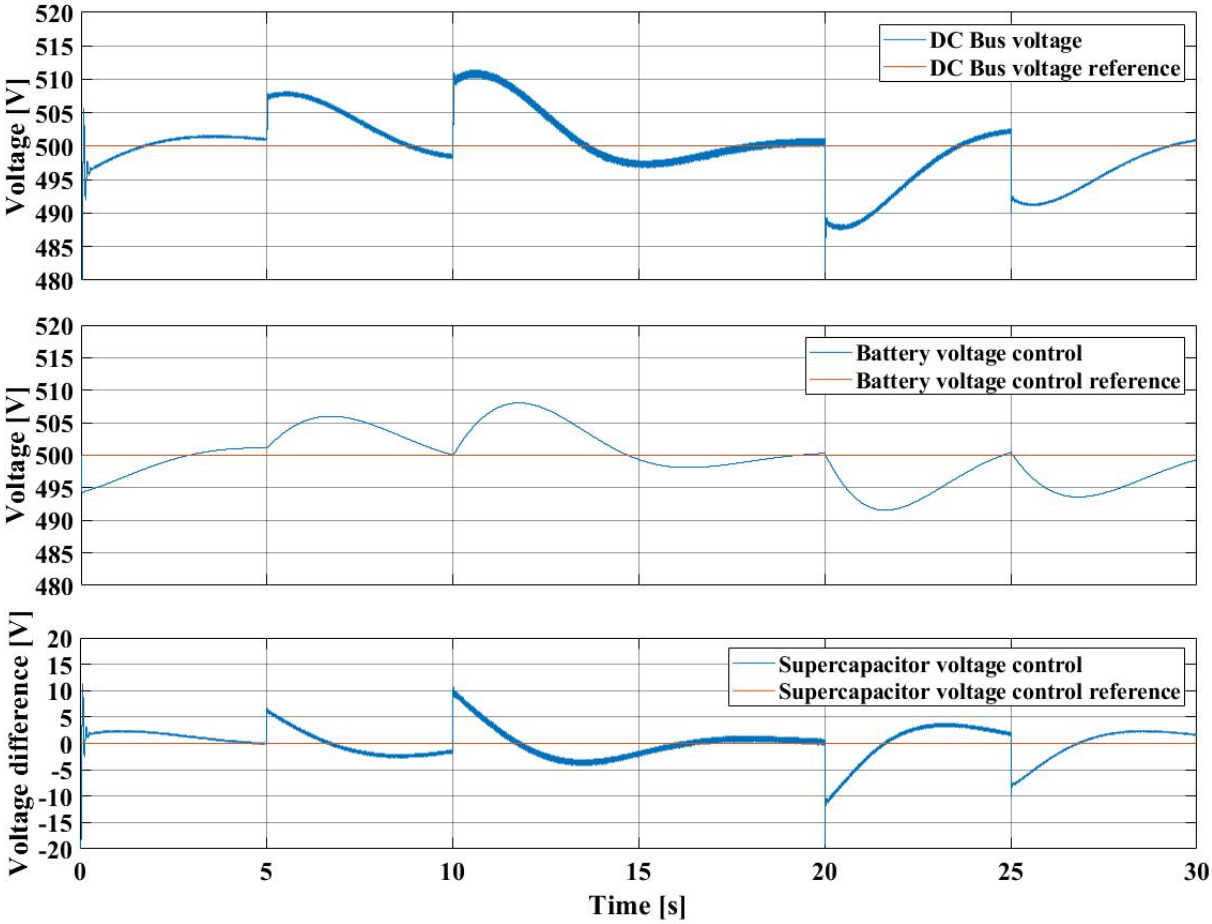

Figure 4-25 DC bus-, battery-, and supercapacitor voltage with the reference voltage in mode of operation 2's load case 1.

Figure 4-26 shows the DC bus voltage plotted together with its reference of 500 V in load case 2 without the supercapacitor. The largest voltage deviations are measured at 64 V.

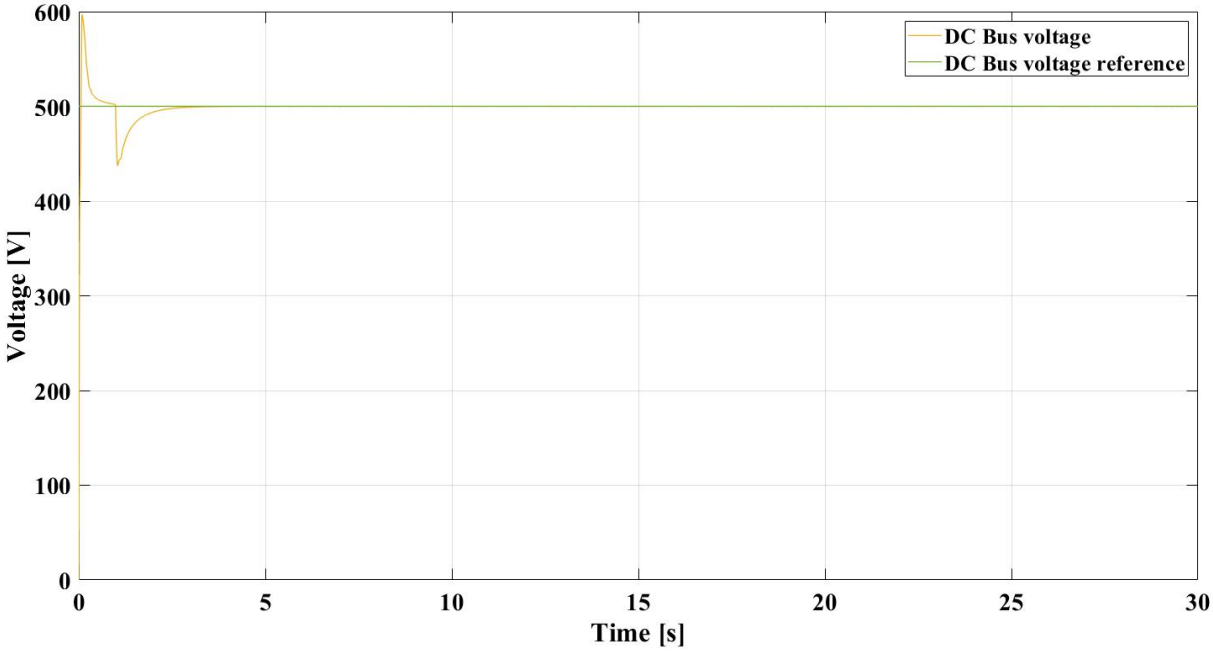

Figure 4-26 DC bus voltage with its reference voltage in mode of operation 2's load case 2 without the supercapacitor.

The DC bus voltage in load case 2 with the supercapacitor installed, plotted together with its voltage reference of 500 V, is shown in Figure 4-27.

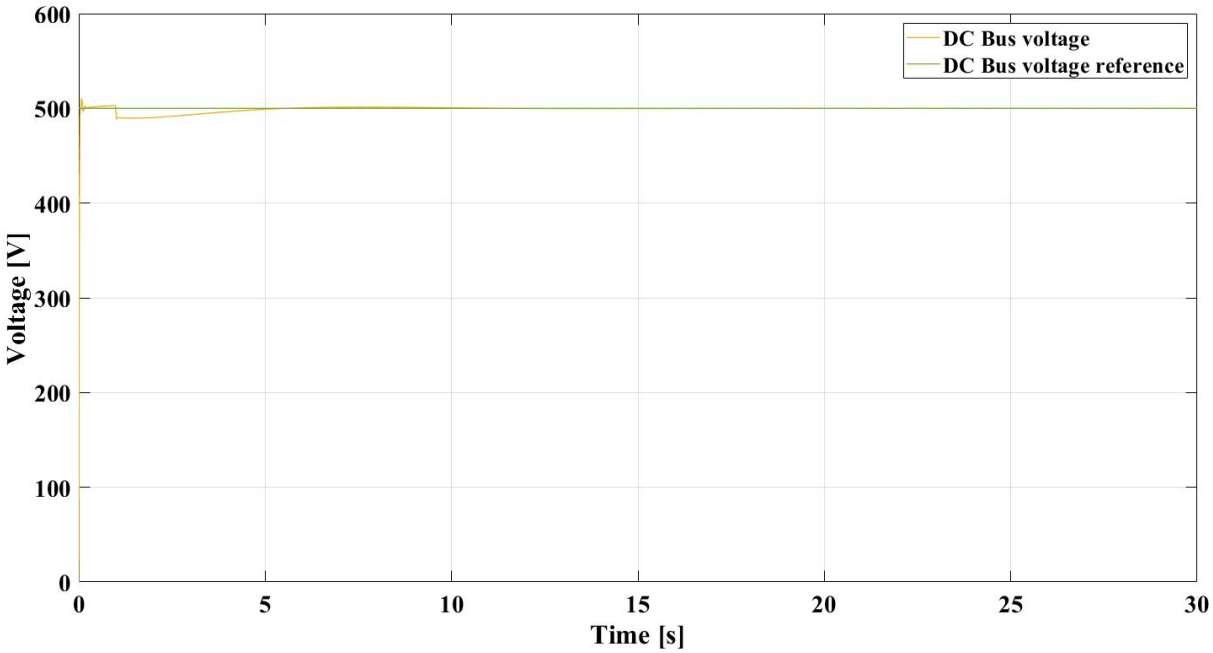

Figure 4-27 DC bus voltage with its reference voltage in mode of operation 2's load case 2 with the supercapacitor.

Figure 4-28 shows a closer look at the DC bus voltage compared with the battery and the supercapacitor voltage control signals in load case 2. The bus voltage in this load case deviates by 3 V above the reference and 10 V below.

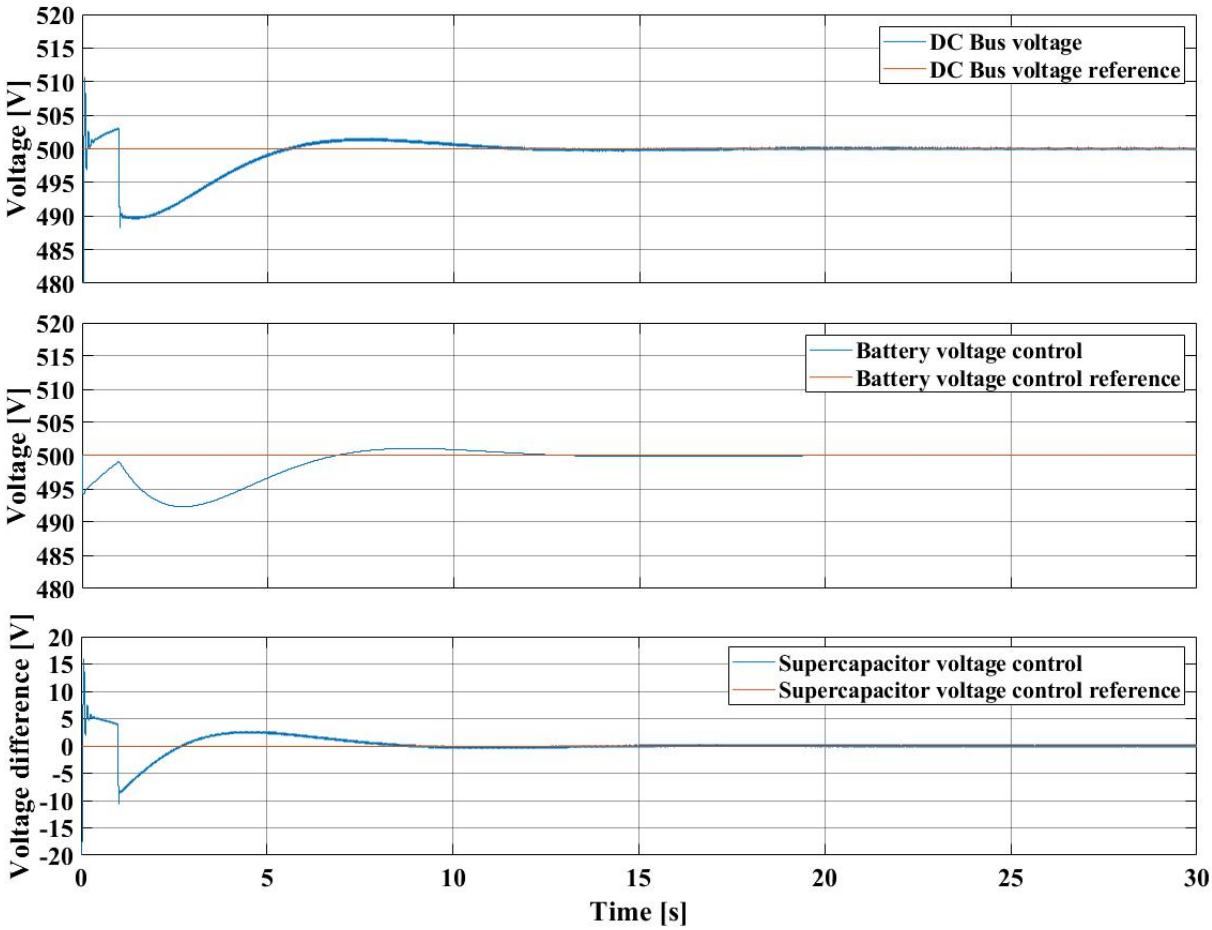

Figure 4-28 DC bus-, battery-, and supercapacitor voltage with the reference voltage in mode of operation 2's load case 2.

4.3.3 Power Electronics

The battery output voltage, current, and SOC in load case 1 without the supercapacitor installed are plotted in Figure 4-29, where the battery voltage varies approximately from 258 to 266 V. The largest measured current is approximately -360 A when charging and 40 A when discharging. The battery's state of charge shows it discharges during the first 5 seconds, then charges until 25 seconds into the simulation and discharges for the last 5 seconds.

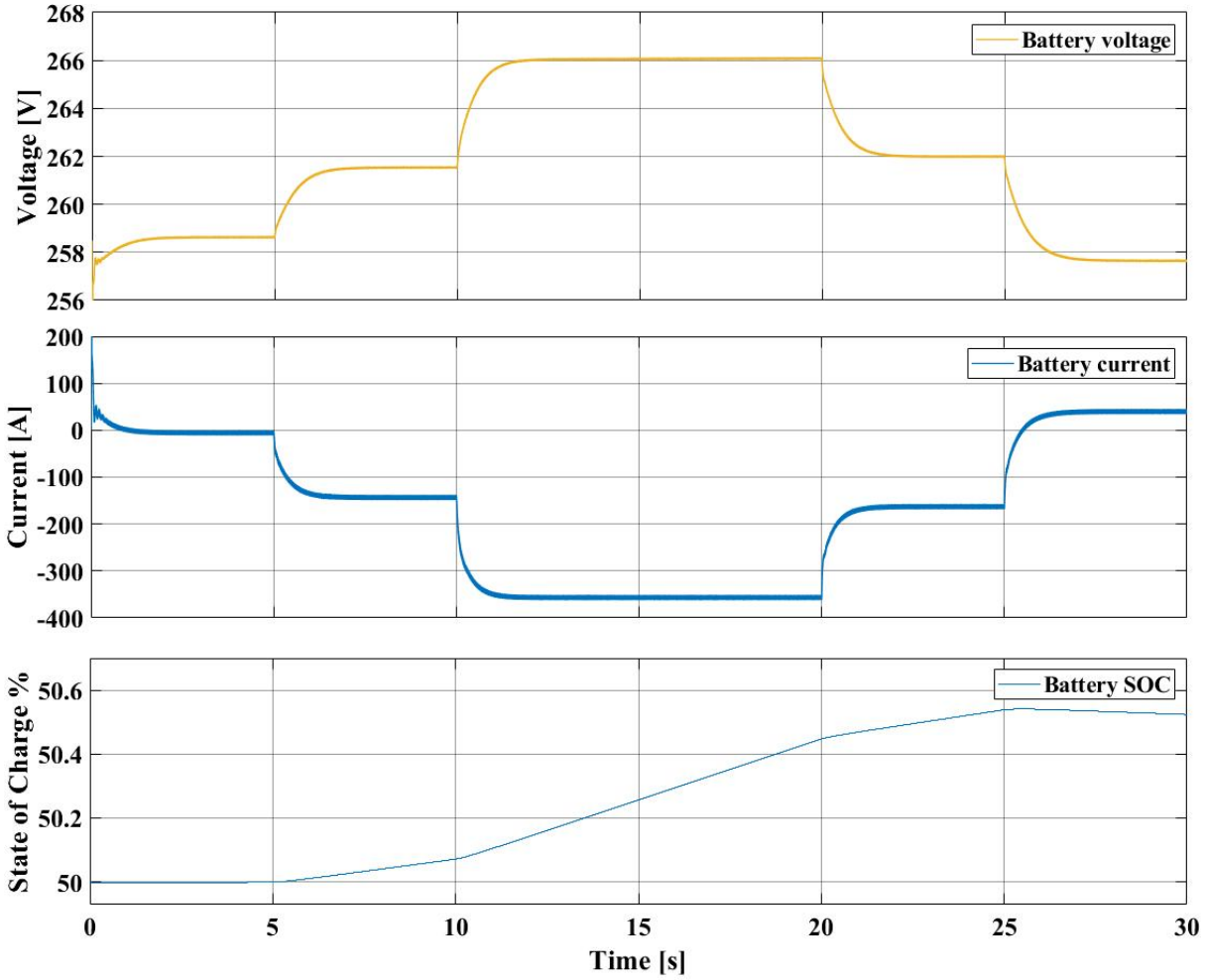

Figure 4-29 Bidirectional battery voltage, -current and SOC in mode of operation 2's load case 1 without the supercapacitor.

The battery output voltage, current, and SOC in load case 1 with the supercapacitor installed are plotted in Figure 4-30. The battery voltage varies approximately from 256 to 266 V, and the largest measured current is approximately -356 A when charging and 140 A when discharging. The battery's state of charge shows it discharges during the first 6 seconds, then charges until 27 seconds into the simulation and discharges for the last 3 seconds.

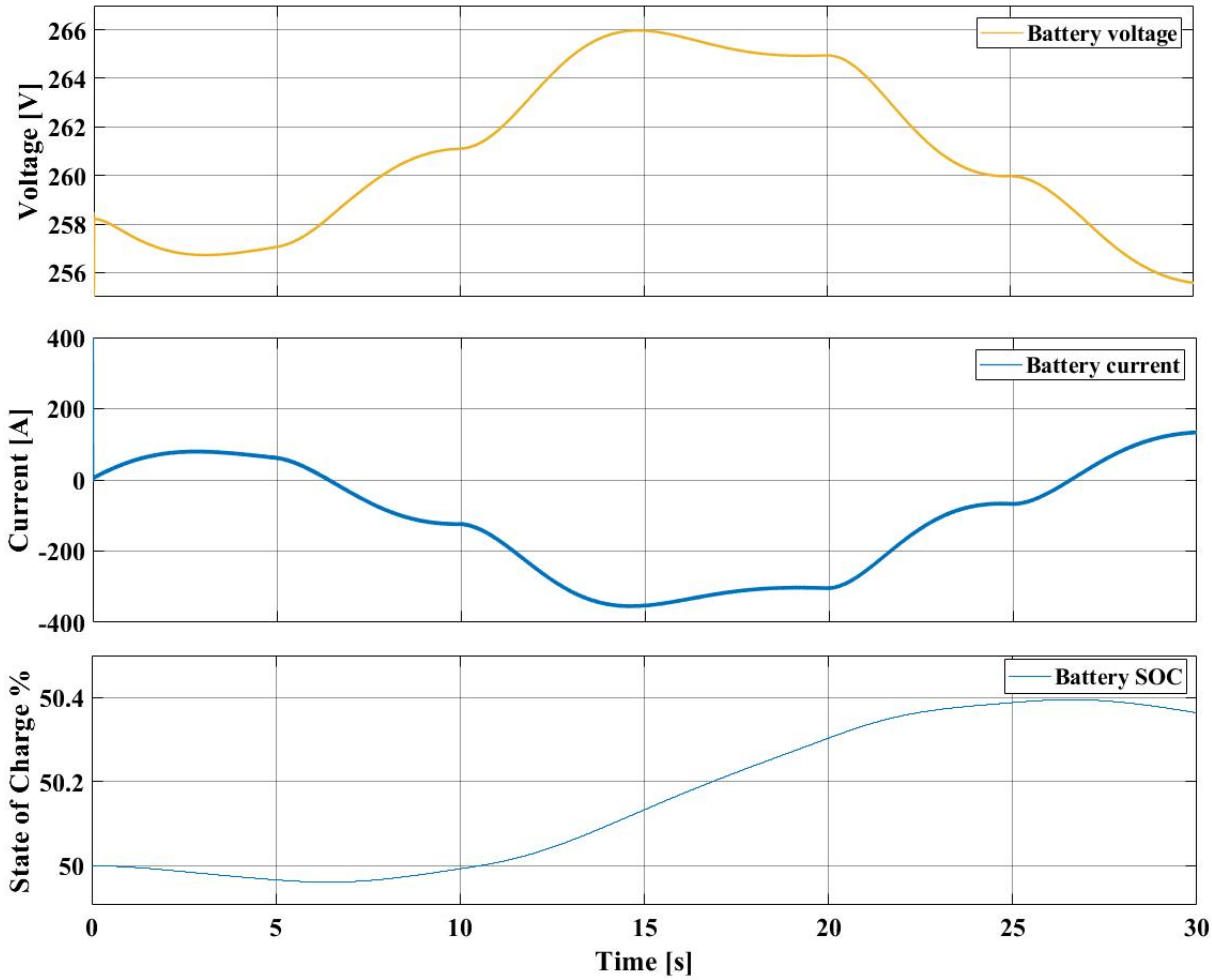

Figure 4-30 Bidirectional battery voltage, -current and SOC in mode of operation 2's load case 1 with the supercapacitor.

The supercapacitor output voltage, current, and SOC in load case 1 are plotted in Figure 4-31. The supercapacitor voltage varies approximately from 240 to 247 V, and the largest measured current is approximately -250 A when charging and 170 A when discharging. The state of charge shows that the supercapacitor is charging during the first 20 seconds, discharging from 20.0 to 22.0 seconds, charging from 22.0 to 25.0 seconds, discharging from 25 to 27 seconds, and charging for the last 3 seconds of the simulation.

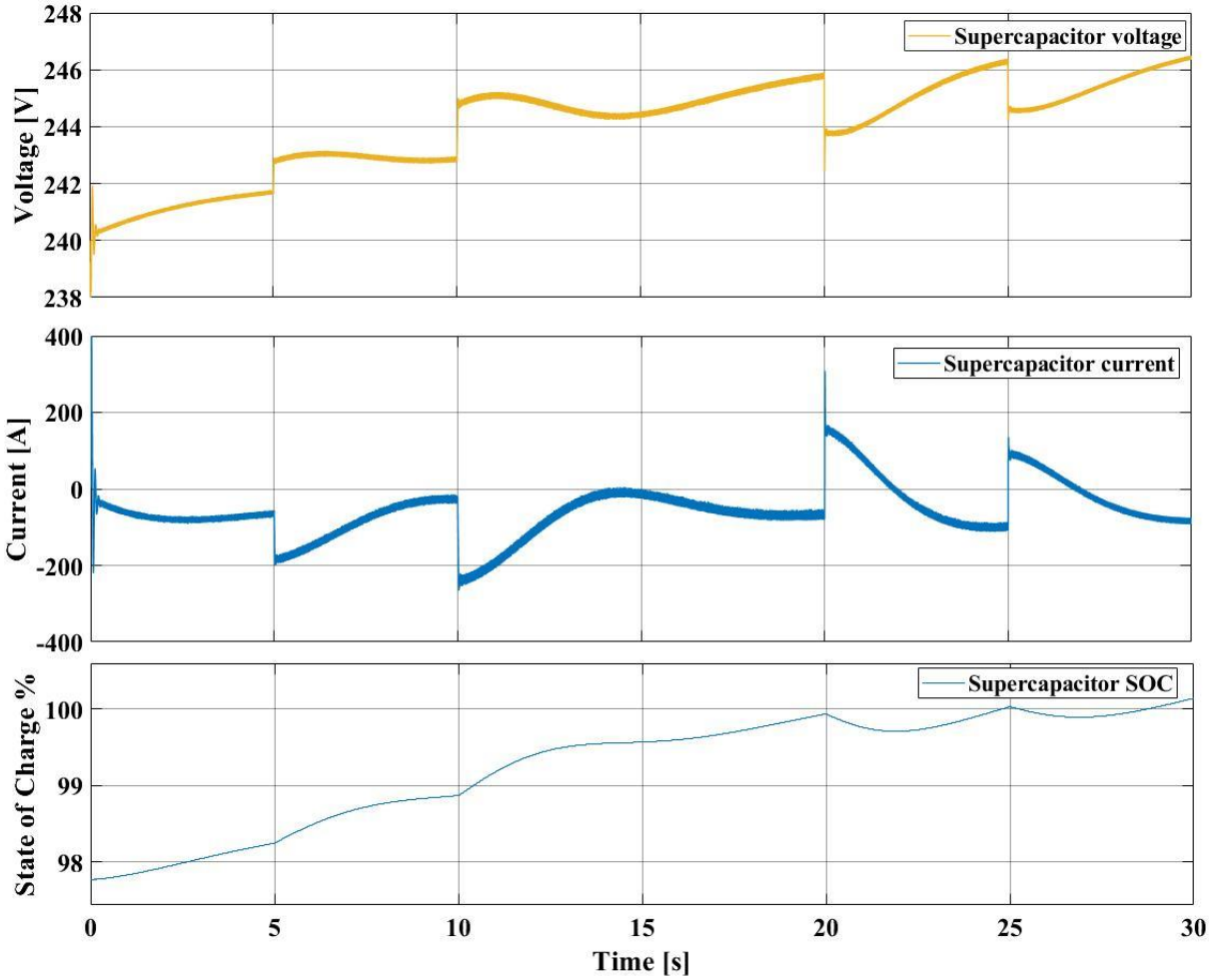

Figure 4-31 Bidirectional supercapacitor voltage, -current and SOC in mode of operation 2's load case 1.

The battery output voltage, current, and SOC in load case 2 without the supercapacitor installed are plotted in Figure 4-32. The battery voltage peaks at approximately 260 V and reaches steady-state at just above 254 V, while the current has a discharging peak at about -90 A and a steady-state current at approximately 190 A. The battery's state of charge shows a constant decrease after the load demands are stabilized.

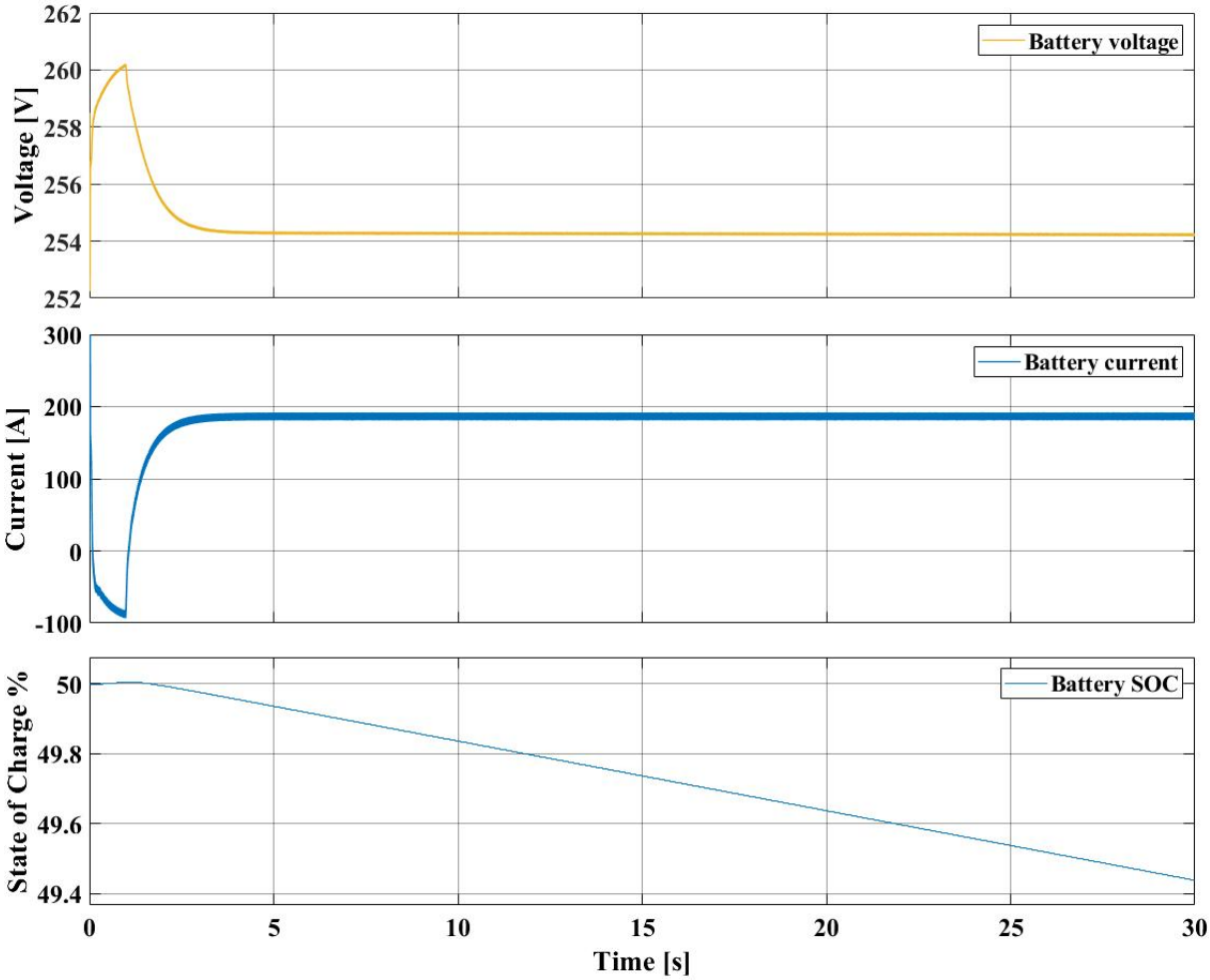

Figure 4-32 Bidirectional battery voltage, -current and SOC in mode of operation 2's load case 2 without the supercapacitor.

The battery output voltage, current, and SOC in load case 2 with the supercapacitor installed are plotted in Figure 4-33. The battery voltages are at its largest just above 258 V and reach steady-state right under 253 V, while the current has a peak just below 300 A and reaches steady-state at about 250 A. The battery's state of charge shows a constant decrease during the load case.

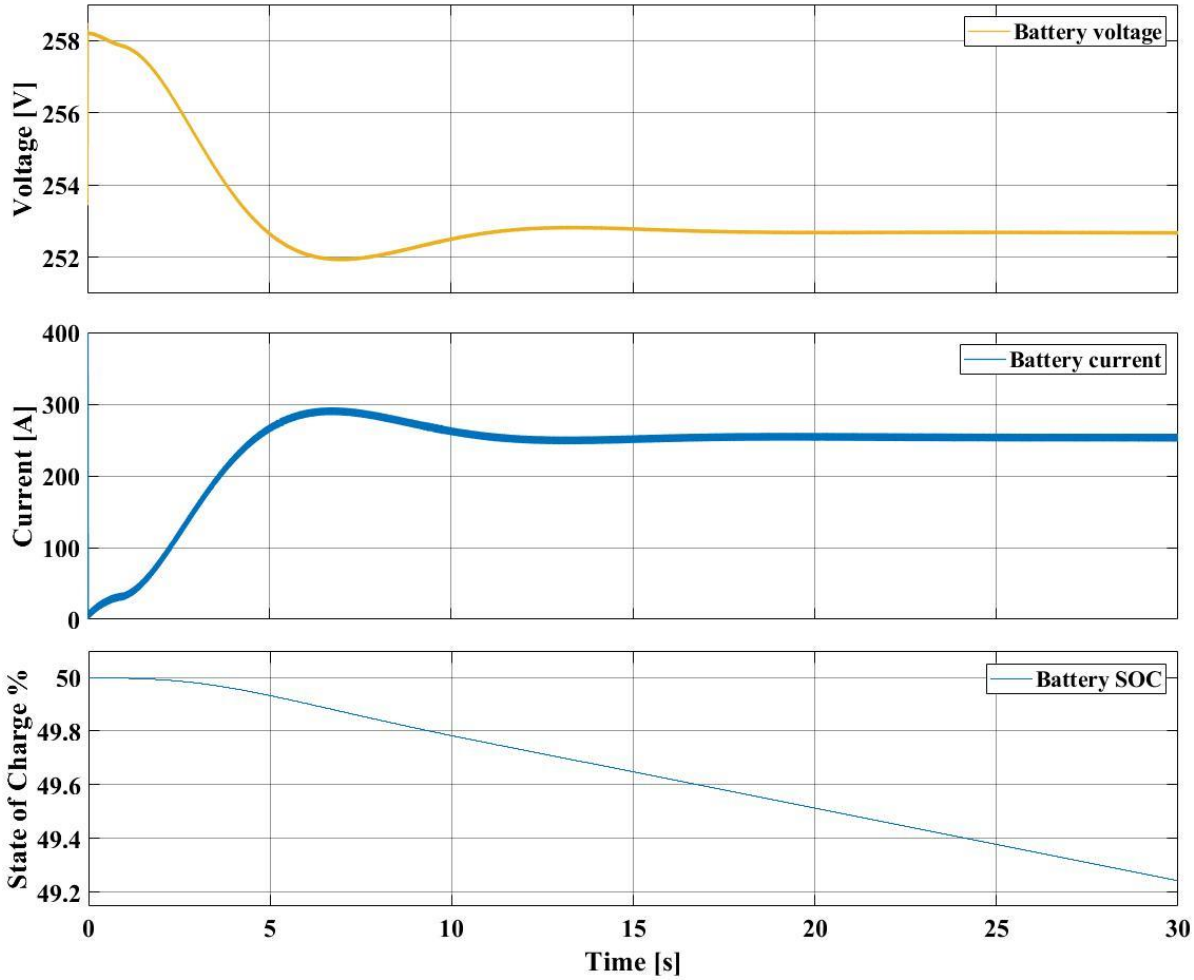

Figure 4-33 Bidirectional battery voltage, -current and SOC in mode of operation 2's load case 2 with the supercapacitor.

The supercapacitor output voltage, current, and SOC in load case 2 with the supercapacitor installed are plotted in Figure 4-34. The supercapacitors voltage varies from approximately 239 to right under 246 V. The current peaks at approximately 130 A and reaches steady state at approximately -50 A. The supercapacitor state of charge shows a constant increase after the load has stabilized.

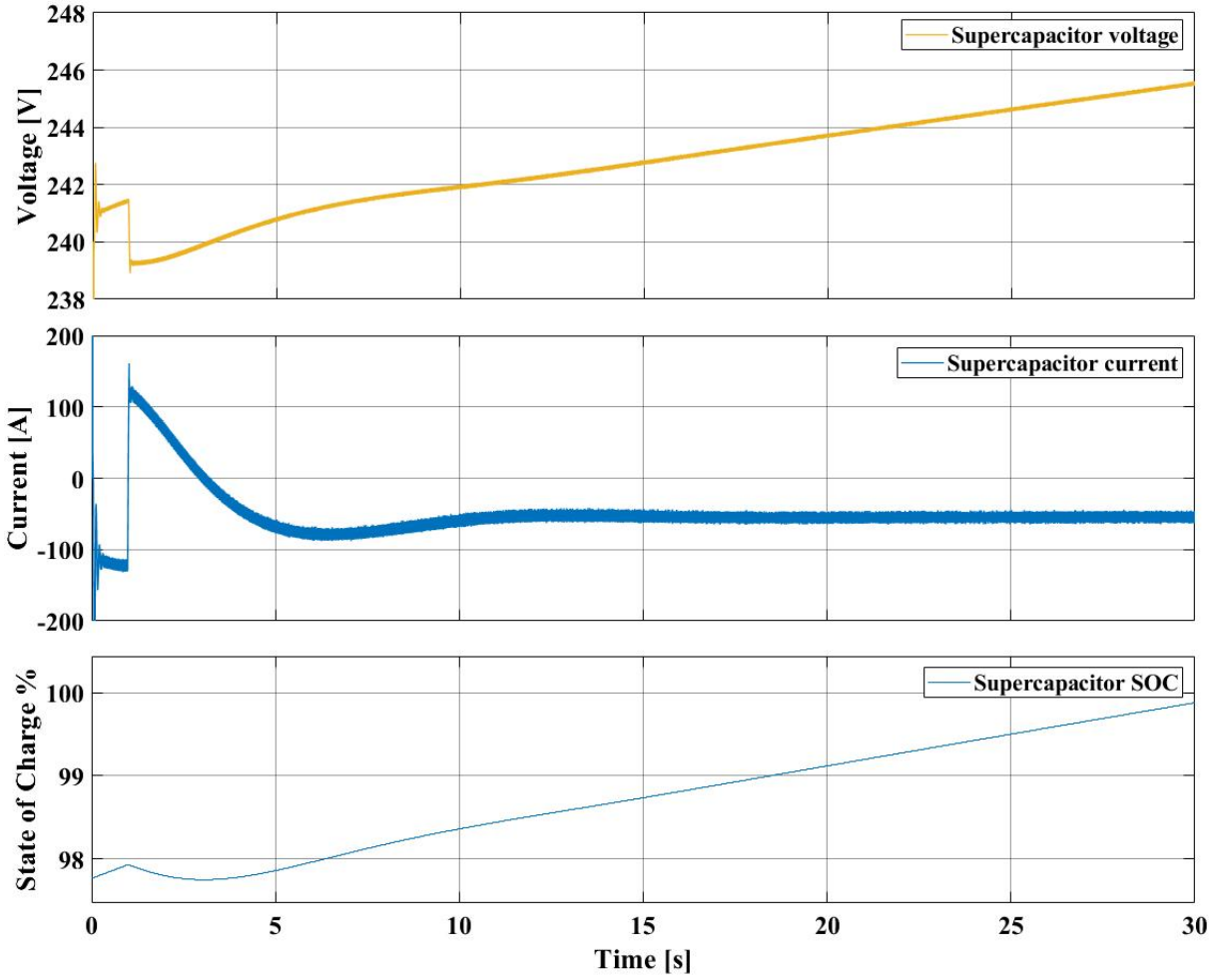

Figure 4-34 Bidirectional supercapacitor voltage, -current and SOC in mode of operation 2's load case 2.

4.4 Mode of Operation 3

Mode of operation 3 uses the generator system to regulate the DC bus voltage through a VSR controlled, active rectifier. The generator operates at nominal speed and exciter-controlled field voltage based on the terminal voltage. The battery system operates in current-mode and undertakes the saturation of the load demand.

4.4.1 Power Shares

The simulated power shares to meet the load demand in load case 1 is displayed in Figure 4-35. Since the power produced by the PV array is considered non-dispatchable, the generator- and battery systems compensate for any surplus or lacking power in the system. The generator's power production varies from 22 at its lowest to 34 kW. The battery pack is charging with a maximum power of 82 kW and discharging with a maximum power of 18 kW.

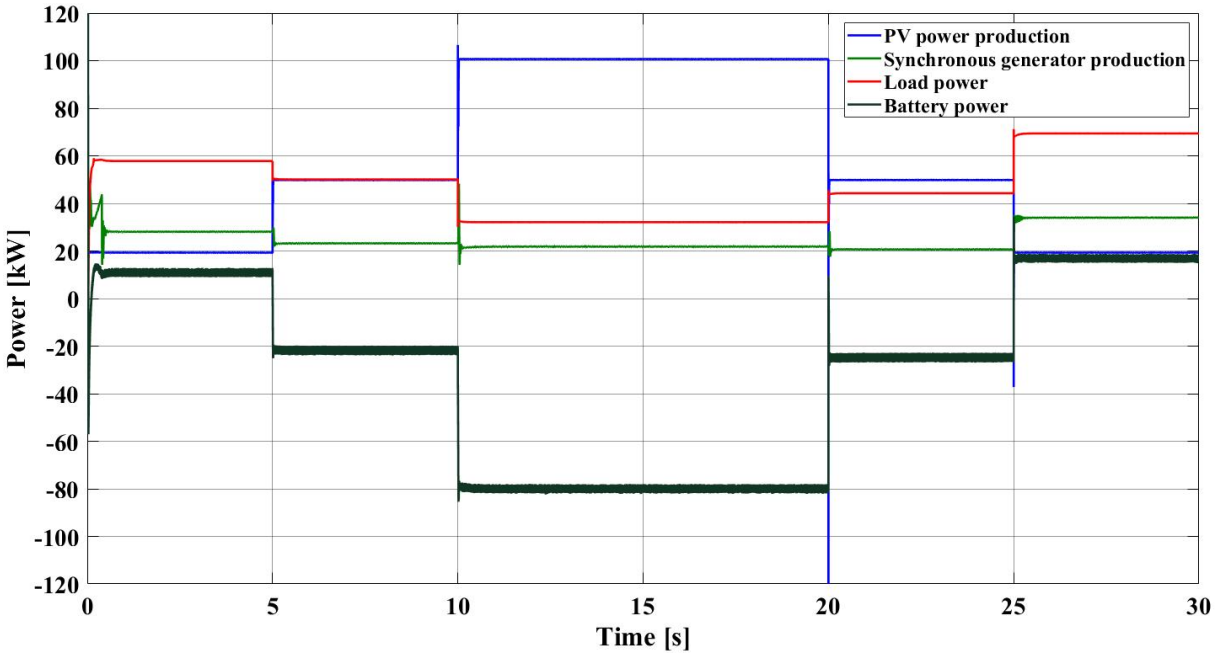

Figure 4-35 The power shares to meet the load demand in mode of operation 3's load case 1.

The power shares to meet the load demand in load case 2 is plotted in Figure 4-36. As the load is constantly set to 69 kW, the generator, along with the battery system, compensates for the required load. Consequently, the generator provides 35 kW, and the battery system provides 34 kW to the system in steady-state.

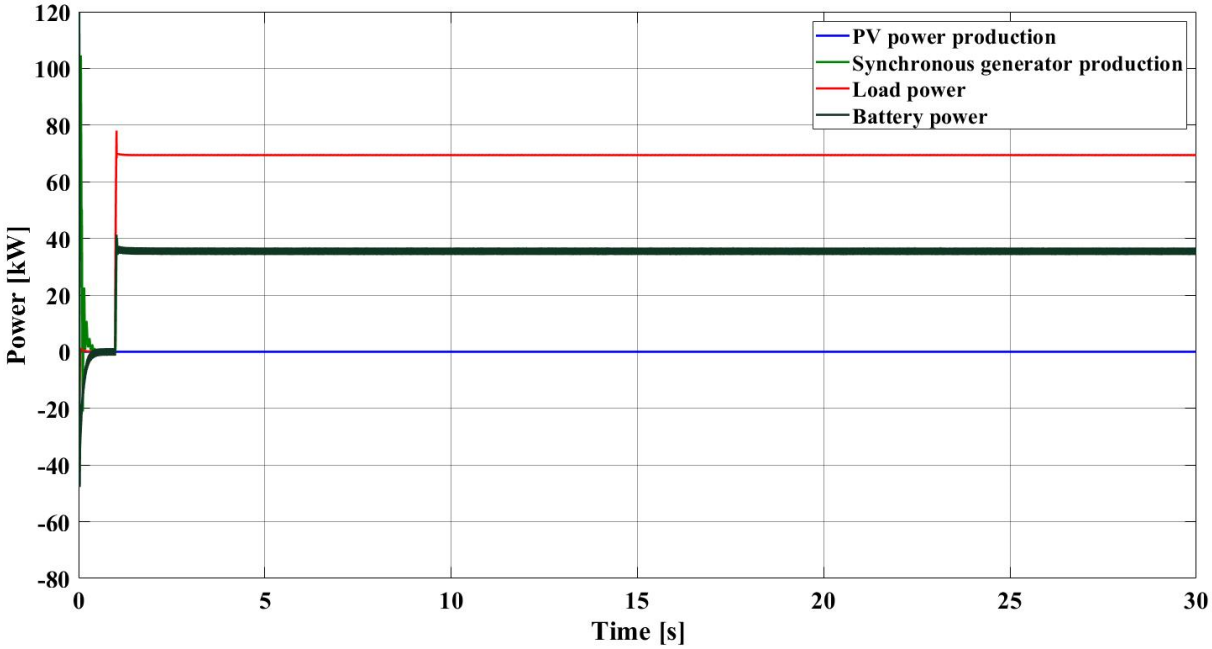

Figure 4-36 The power shares to meet the load demand in mode of operation 3's load case 2.

4.4.2 Control System

Figure 4-37 shows the simulated DC bus voltage in load case 1, plotted together with its reference voltage of 500 V.

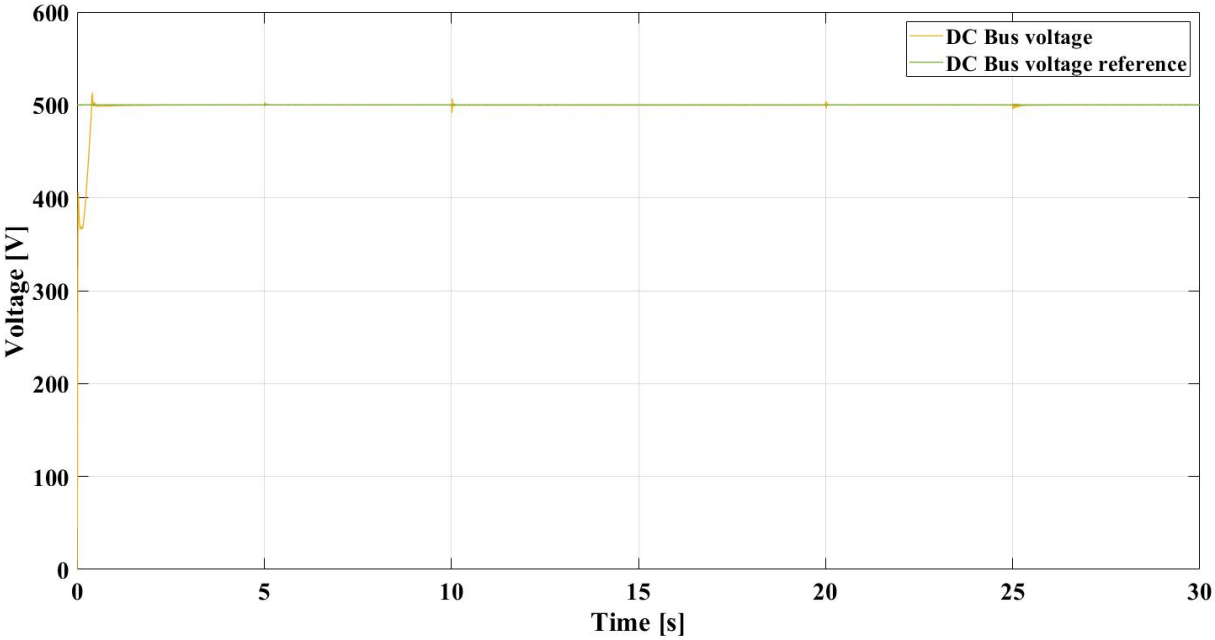

Figure 4-37 DC bus voltage with its reference voltage in mode of operation 3's load case 1.

A closer look at the simulated DC bus voltage in load case 1 is shown in Figure 4-38. The highest measured bus voltage deviations, both appearing at the 10 seconds mark, are first 8 V below, followed by 6 V above the reference value.

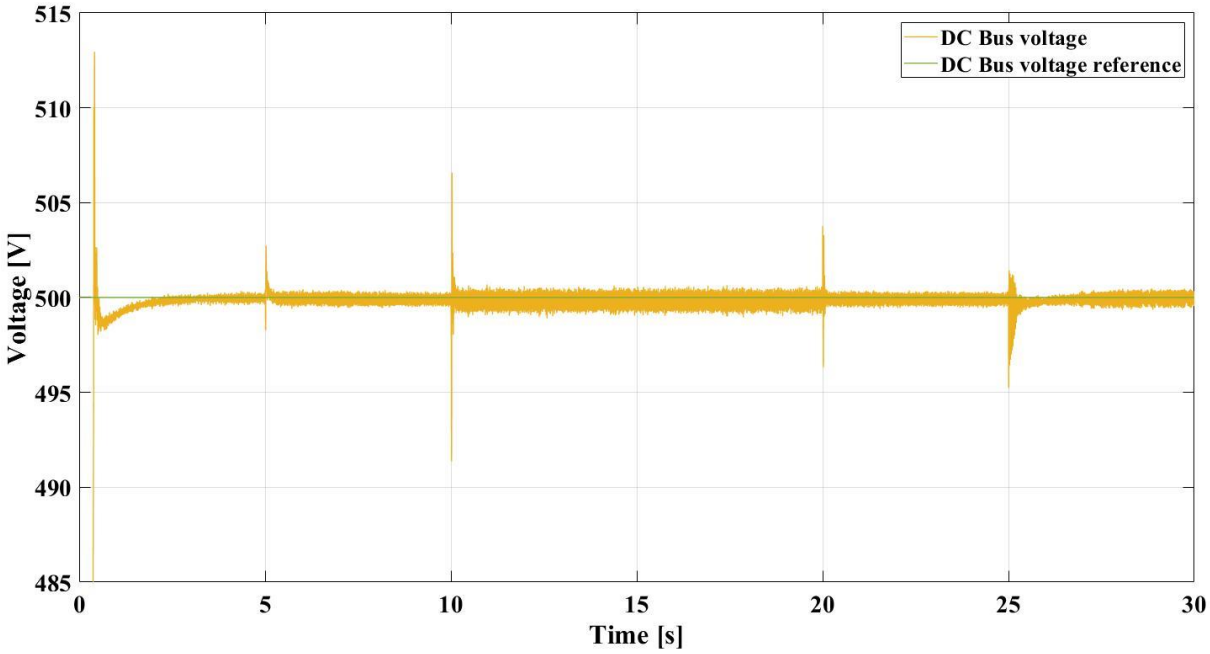

Figure 4-38 A closer view of the DC bus voltage in mode of operation 3's load case 1.

Figure 4-39 shows the DC bus voltage in load case 2, plotted together with its reference of 500 V.

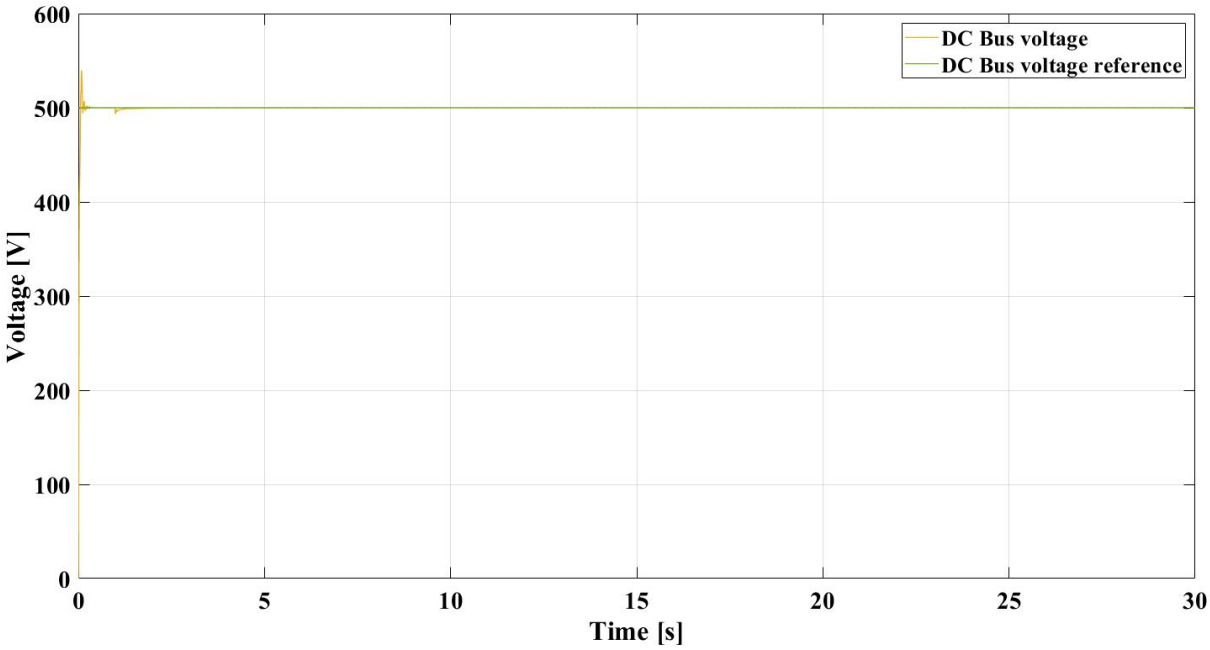

Figure 4-39 DC bus voltage with its reference voltage in mode of operation 3's load case 2.

A closer view of the simulated DC bus voltage in load case 2 is shown in Figure 4-40. The largest voltage deviations are measured at 6 V.

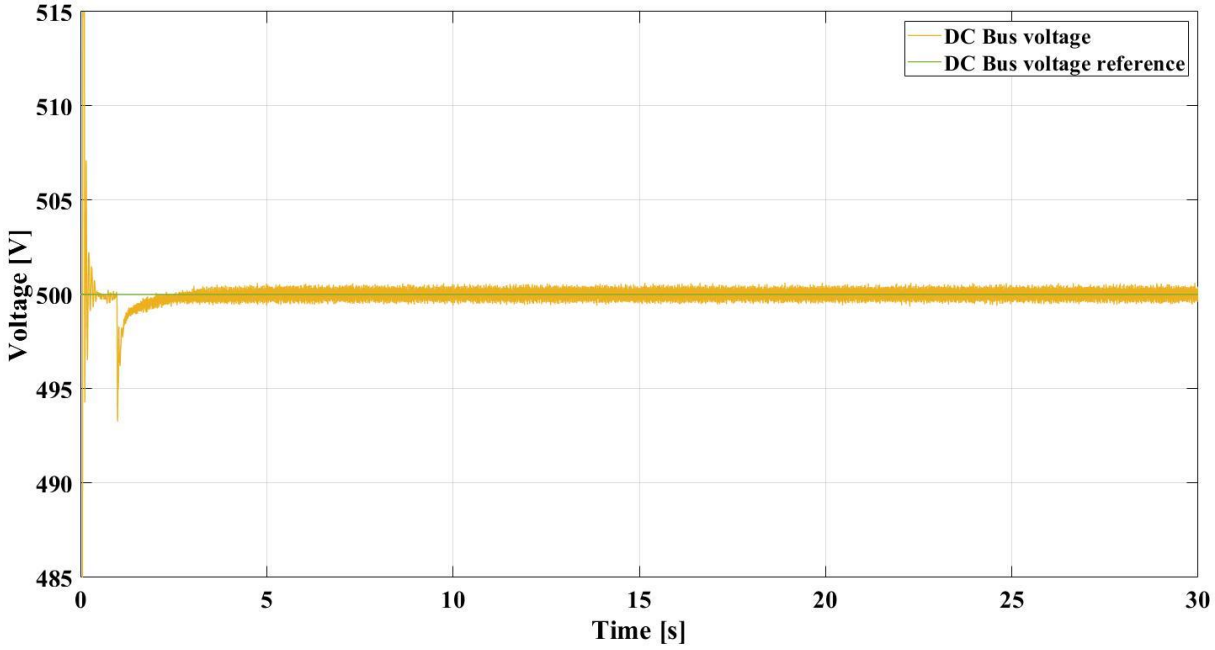

Figure 4-40 A closer view of the DC bus voltage in mode of operation 3's load case 2.

Figure 4-41 shows the measured three-phase voltage waveforms, V_{abc}, from the AC bus and the VSR controller's respective transformed two projections, V_d and V_q. The rms phase voltage is measured at 230 V.

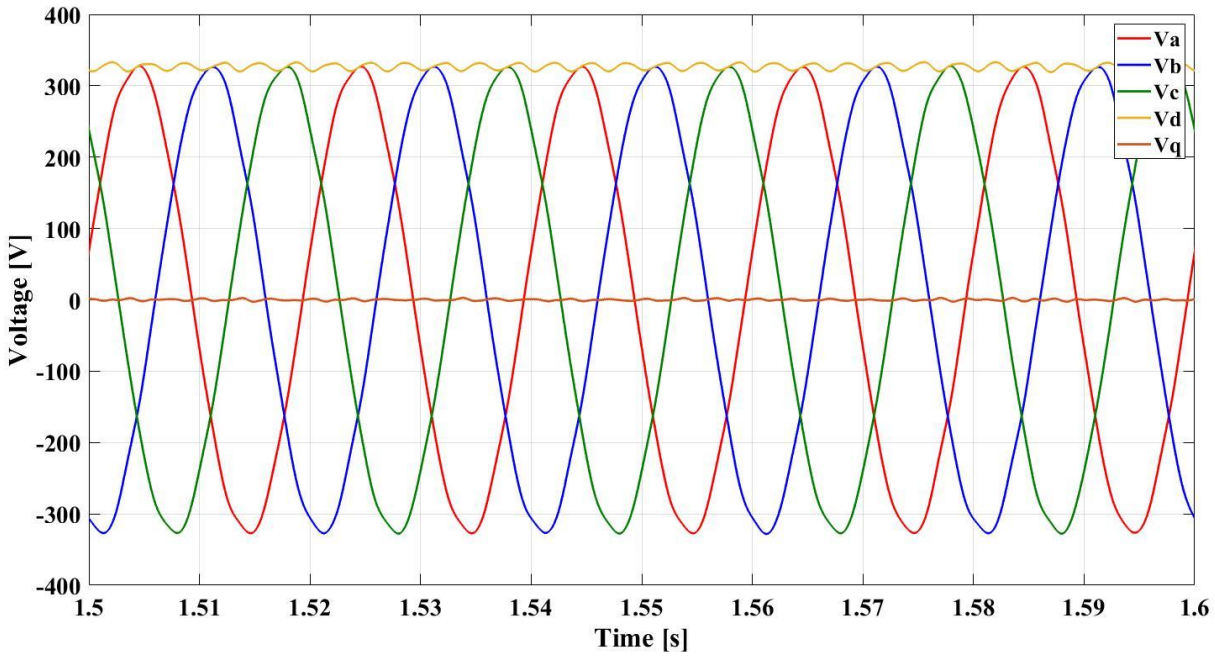

Figure 4-41 Steady-state voltage waveform, V_{abc}, and projected voltages, V_d and V_q, from the AC bus in an instance of mode of operation 3.

Figure 4-42 shows the measured three-phase current waveforms, I_{abc}, from the AC bus and the VSR controller's respective d- and q transformed projections, I_d and I_q. The rms phase current is measured at 40 A at this particular instance.

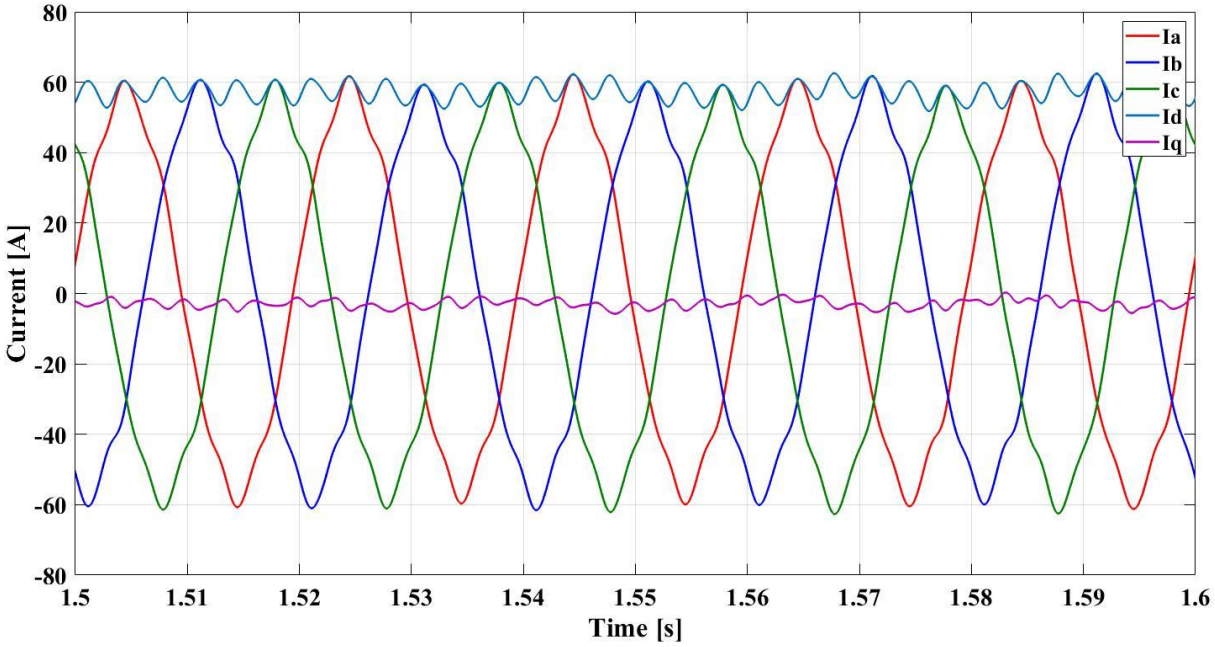

Figure 4-42 Steady-state current waveform, I_{abc}, and projected currents, I_d and I_q, from the AC bus in an instance of mode of operation 3.

The measured d- and q current projections, I_d and I_q, from the AC bus in load case 1 are shown with the control system's corresponding reference's in Figure 4-43.

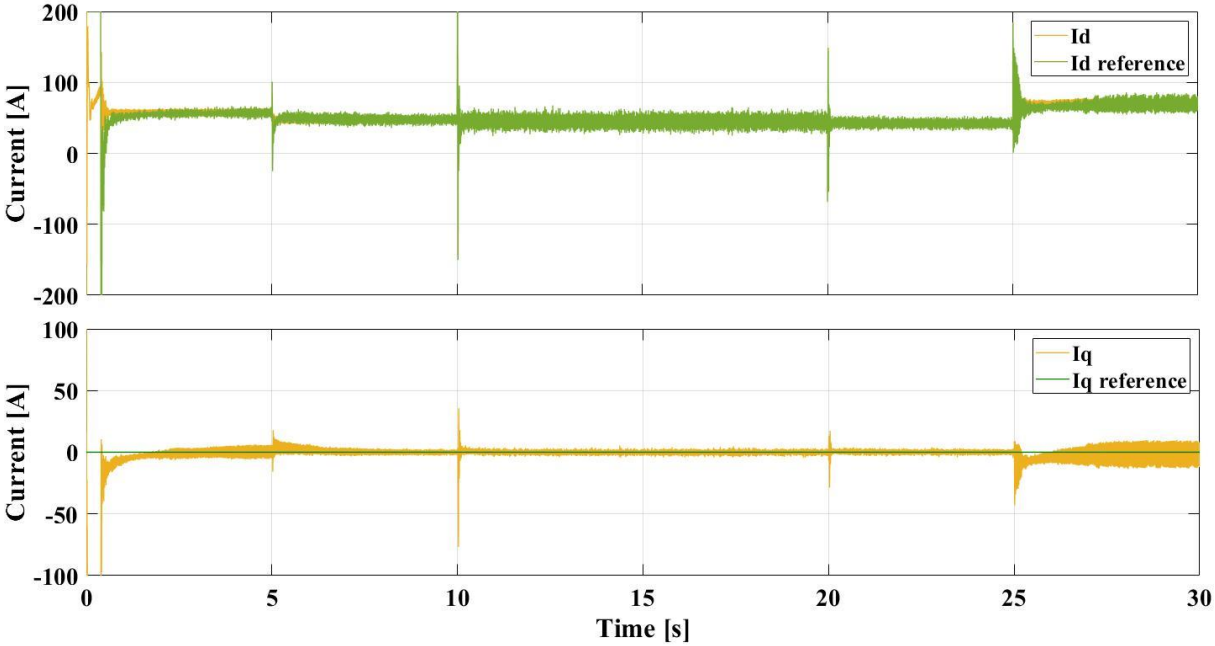

Figure 4-43 Measured d- and q projections of the current, I_d and I_q, with its reference values in mode of operation 3's load case 1.

Figure 4-44 shows the derived reference d- and q projected voltages, V_d and V_q, from the VSR controller in load case 1.

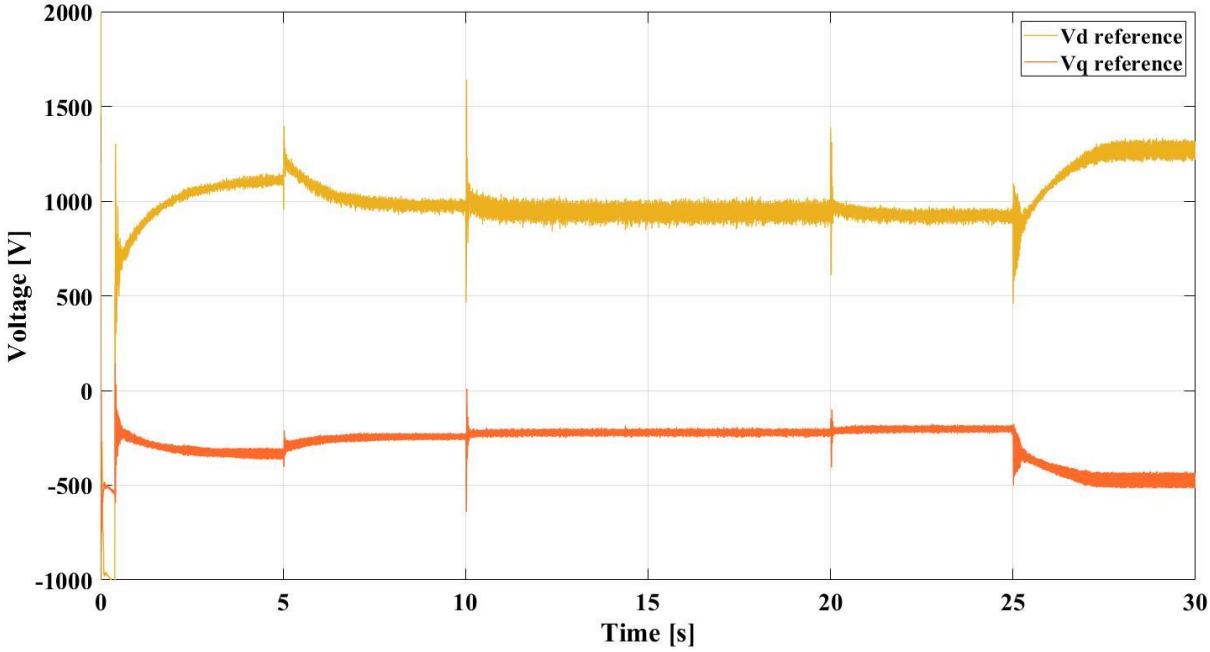

Figure 4-44 VSR controller's derived d- and q projected voltage references, $V_{d,ref}$ and $V_{q,ref}$, in mode of operation 3's load case 1.

The measured d- and q current projections, I_d and I_q, from the AC bus in load case 2 are shown with the control system's corresponding reference's in Figure 4-45.

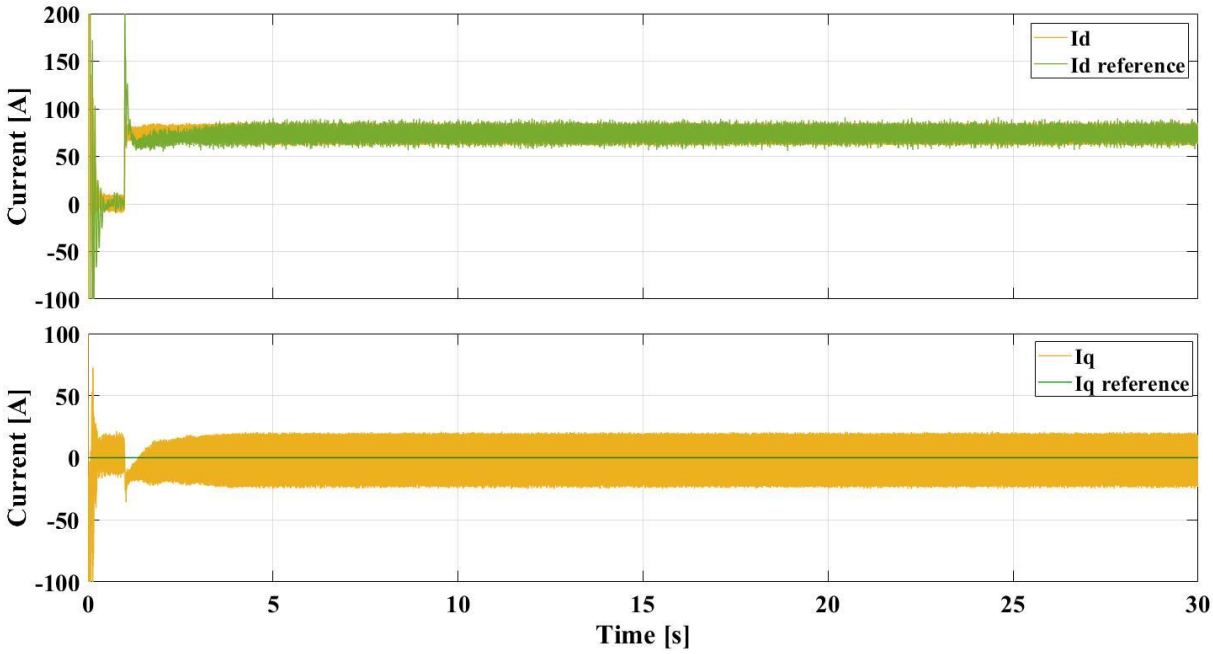

Figure 4-45 Measured d- and q projections of the current, I_d and I_q, with its reference values in mode of operation 3's load case 2.

Figure 4-46 shows the derived reference d- and q projected voltages, V_d and V_q, from the VSR controller in load case 2.

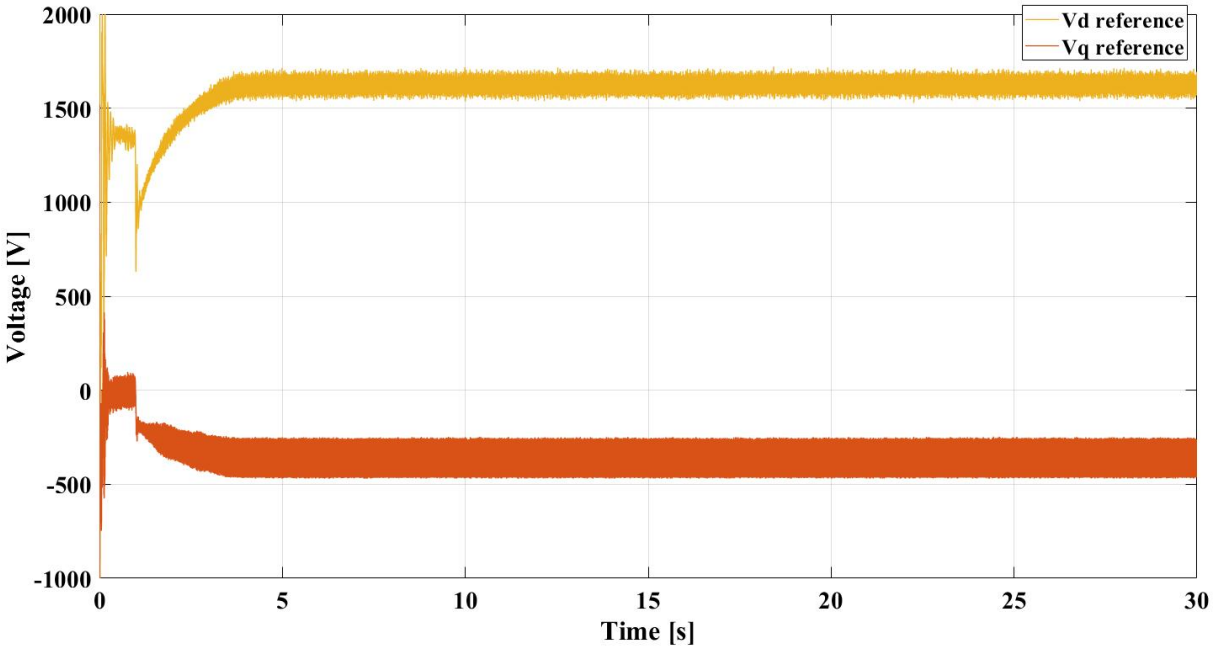

Figure 4-46 VSR controller's derived d- and q projected voltage references, $V_{d,ref}$ and $V_{q,ref}$, in mode of operation 3's load case 2.

The VSI control loop's reference voltage waveform, $V_{abc,ref}$, portrayed with its originating d- and q projected voltages, V_d and V_q, are shown in Figure 4-47.

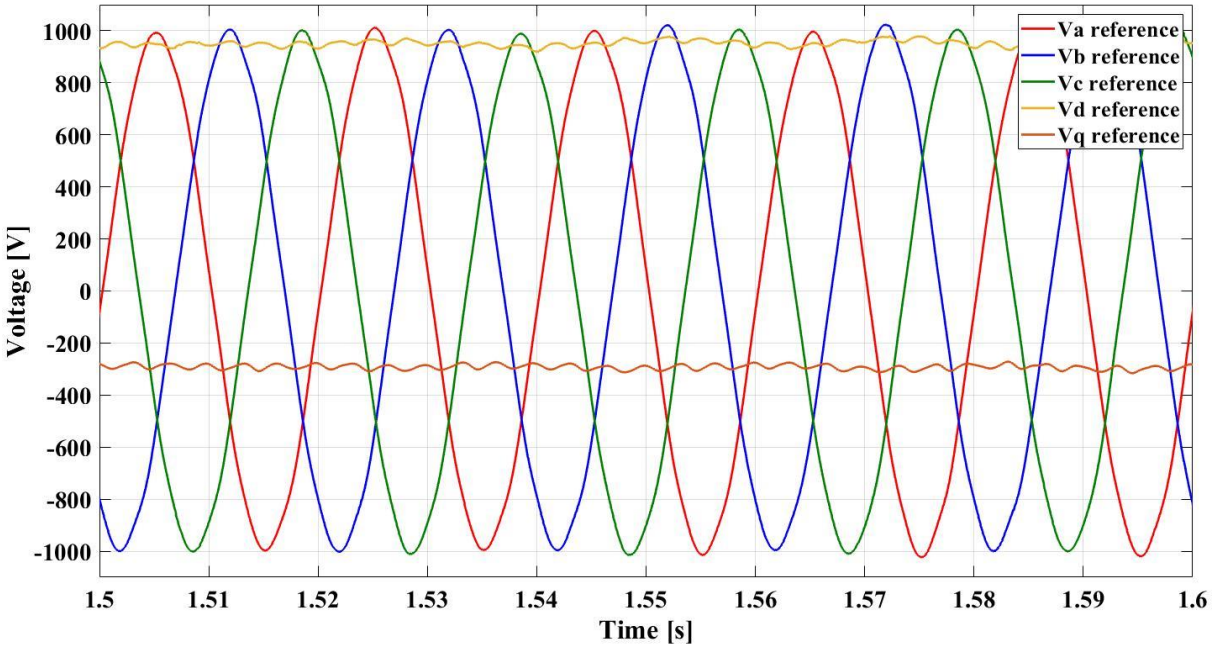

Figure 4-47 Reference three-phase abc waveform, V_{abc}, derived from the VSR controller in a steady-state instance of mode of operation 3.

4.4.3 Power Electronics

The battery output voltage, current, and SOC in load case 1 are plotted in Figure 4-48, where the battery voltage varies approximately from 257 to 265 V. The largest measured current is approximately -300 A when charging and about 70 A when discharging. The battery's state of charge shows it discharges during the first 5 seconds, then charges until 25 seconds into the simulation and discharges for the last 5 seconds.

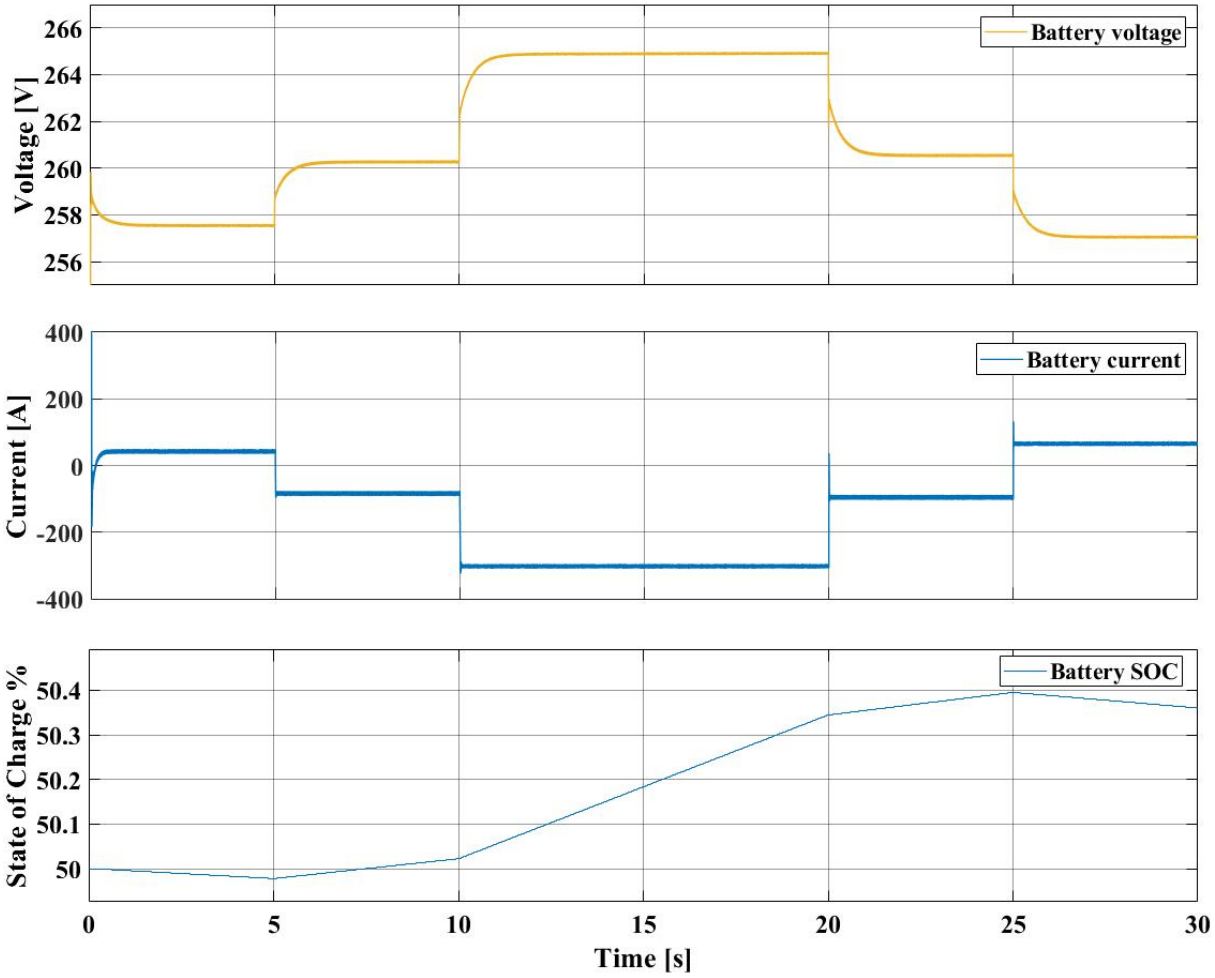

Figure 4-48 Bidirectional battery voltage, -current and SOC in mode of operation 3's load case 1.

The battery output voltage, current, and SOC in load case 2 are plotted in Figure 4-49. The battery voltage is at its largest at about 257 V and reaches its steady-state at just above 255 V, while the current is at its largest at 144 A, which is also its steady-state current. The battery's state of charge shows a constant decrease after steady-state is reached.

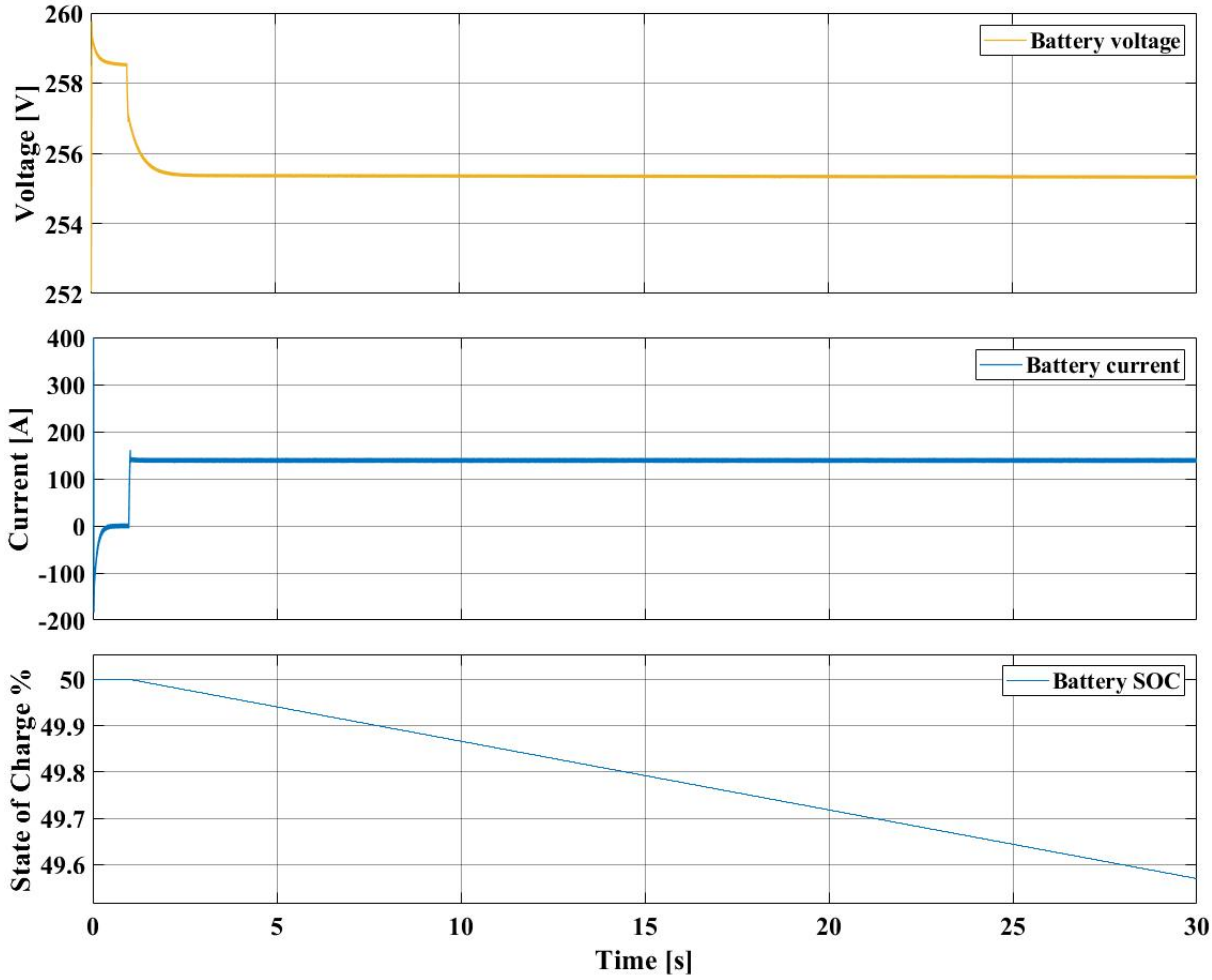

Figure 4-49 Bidirectional battery voltage, -current and SOC in mode of operation 3's load case 2.

The AC voltage entering the rectifier is shown in Figure 4-50, comparing the waveforms before- and after the passive filter.

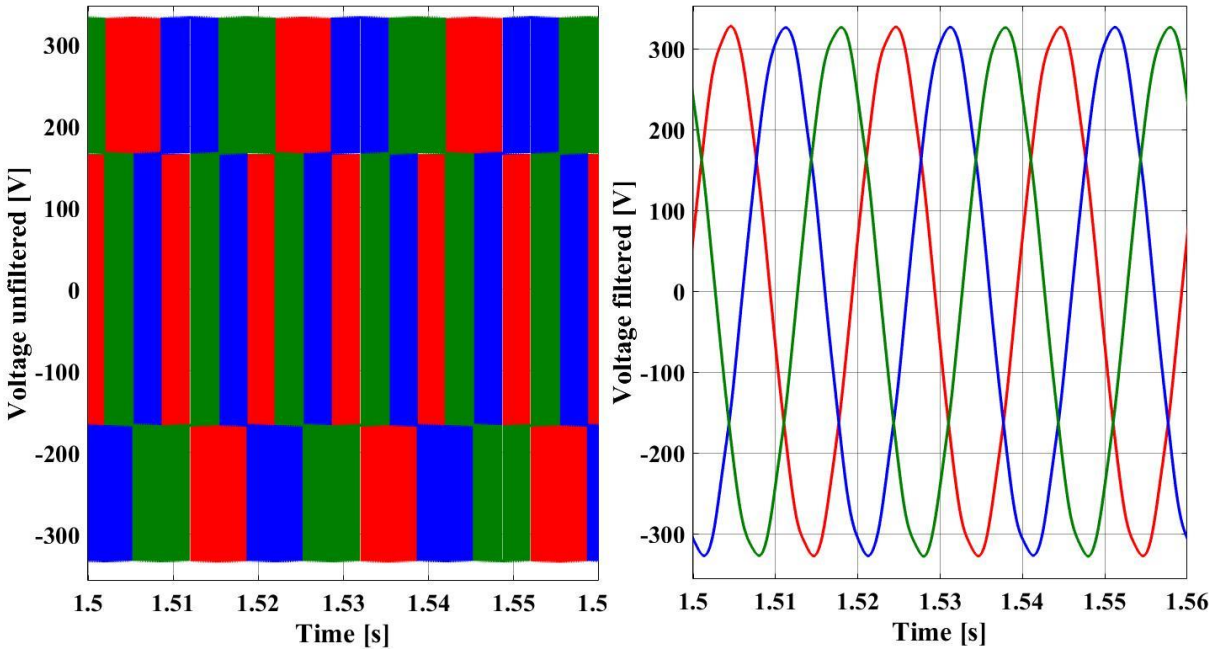

Figure 4-50 AC voltage entering the rectifier before (left)- and after passive inductor filtering (right).

The AC current entering the rectifier is shown in Figure 4-51, comparing the waveforms before- and after the passive filter.

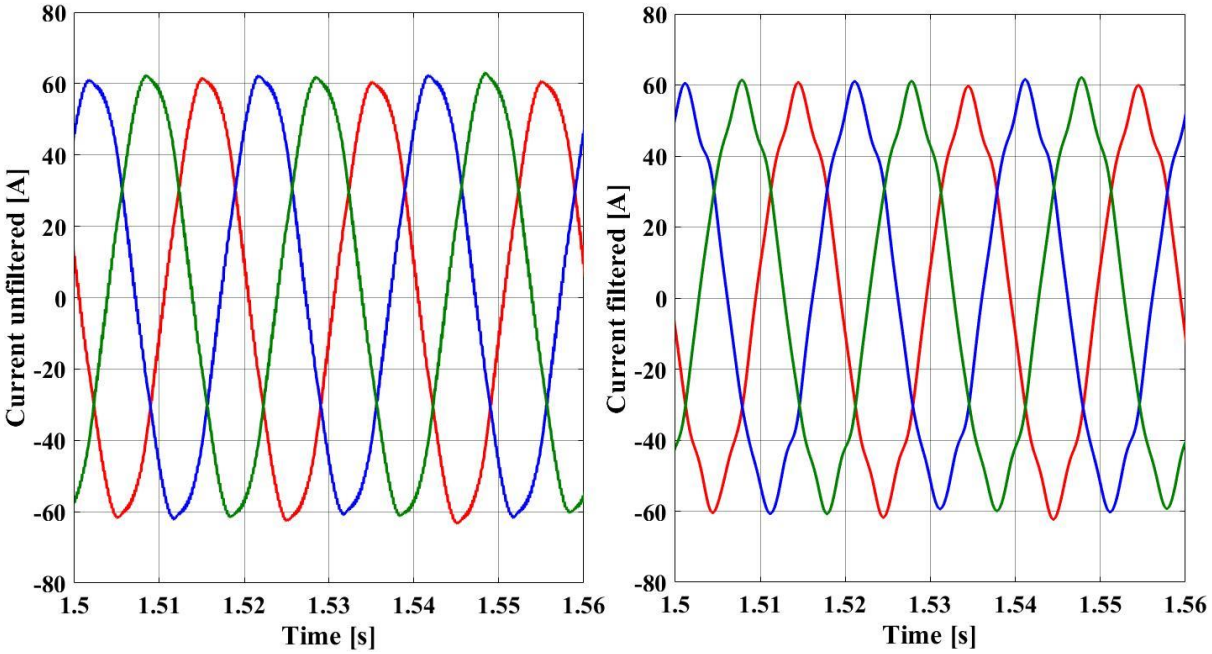

Figure 4-51 AC current entering the rectifier before (left)- and after passive inductor filtering (right).

5 Discussion

This chapter discusses the findings of the simulation model's results, presented in the previous chapter. Results regarding power sharing, the control systems ability to adhere to the DC bus voltage requirements and the handling of its operation points, as well as results regarding power electronic components, are discussed in their respective subsections.

5.1 Power Shares

The objective of the power shares is to saturate the microgrid's load demand by optimally utilising the available power sources. As described in chapter 3, the PV array's produced power follows the predetermined irradiance sequence, shown in Figure 3-2, and the dynamic load demand is set to the load sequence shown in Figure 3-16. The advantage of using the same predetermined load and PV power is that the results from each mode of operation are easily compared to perform the analysis conducted in this segment.

In the first mode of operation, the DC bus is regulated by the available energy storage system, while the generator system operates with constant rotation speed and with constant field voltage, resulting in a constant power influx. The first load case in load case 1, shown in Figure 4-1, undertakes the DC bus regulation exclusively with the battery system. the power sharing scheme shows that the power contribution of the battery is first negative, and then becomes positive at the end of the simulation. This shows that the battery system in perfectly capable of functioning in both injection- and extraction mode and the load case is successful in enforcing this. By facilitating this, the energy storage system is able to balance the power shares successfully.

Although the battery system compensates for the system's surplus or absent power, its response time results in a drop in the generators' produced power, which further causes an overshoot when regulating back to its original state. The response time also results in a delayed saturation of the load demand, which can be seen right after the 25-second mark of the simulation. An argument can therefore be had that the repeatedly occurring response delay may put unnecessary strain on both the battery and generator, in addition to restraining the DC load from achieving its required power. For this reason, the supercapacitor is introduced, forming the DC bus regulating HES system.

The power sharing scheme of mode of operation 1 during load case 1 with the supercapacitor installed is shown in Figure 4-2. In this instance, the battery and supercapacitor work together to saturate the load demand. The results show that the supercapacitor tends to the system's rapid power changes, which allows the battery to have a much smoother power flow. By comparing the battery's power flow to the previous scenario, the battery no longer needs to carry out rapid charging and discharging. An argument can be had that this may pose major benefits with regards to prolonging the battery's lifetime by avoiding rapid changes, which may cause permanent damage if persisting over time. Furthermore, as the system is no longer limited to the battery's response time, the generator system is not affected by sudden power changes, and the load demand is able to instantaneously consume the required system power. Consequently, it can be argued that implementing a supercapacitor system in tandem with the battery system increases the robustness of a rapidly changing system and preserves the battery by avoiding unnecessary degradation.

Figure 4-3 shows the first mode of operation during load case 2 where only the battery system controls the DC bus. Initially, the load takes approximately 2 seconds before achieving its rated consumption, and as with the previous load case, the battery's response time causes a disturbance in the load during scenarios of quick transient responses. Comparing this to Figure 4-4, where the HES system is used, the load still takes approximately 2 seconds to achieve its rated consumption, although without disturbance. This supports that the presence of the supercapacitor positively influences the robustness of the power saturation during instances of abrupt load changes. Furthermore, this load case's results inherently exhibit the advantages of having more the one energy source when attaining the NWA concept as the sheer amount of required power may cause an issue if the system relies too much on the storage systems over time. Additionally, it is shown that if one or more power sources fail, the remaining can deliver the required power without the connected appliances suffering from power shortage. This is a trait of the decentralized control topology.

By looking into the sheer amount of power in the system, where the supercapacitor system is present in the same mode and load case, primarily in Figure 4-2 and Figure 4-4, it becomes apparent that there is a higher power production than consumption. Also, it is notable that this disproportion becomes more emphasised during instances of higher power. This may suggest a consumption of power not accounted for and is likely to originate from the ohmic resistances added to the reactive component in the system's DC converter to add a touch of realism to the converters. Furthermore, this is supported by the fact that the imbalance is greater during a period of higher power flux. Similar discoveries can be seen in the scenarios without the supercapacitor involved, although this becomes less apparent due to one less component containing ohmic losses. The same findings are apparent in the subsequent mode of operations as well.

Mode of operation 2's first load case, where the battery system solely controls the DC bus, is shown in Figure 4-19. It shows that the generator system can somewhat compensate for both surplus and absent power for a short amount of time. Therefore, the battery is not subjected to such rapid changes as it did in the previous mode of operation. However, as the battery response time still is considered as limited, the generator must abruptly compensate for the multiple rapid changes, resulting in the generator briefly ramping its produced power by up to 40 kW in very short durations. Over time, this may arguably add mechanical degradation to the generator, adding maintenance expenses to the generator system and making the solution generally unsustainable in the long term. This can be negated by implementing the HES system, as shown in Figure 4-20. In this case, the generator has a more even power profile, where its produced power deviates no more than 10 kW from its 40 kW setpoint. Compared to the previous mode of operation, this poses as a more robust system, as one might expect when adding an extra control element to the system, i.e., the excitation control.

The second mode of operation's second load case, shown in Figure 4-21 and Figure 4-22, displays the same characteristics as the previous load case. Furthermore, arguments regarding how the second load case pose a challenge with regards to depleting storage capacities, stand the same as the previous mode of operation.

It stands to mention that for the simulation of load case 2, with both modes of operation 1 and 2, it seems that the supercapacitor power share never converges to zero after handling the initial spike in load demand. This is an issue related to the control system of the supercapacitor, specifically in the selection of operation points in the high-frequency voltage transient filtering and is further discussed in subchapter

5.2. Another consideration to be had when addressing the second load case for both the first- and the second mode of operation is that when being heavily reliant on the energy storage system's power injection, it poses the question of how long this operation can be sustained without depleting the storage capacity as this may compromise the function of the HES system, and thus the DC bus, entirely.

By examining the third mode of operation's first load case, shown in Figure 4-35, it is evident that the load demand is entirely saturated for the full duration of the simulation, indicating that the VSR controlled rectifier, in conjunction with the battery system, is able to satisfy the power requirements successfully. As the generator is able to indirectly address the demanded load profile, the sheer power contribution supplied by the battery system is generally reduced in comparison to the previous modes of operation, which is evident by comparing the load sharing scheme in mode of operation 3, shown in Figure 4-35, to the load sharing of the two previous modes in Figure 4-1 and Figure 4-19. This is particularly important in safeguarding the battery's SOC parameter. Furthermore, as the battery system is not required to regulate the DC voltage, the battery's response time, in terms of power saturation, is exclusively limited by its current output, resulting in a much faster power regulation than observed in the previous modes of operations.

The fast response time of both the generator and the battery can be observed again for the second load case, shown in Figure 4-36, where both systems immediately respond to the demanded load. Compared to the same load case of the previous modes of operation, this mode appears to incorporate a far more superior stability and robustness with regards to meeting the demanded load, although, at the cost of both the generator and the battery being subjected to more stress.

With regards to the power sharing across each load case, the final of the three proposed modes of operation stands out as the superior option. Even when the two first modes implement their supercapacitors, the third operation mode shows superior robustness and stability.

5.2 Control System

Considering the defined stability criteria in chapter 3, i.e., a maximum DC bus voltage deviation of ± 3 % from the reference value of 500 V, each of the tested modes of operation imposed on this thesis' microgrid model has successfully been implemented with this in mind. By looking into the robustness of mode of operation 1 and 2's control systems' both without- and with the supercapacitor included in the energy storage system, the resulting DC bus voltages, shown in Figure 4-5, Figure 4-6, Figure 4-23, and Figure 4-24, respectively, shows that the microgrid system clearly benefits from the supercapacitor's response time during periods of quick load changes. Of the two modes of operation, the latter shows the most robustness considering the largest DC bus voltage deviations that occur, namely 11 V above the reference and 12 V below the reference, as shown in Figure 4-25. The less robust counterpart to the second operation mode, i.e., mode of operation 1, inheres DC bus voltage deviations of 13 V above the reference and 14 V below, at the most, as shown in Figure 4-7. Although this mode showed less robustness when considering the scope of the voltages the two didn't show much difference. When it comes to the two modes of operation's robustness without the supercapacitor installed, the trend where the first operation mode shows less robustness than the second seems to persist, as seen by comparing Figure 4-5 and Figure 4-23 to each other. Mode of operation 3, however, showed by far the highest robustness of all the tested operation modes. With the greatest deviations at a mere 6 V above the reference and 8 V below the reference, as shown in Figure 4-38. Although this mode of operation shows

a significantly improved robustness, it also seems to incorporate some sizeable ripples when operating in steady-state at large loads.

A similar pattern emerges when looking into the simulation results of load case 2. Initially, each mode of operation takes about two to three seconds to stabilise at its operation point, as shown in Figure 4-8, Figure 4-26, and Figure 4-40 for load cases 1, 2, and 3, respectively. Showing a similar trend to the results of load case 1, but with the robustness of each mode of operation reflecting how long the system takes to reach its value, the first mode of operation takes the longest. However, as expected, when the supercapacitor is added to the two first modes of operation, the system's overshoot is drastically reduced, as shown in Figure 4-10 and Figure 4-28, although the time it takes for the system to stabilise seems to be increased compared to the instance without the supercapacitor. Nevertheless, it should be mentioned that although the time for the system to stabilise is increased, during the majority of the time, the voltage deviations are within 5 V of the reference value in both operation modes. The systems' stability is therefore considered as strengthened with the supercapacitor present. Furthermore, as one might expect with the already established robustness of mode of operation 3, this mode shows superior step response time compared to the two previous operation modes, although the steady-state oscillations highlighted in the previous load case persist in this one too.

Across each load case, the third mode of operation is the one that seemingly undertake the task of stabilizing the DC bus voltage in the best way. Considering the control elements utilized across each mode of operation it is clear that the stability and robustness increases as the complexity of the control system increase. This is based on regarding the VSR control as a more complex control system as the high-frequency voltage transient filter-based cascade control of the HES system.

The power production profile for the PV system used in load case 1, shown in Figure 4-11, shows that a minimal amount of steady-state oscillations is imposed on the system, and the step response time is clearly sufficient. However, the voltage- and current profile compared to the irradiation input of the PV array in Figure 4-12 shows that the voltage parameter indeed incorporates some degree of oscillations, particularly in settings with low irradiance and power production. Considering that the voltage parameter is what imposes the MPPT algorithm on the PV system, this is to be expected. Nevertheless, Figure 4-12 provides a good depiction of how the irradiance mainly drives the PV current, which then, in turn, drives the power output of the PV system. In the context of the entire primary control system of the hierarchical control system, the PV controller is a single objective controller with no particular regard to anything other than injecting the microgrid with as much power as possible. The PV system used in the simulation model covered in this thesis clearly carries out its function successfully, which supports the fact that the selection and implementation of the MPPT method are successful.

The supercapacitor's effect on the system is evident by analysing the DC bus voltage deviations in Figure 4-5 and Figure 4-6 for the first mode of operation and Figure 4-23 and Figure 4-24 for the second mode of operation. This reflects that the high-frequency voltage transient filtering control strategy, introduced in subchapter 2.1.3, has been successfully implemented. As opposed to the component application where the supercapacitor is excluded, and the DC bus voltage is governed entirely by the battery pack, the DC bus voltage measurement in the HES system is undergoing a low-pass filtering as explained in subchapter 3.2.3. Consequentially, in addition to the cascade controller's PI parameters, the control system's performance in this application is also inherently dependent on the low pass filter to encompass an appropriate time constant in order to ensure that the filter picks up only the fastest bus voltage deviations.

However, when simulating load case 2, it becomes apparent that there persists an inherent flaw in this function, whereas Figure 4-4 and Figure 4-18 for mode of operation 1, and Figure 4-22 and Figure 4-34 for mode of operation 2 show that when the system is at stable operation, the supercapacitor depletes power from the system when it clearly should not. Despite this, the graph of the supercapacitor's operation point regulation in Figure 4-10 and Figure 4-28 for mode of operation 1 and 2, respectively, shows that the two supercapacitor controllers successfully regulate their portion of the DC bus voltage towards zero. This suggests that the low pass filter that sets the feedback signal of the supercapacitor controller is not optimally configured. More specifically, their time constant doesn't incorporate the necessary value to realistically reflect the supercapacitor's desired role in the load sharing scheme even though the DC bus voltage is satisfactory. However, this reflects the energy storage system's role in the context of the primary control level of the hierarchical control as a multi objective controller where the primary control parameter is the DC bus voltage, and the secondary is the corresponding load injection.

The relationship between the primary- and secondary objectives of the control system of the first two load cases can be described as follows:

- The battery, and supercapacitor when applied, oversees maintaining the DC bus voltage to its desired value. Since the cascade controller used to undergo this regulation use the DC bus voltage as the main reference and feedback signal, as explained in subchapter 3.2.2 and 3.2.3, this is classified as the primary objective of the controller.

- As a secondary repercussion of the voltage adjustment, the amount of power in the system will be affected accordingly. More specifically, whenever there occurs a power surplus- or deficit in the system, this will manifest itself in the DC bus voltage as a rise or drop, respectively. Therefore, the control system also indirectly addresses the power sharing scheme by addressing the DC bus voltage.

Still considering the first two load cases, amidst the energy storage system which governs the DC bus voltage, both the hydropower generator and the PV system inject power into the microgrid without regard to the DC bus voltage. These are classified as single objective controllers and are directly controlled based on their power output, whereas the PV system is operating in MPPT mode as mentioned above, and the hydropower generator undertakes two different approaches to the power injection in the first two operation modes.

Although both of the operation modes utilise the generator as a constant power source rather than a governor system for the DC bus voltage, the second mode of operation utilises an excitation control to regulate the generator's field voltage, whereas the first operation mode has the field voltage fixed at nominal value. Implementing the excitation controller effectively enables the generator's field voltage to be altered in order to address its terminal voltage. In the context of the remaining system, this operation mode is reminiscent of how the energy storage system addresses its power influx indirectly by imposing a control system to address the voltage. Equally, because of the slower response time of the battery in the two first load cases, there occur temporary moments, when the supercapacitor is not included in the system, where the imbalance in the system causes disturbances to both the power sharing, DC bus voltage. These disturbances manifest themselves not only in the DC bus, where they are rectified by the battery after a certain amount of time but also in the AC bus voltage, i.e., the terminal voltage of the generator. This way, the generator system is able to somewhat minimise the effect of the temporarily occurring disturbance, as shown in the load sharing of the second operation mode in Figure 4-19 and its correlating DC bus voltage in Figure 4-23. The same effect takes place when the supercapacitor is

involved, although much less exaggerated. This is a reasonable argument as to why the robustness of mode of operation 2 is greater than for mode of operation 1.

Even though the generator system is somewhat able to address the active power shares of the microgrid by using the excitation controller, its effect is very limited. Therefore, a far more impactful control method is through AGC. The active power output of the generator can then be more directly controlled, using the proportionality between active power and the frequency, which is mainly driven by the generator speed. With this implemented in modes of operation 1 and 2, one could experience an even better generator performance with regards to compensating for the power shares in the system than what is achieved with only the excitation system.

In order to address the DC bus voltage in the third mode of operation, the generator system employs VSR control on an active rectifier. Although this operation mode shows promising results regarding robustness and DC bus voltage stabilisation, certain aspects also need to be considered. When comparing the DC bus voltages across the three modes of operation, in Figure 4-7 and Figure 4-10 for mode 1, Figure 4-25 and Figure 4-28 for mode 2, and Figure 4-38 and Figure 4-40 for mode 3, there appear to be considerably larger ripples in the DC bus voltage regulated by the VSR controller than in the previous modes. It is reasonable to suggest that where there are used more controllers, each may represent a potential source of ripple noise and that this may be the reason why this is more prominent for this load case.

Furthermore, by looking into the d- and q projections of the AC bus voltage- and current in Figure 4-41 and Figure 4-42, respectively it is obvious that some a significant amount of ripples actually are originating from the AC side. By further analysing the d- and q projection used for the VSR control system, primarily from load case 1, in Figure 4-43 for the current regulation, and Figure 4-44 for the derived voltage reference, it can be confirmed that it actually is the VSR controller that is the culprit. As expected, the ripple occurrences are more exaggerated at instances with more power in the system. This is confirmed by the same d- and q projection plots from the current and voltage regulation in load case 2, shown in Figure 4-45 and Figure 4-46, respectively. However, as shown by the actually imposed reference voltage waveform in Figure 4-47, the VSR regulation is definitely able to perform its control objective regardless of the noise, which eventually can be diminished by further tuning.

Another consideration regarding the third operation mode is the stress this mode imposes on the battery system. As mentioned in subchapter 2.1.3, one of the reasons to use a supercapacitor to undertake the majority of the stress caused by abrupt operation changes of the storage system is to spare the battery as this may drastically decrease the battery lifetime. It is clear by looking at the battery current graph in Figure 4-48 and the power shares of the battery along load case 1 in Figure 4-35 that the battery is subject to significantly more abrupt load changes than in the previous load case, which arguably will damage the battery over time, as earlier discussed in subsection 5.1. Therefore, one can argue whether the improved system robustness is worth it if the sustained operation deteriorates the battery. A sensible solution would be to implement this operation mode only on load dynamics that are within a certain degree of abruptness so the system may gain from the robustness while safeguarding the battery system. An alternative solution can be to install the supercapacitor in parallel with the battery system, reassembling the HES system for this mode of operation as well, as a way of off-loading the most abrupt load changes subjected from the battery system.

It stands to mention that in each of the instances there is implemented a PI controller, there is potential for further, finer tuning than performed in this thesis. Particularly the supercapacitor system seems to host a considerable magnitude of ripple noise, whereas the reason for this may lie in the supercapacitor's

exceptional response time. This makes even the smallest deviation to its operation point exaggerated in the system. Although acceptable results are achieved for the purpose of performing an analysis on the proposed simulation model, an application in real life would require more finely tuned regulators, particularly for the supercapacitor system and the VSR controller. However, an alternative cause of the system ripples, including the large power spikes occurring in the PV power output, may be originating from the various filter systems in the simulation model, which are discussed in greater detail in the following subchapter 5.3.

5.3 Power Electronics

The converter's design disclosed under chapter 2 is clearly working as intended. However, their high switching frequency is prone to causing ripple- and spike noise, which further may cause stability issues on the DC bus and is the reason to why there are installed filters.

A close examination of the PV system's produced power output in Figure 4-11 shows that large spike noise occurs during the simulation. Coincidentally, each of these occurrences are at the time when the irradiance undergoes an abrupt change. Furthermore, the same spike noise can be observed in voltage- and current plots in Figure 4-12, where a comparison to the irradiance plot further supports relation between the spike and the abrupt change of irradiance. As incidences with large leaps of input values often are related to equally large responses by its correlating governing body, there is likely a connection between the resulting spike and the sudden change of PWM switching caused by the MPPT algorithm. Similarly, a significant number of ripples can be observed in the same voltage and current plot. As discussed in the subchapter above, these may originate from the steady-state oscillations caused by the P&O MPPT algorithm. However, the produced PV power is at the expected levels and kept stable for each simulation. This indicates that the utilised DC-DC boost converter design presented in subchapter 2.1.1 is working in accordance with the PV system's specifications and that the MPPT algorithm is sufficiently designed for this converter. However, it may be argued that the occurring noise could be reduced by further adjusting the PV boost converter's filters.

By evaluating the battery's current and voltage for the first load case in mode of operation 1, both without- and with the supercapacitor, shown in Figure 4-13 and Figure 4-14, respectively, a noticeably low ripple noise appears to occur for both charge- and discharging mode. What is particularly advantageous is that no spike noise occurs even when the battery is subjected to fast load changes without the presence of the supercapacitor. Similar results can be viewed in load case 1 for the second mode of operation, both without- and with the supercapacitor involved, shown in Figure 4-29 and Figure 4-30, respectively. The ripples that occur throughout load case 2 are shown in Figure 4-16 and Figure 4-17 for mode of operation 1, and Figure 4-32 and Figure 4-33 for mode 2. These plots show that the ripples and load spikes are prevented throughout the entire simulation of load case 2 as well, across each mode of operation.

Compared to the battery system, the supercapacitor system contains significantly more ripple noise even though it adopts the same bidirectional converter design as shown in Figure 4-15 and Figure 4-31. By account of the produced noise, it can be argued that the designed LC filtering is not as well suited for the supercapacitor as it was for the battery. If this is the case, the noise may be reduced or completely eliminated by readjusting the capacitor- and induction filter. As mentioned in subchapter 5.1, the noise may also originate from the control system. While there undoubtedly is noise arising from the supercapacitor system, it apparently does not seem to affect the stability of the DC bus. However, it can be argued that the produced noise can further develop into harmonic distortions on the AC bus if not

contained. For the second load case, similar noise can be viewed for mode of operation 1, Figure 4-18, and mode of operation 2, Figure 4-34.

When considering the battery's SOC parameter of each mode of operation in load case 1, it is apparent that the one's excluding the supercapacitor in the simulation, shown in Figure 4-13 and Figure 4-29, shows a steeper SOC curve compared to the simulations where the supercapacitor is involved, shown in Figure 4-14 and Figure 4-30. This essentially means that the battery system gains from having the supercapacitor present in two different ways. The first is reducing the stress imposed on the battery, as discussed earlier, and the second is that the operation occupies less battery capacity. However, the second load case shows the opposite trend, i.e., the presence of the supercapacitor causes the battery system's SOC curve to become steeper. This becomes apparent by comparing the SOC plots for load case 2 without the supercapacitor, shown in Figure 4-16 and Figure 4-32 for mode of operation 1 and 2, to the SOC plots with the supercapacitor installed, showed in Figure 4-17 and Figure 4-33.

For the microgrid's AC side, as mentioned in subchapter 2.2.2, a filter is required to reduce the noise originating from the rectifier's six PWM controlled IGBTs. The effect of the filter can be seen in Figure 4-50, where AC voltage is plotted before and after the passive filter. Furthermore, the filter's effect on the current can be seen in Figure 4-51. A close examination of the two figures shows that the filters successfully are able to "clean" the waveforms to such a degree that the AC side can successfully be integrated into the system, avoiding huge disturbances.

5.4 Grid Layout, Topology, and Architecture Considerations

One of the most prominent features of distributed generation, in general, is the ability to not be entirely affected by outages occurring in the public grid, be it from extreme weather, sabotage, or maintenance work. When applying this microgrid concept to industrial loads in manufacturing processes, particularly when applied in island-mode as covered in this thesis, it is reasonable to argue that this would work to maintain the manufacturing plant's operation despite a blackout scenario that would otherwise incapacitate the production. Nevertheless, for the proposed microgrid to function in island mode operation, certain requirements regarding the power influx must be satisfied. In short, this specifically involves ensuring a sufficient amount of hydropower production as well as available storage capacity in the battery system. Load case 2 shows how this scenario poses a challenge when it comes to depleting the storage systems during periods of high load demand and little to no PV power injection. Although, as argued above, the microgrid does possess the necessary foundations to undertake grid connected mode, with minimal system customisation, which could work as a fail-safe in this sort of scenario, safeguarding the power influx. Also, when considering the earlier point, arguing that supplying AC load from the AC bus is beneficial in the context of energy efficiency and how DC energy storage is most applicable for DC loads, it is reasonable to argue that in microgrid configurations with AC loads, a grid connection may pose as a viable option for balancing the AC load the same way battery storage is applicable for balancing DC loads. Or in other words: the grid may undertake the same function for the AC load as the battery does for the DC load in that scenario.

It is arguable whether the physical layer of the microgrid model constructed in this thesis only encompasses primary control or inherits secondary- and tertiary level control mechanisms as well. Nevertheless, a reasonable assessment is that the main goal of this model, regarding the DC bus stability, is clearly within the primary control level domain, as presented in subchapter 2.3.1. However, there are a couple of indices that certain secondary control mechanisms are present, although not directly addressed in the control strategy of this system, whereas the presence of the AC bus pose as one of them.

As stated in this thesis' theory part on the secondary control level, in subchapter 2.3.2, this control level usually resides between the microgrid's physical layer and the public grid, benefitting from the primary level's obtained robustness and stability. Since the AC bus, as it is modelled in this thesis, obviously would work as a mediator between the public grid and the microgrid model if it was to be grid connected, an argument can definitely be had in favour of the presence of the secondary control level. It is also stated that the secondary control level usually undertakes alterations of the control strategy, managed by top layer mechanisms. Therefore, it can be further argued that the ability to select or deselect the inclusion of the supercapacitor, as is done in the first two modes of operation, as well as switching between the modes of operation, can also be conceived as secondary control mechanisms. An example of how this can be implemented to the system if it were it to be realised is an instance where it is forecasted or predicted that the load profile inherits a very slow transient response, meaning that the stabilisation of the DC bus does not require a supercapacitor in order to undertake the DC bus regulation sufficiently. It would then be the secondary control system that is charged with imposing a change of mode of operation to address this, in this case, either by deactivating the supercapacitor as shown in the mode of operation 1 and 2 or by initiating mode of operation 3. However, a control operation such as this plays to the secondary control level's ability to mediate between the surrounding control levels. Therefore, it would require that there, in fact, is a tertiary control level present in the system, which, when considering the microgrid model constructed in this thesis, is a discussion in itself.

As stated in subsection 2.3.3, the tertiary control level is the control organ that performs the top-level considerations and decision making regarding the overall operation of the microgrid. Since the microgrid model built in this thesis is an isolated system, so to speak, there are naturally no third level mechanisms programmed into this model. However, the model is perfectly sufficient to exemplify the several uses of the tertiary level's function and how they would be imposed in the system if it were a greater infrastructure. In the example in the paragraph above, it would be the tertiary control level that is tasked with the decision making behind what the secondary level is appointed to alter or facilitate. In general, a sensible assessment of the relationship between the tertiary- and the secondary control level can be explained as follows: The tertiary level is the mechanism that makes the system "smart" by making decisions based on available data and information and act in accordance. The secondary level is the mechanism that materialises the tertiary level's decision making and turns them into actual operation modes in the physical layer. In the context of the microgrid model used in this thesis, there are several ways to impose the tertiary level mechanisms and alternating between the modes of operation.

The capacity of the energy storage system, including the available water for driving the hydropower generator, is a good depiction of how the tertiary level is not only viewed as an optional addition to the microgrid but also poses as a vital mechanism for the microgrid to ensure a sustainable operation over time. As made clear in load case 2 across each mode of operation, where the microgrid undertakes a scenario where the storage-based power contributors are constantly running at high capacity, the state of charge parameters, shown in Figure 4-16 and Figure 4-17 for mode of operation 1, Figure 4-32 and Figure 4-33 for mode 2, and Figure 4-49 for mode 3, shows that this operation is not sustainable over a longer period of time as their storage eventually will be depleted. The same goes for the generator's water magazine, which also will experience a similar depletion. However, the tertiary control level can facilitate periods of operation like this by ensuring the water magazines or battery state of charge has sufficient capacity when entering such load cases by acting on predictions of periods with high load demand and low PV power production. Furthermore, the same principle arguably applies in opposite load cases as well, where there are risks of too much energy in the system in scenarios where the tertiary level forecasts a high PV production at a time the load demand is estimated to be low. The control

mechanism can then ensure that battery capacity is available to absorb excess power and lower the production- or shut down the hydropower generator.

6 Conclusion

Analysis of the component- and control system application of a hydropower- and PV based DC microgrid designed for electrifying land-based industries has successfully been performed using MATLAB Simulink where the undertaken load cases successfully portray the desired system characteristics. The hierarchical control system is imposed to the microgrid's physical layer model and each of the considered modes of operation across both load cases is able to satisfy the requirements defined as acceptable in this thesis, i.e., maximum ± 3 % DC bus voltage deviations, by implementing the following control system- and component applications:

- DC bus voltage governed by a HES system incorporating a voltage mode cascade control, with a split setpoint for the battery and supercapacitor systems based on high-frequency voltage transient filtering. Power requirements are met jointly by an MPPT operated PV system and salient pole synchronous generator operating under constant, rated speed. The field voltage of the generator may either be fixed at an appropriate value or regulated by a terminal voltage-based excitation control. Although both satisfy the requirements, the latter generator configuration shows an improved response.

- DC bus voltage governed by a salient pole synchronous generator system using excitation control and an active rectifier incorporating VSR control to regulate the DC bus voltage. Power requirements are met jointly by an MPPT operated PV system and a battery system incorporating single-regulator current mode control.

The final of the two control system- and component applications above incorporates the most robustness in terms of stabilizing the DC bus voltage and is, therefore, the preferable option. Furthermore, it can be stated that the implementation of the supercapacitor in mode of operation 1 and 2 is necessary to satisfy the ± 3 % DC bus voltage deviation requirements in the load cases considered in this thesis. It can be further concluded that the selected MPPT method is able to successfully carry out its operation, while the selected control strategies, i.e., voltage-mode control, current mode control, and VSR control have successfully been realised. Another conclusion regarding the control system is the successful realization of the benefits of decentralized control topology, where sustained operation of the system despite the failing of the PV system epitomizes this.

In the context of attaining the NWA concept to electrify the Norwegian DC based industry sector without major investments in the public grid, the proposed microgrid solution shows promising results. However, as made apparent by simulation load case 2 of the simulation model, the obstacle of safeguarding the storage capacity for the energy storage systems must be overcome for this microgrid solution to be completely viable. Implementing the top-level smartgrid system architecture through the tertiary level control is mentioned as a possible way of overcoming this, although further studies are required in order to draw conclusions based on this.

7 Future Work

The work of this thesis mainly covers the operation of the microgrid on the DC side. A natural development of this model is to further develop the proposed microgrid system to become more versatile when it comes to what type of load it can handle. This involves undertaking scenarios where both DC- and AC loads are connected. It would then be appropriate to implement a control system that allows the AC load to be balanced by an impending grid connection while the bulk of its power originates from the local hydropower plant, simultaneously with a DC load being balanced by the HES system on the DC side. This way, the two loads can be balanced by components installed on their designated bus in order to maintain energy efficiency during sustained operation. This would also pose a more realistic scenario with regard to the scope of this thesis, as one would expect to encounter AC loads as well as DC loads on industrial sites.

With regards to improving the existing model's physical layer infrastructure, there is clearly room for improvement when it comes to controller tuning and power system filtering. Particularly the supercapacitor systems control system could definitely be fine-tuned in order the eliminate the ripples that are apparent during all its operation. Furthermore, the VSR controller is also found to be a source of oscillations in the system, as discussed in subchapter 5.2. Additionally, the filter system for the AC bus needs more work if a grid connection were to be undertaken.

As the model stands, the hydropower generator system does not incorporate any form of speed governing or AGC but instead runs at the ideal scenario of constant, nominal speed. This is an area where the proposed microgrid system could clearly benefit from implementing an actual governing system instead. By implementing an actual AGC system to the proposed microgrid solution to the system, the ability to regulate the system's power flow would be greatly improved. Particularly mode of operation 1 and 2 would benefit from this, as the generator's excitation system is clearly not sufficient with regards to replacing the supercapacitor.

There are questions about whether the battery system in mode of operation 3 is sufficiently safeguarded from damaging stress. Further work may therefore encompass facilitating a function of only implementing the third operation mode for load dynamics with a certain time constant, or alternatively implementing the HES system for this mode, as argued in subchapter 5.2.

In the context of electrifying the Norwegian DC-based industry sector, a further development of this work is to find a solution to safeguarding the energy storage systems capacity. This is a clearly an obstacle that must be overcome in order to implement this technology.

References

[1] A. J. Eliston. "Hvor kommer strømmen fra?" Norwegian Water Resources and Energy Directorate. https://www.nve.no/energi/energisystem/kraftproduksjon/hvor-kommer-strommen-fra/ (accessed March 3., 2022).

[2] S. Skau. "Ny kraftproduksjon." Norwegian Water Resources and Energy Directorate. https://www.nve.no/energi/analyser-og-statistikk/ny-kraftproduksjon/ (accessed March 3., 2022).

[3] R. Andrew and G. Peters, "The Global Carbon Project's fossil CO2 emissions dataset: 2021 release," CICERO Center for International Climate Research, Oslo, Norway, 2021. [Online]. Available: https://doi.org/10.6084/m9.figshare.16729084.v1

[4] United Nations Population Division. "World Population Prospects: The 2019 Revision." United Nations Department of Economic and Social Affairs: Population Dynamics. https://population.un.org/wpp/ (accessed March 4., 2022).

[5] P. Friedlingstein *et al.*, "Global Carbon Budget 2021," *Earth Syst. Sci. Data Discuss.*, vol. 2021, pp. 1-191, 2021, doi: 10.5194/essd-2021-386.

[6] I. E. Haukeli. "Elektrifiseringstiltak i Norge." Norwegian Water Resources and Energy Directorate. https://www.nve.no/energi/analyser-og-statistikk/elektrifiseringstiltak-i-norge/ (accessed March 2., 2022).

[7] I. E. Haukeli *et al.*, "Elektrifiseringstiltak i Norge Hva er konsekvensene for kraftsystemet?," Norwegian Water Resources and Energy Directorate, Oslo, Norway, 36/2020, October, 2020 2020. Accessed: March 2. 2022. [Online]. Available: https://publikasjoner.nve.no/rapport/2020/rapport2020_36.pdf

[8] H. B. Laird. "Klimakur 2030." The Norwegian Environment Agency. https://www.miljodirektoratet.no/klimakur (accessed March 2., 2022).

[9] Oljedirektoratet, "Kraft fra land til Norsk sokkel," Norwegian Petroleum Directorate, Stavanger, Norway, 2020. Accessed: March 3. 2022. [Online]. Available: https://www.npd.no/globalassets/1-npd/publikasjoner/rapporter/2020/kraft-fra-land-til-norsk-sokkel/kraft-fra-land-til-norsk-sokkel-rapport-2020.pdf

[10] D. Spilde, J. Hole, and H. I. Endresen, "Elektrifisering av landbaserte industrianlegg i Norge: En kartlegging av teknisk potensial og konsekvensene for kraftnettet," Norwegian Water Resources and Energy Directorate, Oslo, Norway, 18/2020, June 2020. Accessed: March 2. 2022. [Online]. Available: https://publikasjoner.nve.no/rapport/2020/rapport2020_18.pdf

[11] Industry Technical Support Leadership Committee (ITSLC) Task Force, "Importance of T&D Grid Modernization to Mitigate Impacts from and Adapt to Climate Change," in "PES-Technical Report," The Institute of Electrical and Electronic Engineers, Inc., PES-TR93, 2022.

[12] A. G. Vikestad and A. Frantzen, "Analysis of the Component- and Control System Application of a PV Based DC Microgrid," University of Agder, Research Project, 2021.

[13] A. Raj and R. P. Praveen, "Highly efficient DC-DC boost converter implemented with improved MPPT algorithm for utility level photovoltaic applications," *Ain Shams Engineering Journal*, vol. 13, no. 3, p. 101617, 2022/05/01/ 2022, doi: https://doi.org/10.1016/j.asej.2021.10.012.

[14] N. Mohan, *Power electronics : a first course*. Hoboken, N.J: Wiley, 2012.

[15] Y. Koca, Y. Aslan, A. Yonetken, and Y. Oğuz, "Boost Converter Design and Analysis for Photovoltaic Systems," presented at the 4th International Conferenceon Engineering Technology and Applied Sciences (ICETAS), Kiev, Ukraine, 2019. [Online]. Available:

https://www.researchgate.net/profile/Ahmet-Yonetken/publication/332934556_Boost_Converter_Design_and_Analysis_for_Photovoltaic_Systems/links/5cd286ab299bf14d957e8b0d/Boost-Converter-Design-and-Analysis-for-Photovoltaic-Systems.pdf.

[16] B. Hauke, "Basic Calculation of a Boost Converter's Power Stage," Texas Instruments, Dallas, Texas, SLVA372C, 2014.

[17] L. Yang and T. Liang, "Analysis and Implementation of a Novel Bidirectional DC–DC Converter," *IEEE Transactions on Industrial Electronics*, vol. 59, no. 1, pp. 422-434, 2012, doi: 10.1109/TIE.2011.2134060.

[18] A. Elahi, *Bidirectional DC-DC Power Converter Design Optimization, Modeling and Control*. 2016.

[19] N. Kondrath, "Bidirectional DC-DC converter topologies and control strategies for interfacing energy storage systems in microgrids: An overview," in *2017 IEEE International Conference on Smart Energy Grid Engineering (SEGE)*, 14-17 Aug. 2017 2017, pp. 341-345, doi: 10.1109/SEGE.2017.8052822.

[20] S. Motahhir, A. El Hammoumi, and A. El Ghzizal, "The most used MPPT algorithms: Review and the suitable low-cost embedded board for each algorithm," *Journal of Cleaner Production*, vol. 246, p. 118983, 2020/02/10/ 2020, doi: https://doi.org/10.1016/j.jclepro.2019.118983.

[21] M. Hlaili and H. Mechergui, "Comparison of Different MPPT Algorithms with a Proposed One Using a Power Estimator for Grid Connected PV Systems," *International Journal of Photoenergy*, vol. 2016, p. 10, 2016. [Online]. Available: https://doi.org/10.1155/2016/1728398.

[22] A. Mohapatra, B. Nayak, P. Das, and K. B. Mohanty, "A review on MPPT techniques of PV system under partial shading condition," *Renewable and Sustainable Energy Reviews*, vol. 80, pp. 854-867, 2017/12/01/ 2017, doi: https://doi.org/10.1016/j.rser.2017.05.083.

[23] K. M. S. Y. Konara, M. L. Kolhe, and S. Arvind, "Power dispatching techniques as a finite state machine for a standalone photovoltaic system with a hybrid energy storage," *AIMS Energy*, vol. 8, no. 2, pp. 214-230, 2020, doi: 10.3934/energy.2020.2.214.

[24] K. Javed, H. Ashfaq, R. Singh, S. M. S. Hussain, and T. S. Ustun, "Design and Performance Analysis of a Stand-alone PV System with Hybrid Energy Storage for Rural India," *Electronics*, vol. 8, no. 9, 2019, doi: 10.3390/electronics8090952.

[25] K. M. S. Y. Konara, M. Kolhe, and A. Sharma, "Power flow management controller within a grid connected photovoltaic based active generator as a finite state machine using hierarchical approach with droop characteristics," *Renewable Energy*, vol. 155, pp. 1021-1031, 2020/08/01/ 2020, doi: https://doi.org/10.1016/j.renene.2020.03.138.

[26] S. Mehdi, B. Achour, A. Sabrina, and S. Ouchen, "Implementation of a real-time energy management consisting of a battery and a supercapacitor," in *2017 5th International Conference on Electrical Engineering - Boumerdes (ICEE-B)*, 29-31 Oct. 2017 2017, pp. 1-6, doi: 10.1109/ICEE-B.2017.8192200.

[27] I. Boldea, "Synchronous Generators," ed: CRC Press, 2015.

[28] J. K. Nøland and U. Lundin, "Step time response evaluation of different synchronous generator excitation systems," in *2016 IEEE International Energy Conference (ENERGYCON)*, 4-8 April 2016 2016, pp. 1-7, doi: 10.1109/ENERGYCON.2016.7513956.

[29] M. Micev, M. Ćalasan, and D. Oliva, "Design and robustness analysis of an Automatic Voltage Regulator system controller by using Equilibrium Optimizer algorithm," *Computers &*

Electrical Engineering, vol. 89, p. 106930, 2021/01/01/ 2021, doi: https://doi.org/10.1016/j.compeleceng.2020.106930.

[30] D. P. Kothari and N. I. J., "Automatic Generation and Voltage Control," in *Modern power system analysis*. New Delhi: Tata McGraw-Hill Pub. Co., 2003, ch. 8, pp. 290-325.

[31] H. Shayeghi, H. A. Shayanfar, and A. Jalili, "Load frequency control strategies: A state-of-the-art survey for the researcher," *Energy Conversion and Management*, vol. 50, no. 2, pp. 344-353, 2009/02/01/ 2009, doi: https://doi.org/10.1016/j.enconman.2008.09.014.

[32] H. M. Hasanien, "Design Optimization of PID Controller in Automatic Voltage Regulator System Using Taguchi Combined Genetic Algorithm Method," *IEEE Systems Journal*, vol. 7, no. 4, pp. 825-831, 2013, doi: 10.1109/JSYST.2012.2219912.

[33] T. R. S. de Freitas, P. J. M. Menegáz, and D. S. L. Simonetti, "Rectifier topologies for permanent magnet synchronous generator on wind energy conversion systems: A review," *Renewable and Sustainable Energy Reviews*, vol. 54, pp. 1334-1344, 2016/02/01/ 2016, doi: https://doi.org/10.1016/j.rser.2015.10.112.

[34] P. T. Huynh, P. J. Wang, and A. Banerjee, "An Integrated Permanent-Magnet-Synchronous Generator–Rectifier Architecture for Limited-Speed-Range Applications," *IEEE Transactions on Power Electronics*, vol. 35, no. 5, pp. 4767-4779, 2020, doi: 10.1109/TPEL.2019.2946244.

[35] A. E. W. H. Kahlane, L. Hassaine, and M. Kherchi, "LCL filter design for photovoltaic grid connected systems," in *Revue des Energies Renouvelables SIENR'14*, Ghardaïa, Algeria, 2015, pp. 117-232. [Online]. Available: https://www.cder.dz/download/sienr2014_31.pdf. [Online]. Available: https://www.cder.dz/download/sienr2014_31.pdf

[36] M. Liserre, F. Blaabjerg, and S. Hansen, "Design and control of an LCL-filter-based three-phase active rectifier," *IEEE Transactions on Industry Applications*, vol. 41, no. 5, pp. 1281-1291, 2005, doi: 10.1109/TIA.2005.853373.

[37] P. Shweta and S. Nagendraprasad, "Vector Controled Voltage Source PWM Rectifier," *International Journal of Engineering Research and*, vol. V4, no. 04, 2015/04/23 2015, doi: 10.17577/ijertv4is040845.

[38] K. R. Naik, B. Rajpathak, A. Mitra, and M. L. Kolhe, "Assessment of energy management technique for achieving the sustainable voltage level during grid outage of hydro generator interfaced DC Micro-Grid," *Sustainable Energy Technologies and Assessments*, vol. 46, p. 101231, 2021/08/01/ 2021, doi: https://doi.org/10.1016/j.seta.2021.101231.

[39] C. J. O'Rourke, M. M. Qasim, M. R. Overlin, and J. L. Kirtley, "A Geometric Interpretation of Reference Frames and Transformations: dq0, Clarke, and Park," *IEEE Transactions on Energy Conversion*, vol. 34, no. 4, pp. 2070-2083, 2019, doi: 10.1109/TEC.2019.2941175.

[40] C. V. Suru, C. A. Patrascu, and M. Linca, "The synchronous fundamental dq frame theory implementation and adaptation for the active filtering," in *2014 International Conference on Applied and Theoretical Electricity (ICATE)*, 23-25 Oct. 2014 2014, pp. 1-6, doi: 10.1109/ICATE.2014.6972654.

[41] J. Pradeep and R. Devanathan, "Adoption of Park's Transformation for Inverter Fed Drive," *International Journal of Power Electronics and Drive Systems (IJPEDS)*, vol. 5, p. 366, 02/01 2015, doi: 10.11591/ijpeds.v5.i3.pp366-373.

[42] J. R. Rodriguez, J. Dixon, J. Espinoza, J. Pontt, and P. Lezana Illesca, "PWM regenerative rectifiers: State of the art," *Industrial Electronics, IEEE Transactions on*, vol. 52, pp. 5-22, 03/01 2005, doi: 10.1109/TIE.2004.841149.

[43] J. Raisch, A.-K. Schmuck, D. Gromov, and G. Stephanie, "Hierarchical Control Theory," Berlin, 2018.

[44] J. C. Vasquez, J. M. Guerrero, J. Miret, M. Castilla, and L. G. d. Vicuña, "Hierarchical Control of Intelligent Microgrids," *IEEE Industrial Electronics Magazine*, vol. 4, no. 4, pp. 23-29, 2010, doi: 10.1109/MIE.2010.938720.

[45] D. Y. Yamashita, I. Vechiu, and J.-P. Gaubert, "A review of hierarchical control for building microgrids," *Renewable and Sustainable Energy Reviews*, vol. 118, p. 109523, 2020/02/01/ 2020, doi: https://doi.org/10.1016/j.rser.2019.109523.

[46] A. Kiani and A. Annaswamy, "Distributed hierarchical control for renewable energy integration in a Smart Grid," in *2012 IEEE PES Innovative Smart Grid Technologies (ISGT)*, 16-20 Jan. 2012 2012, pp. 1-8, doi: 10.1109/ISGT.2012.6175710.

[47] J. Dudiak, Z. Conka, and M. Kolcun, "Hierarchical control of microgrid with renewable energy sources and energy storage," in *Elektroenergetika 2015*, Stara Lesna, Slovak Republic, 2015, no. 8, pp. 568-571.

[48] F. Gao, R. Kang, J. Cao, and T. Yang, "Primary and secondary control in DC microgrids: a review," *Journal of Modern Power Systems and Clean Energy*, vol. 7, no. 2, pp. 227-242, 2019, doi: 10.1007/s40565-018-0466-5.

[49] S. Dahale, A. Das, N. M. Pindoriya, and S. Rajendran, "An overview of DC-DC converter topologies and controls in DC microgrid," in *2017 7th International Conference on Power Systems (ICPS)*, 21-23 Dec. 2017 2017, pp. 410-415, doi: 10.1109/ICPES.2017.8387329.

[50] B. Mammano and M. Jordan, "Load Sharing with Paralleled Power Supplies," Texas Instruments, SLUP094, 1991. Accessed: 25. March 2022. [Online]. Available: https://www.thierry-lequeu.fr/data/SLUP094.pdf

[51] Posharp. "SPR-305E-WHT-D Solar Panel from SunPower." Posharp. http://www.posharp.com/spr-305e-wht-d-solar-panel-from-sunpower_p1621616600d.aspx (accessed 02. May, 2022).

[52] S. MATLAB. "Help center, Documentation, Battery model." The MathWorks Inc. https://se.mathworks.com/help/physmod/sps/powersys/ref/battery.html (accessed 2022).

[53] S. MATLAB. "Help center, Documentation, Supercapacitor model." The MathWorks Inc. https://se.mathworks.com/help/physmod/sps/powersys/ref/supercapacitor.html (accessed 2022).

[54] S. MATLAB. "Help center, Documentation, Synchronous machine pu standard model." The MathWorks Inc. https://se.mathworks.com/help/physmod/sps/powersys/ref/synchronousmachinepustandard.html?searchHighlight=synchronous%20machine&s_tid=srchtitle_synchronous%20machine_4 (accessed 2022).

[55] C. S. Jensen. "Små vannkraftverk." Norwegian Water Resources and Energy Directorate. https://www.nve.no/konsesjon/konsesjonsbehandling-av-vannkraft/smaa-vannkraftverk/ (accessed 28.04.2022, 2022).

[56] S. MATLAB. "Help center, Documentation, One-Quadrant Chopper DC Drive model." The MathWorks Inc. https://se.mathworks.com/help/physmod/sps/powersys/ref/onequadrantchopperdcdrive.html (accessed 2022).

Appendix

Appendix A – MPPT Algorithm

```
function D = MPPT_Control(V,I)

Dmax=0.75;
Dmin=0;
Dint = 0.5;
deltaD=125e-6;
persistent Vold Pold Dold;

dataType ='double';

if isempty(Vold)
    Vold=0;
    Pold=0;
    Dold=Dint;
end

P = V*I;
dV = V - Vold;
dP = P - Pold;

if dP ~= 0
    if dP < 0
        if dV < 0
            D = Dold - deltaD;
        else
            D = Dold + deltaD;
        end
    else
        if dV < 0
            D = Dold + deltaD;
        else
            D = Dold - deltaD;
        end
    end
else
    D=Dold;
end
if D>=Dmax||D<=Dmin
    D=Dold;
end

Dold=D;
Vold=V;
Pold=P;
```